Investigation on the Electrical Transport Properties and the Structural Evolution of Emerging Energy Materials under High Pressure

Huacai Yan

université
PARIS-SACLAY

Investigation on the Electrical Transport Properties and the Structural Evolution of Emerging Energy Materials under High Pressure

Etude des propriétés de transport électrique et de l'évolution structurale de matériaux énergétiques émergents sous haute pression

Thèse de doctorat de l'université Paris-Saclay

École doctorale n°564 : physique en Île-de-France (PIF)
Spécialité de doctorat : Physique
Graduate School : Physique. Référent : Faculté des sciences d'Orsay

Thèse préparée dans l'unité de recherche **Synchrotron Soleil** (Université Paris-Saclay), sous la direction de **François BAUDELET**, Directeur de recherche, et la co-direction de **Qingyu KONG**, Scientifique de Ligne De Lumière

Thèse soutenue à Paris-Saclay, le 19 Mai 2022, par

Huacai YAN

Composition du Jury

Anne BLEUZEN Professeur, Université Paris-Saclay	Présidente
Alfonso SAN-MIGUEL FUSTER Professeur, Université Lyon 1 et CNRS	Rapporteur & Examinateur
Andrea DI CICCO Professeur, University of Camerino (Italy)	Rapporteur & Examinateur
Angelika ROSA Chargée de recherche, European Synchrotron Radiation Facility (Grenoble)	Examinatrice
Qingyu KONG Scientifique de Ligne De Lumière, Synchrotron SOLEIL	Co-Directeur de thèse

THÈSE DE DOCTORAT

NNT : 2022UPASP047

université PARIS-SACLAY | ÉCOLE DOCTORALE Physique en Île-de-France (PIF)

Titre : Etude des propriétés de transport électrique et de l'évolution structurale de matériaux énergétiques émergents sous haute pression

Mots clés : Haute pression, pérovskites, spectroscopie d'impédance, photocourant, matériaux lamellaires 2D, spectroscopie d'absorption des rayons X

Résumé : Pour résoudre les problèmes environnementaux dus à l'utilisation de combustibles fossiles traditionnels, les scientifiques recherchent activement de nouveaux matériaux énergétiques pour développer et utiliser des énergies renouvelables et propres. Des pérovskites et des composés lamellaires bidimensionnels ont attiré l'attention comme matériaux de cellules solaire en raison de leurs remarquables propriétés photovoltaïques. La pression est un moyen important qui peut modifier les propriétés structurales et électroniques des matériaux, modifiant ainsi le transport électrique et les propriétés photoélectriques des matériaux. Dans ce travail, nous avons choisi $CsPbBr_3$, ReS_2 et l'arsenic noir (« black arsenic », bAs) comme objets de recherche, qui sont représentatifs des pérovskites et des matériaux bidimensionnels. Les propriétés de transport électrique de $CsPbBr_3$ ont été étudiées sous pression par spectroscopie d'impédance en courant alternatif (AC) in situ et par des mesures de photo-courant. L'évolution structurale de ces matériaux a été étudiée sous pression en utilisant la spectroscopie d'absorption des rayons X (SAX) in situ. Les résultats détaillés de cette étude sont les suivants : 1) Par des mesures de spectroscopie d'impédance in situ sous haute pression, nous avons étudié systématiquement les propriétés de transport électrique de $CsPbBr_3$. Nous avons déterminé que ce composé subit une transition de phase structurale à 1,2 GPa. Lorsque la pression est inférieure à 2,3 GPa, il y a coexistence de la conduction électronique et ionique. Quand la pression dépasse 2,3 GPa, la conduction ionique disparaît, et une transition de la conduction ionique à la conduction électronique se produit. Par des mesures de photoconductivité in situ à haute pression, nous avons déterminé que la réponse à la lumière visible de $CsPbBr_3$ dans la phase haute pression était nettement meilleure que celle de la phase basse pression, ce qui indique que la pression peut améliorer ses propriétés photoélectriques. Les résultats de spectroscopie d'absorption SAX à haute pression ont également confirmé que $CsPbBr_3$ subit une transition de phase à 1,2 GPa, et grâce à l'analyse des résultats par transformée de Fourier, nous savons que la pression provoque une diminution continue de la distance Pb-Br, ce qui entraîne des distorsions et des contractions des octaèdres $PbBr_6$, ce qui induit la transition de phase. 2) Nous avons étudié l'évolution de la structure locale du ReS_2 par des mesures in situ de la structure fine d'absorption des rayons X (EXAFS) à haute pression. Nous avons trouvé une transition intra-couche à 6,0 GPa associée à la rotation dans le sens inverse des aiguilles d'une montre des atomes de soufre autour de la chaîne d'atomes de Re conduisant à la formation de liaisons covalentes S-S entre les couches, suivie d'une transition inter-couche d'un empilement désordonné à un empilement ordonné à 20,4 GPa. Les résultats de la transformation de Fourier montrent que les longueurs de liaison Re-S deviennent progressivement plus courtes lorsque la pression augmente dans toute la gamme de mesure. Nous avons déterminé le nombre d'atomes S entourant Re, la valeur du pseudo-coefficient de Debye-Waller et la longueur de la liaison Re-S, qui passe de 2,413 Å à pression ambiante à 2,378 Å à 20,4 GPa par ajustement structural local. 3) Nous avons étudié l'évolution de la structure de bAs par des mesures d'EXAFS in situ à haute pression. Nous avons déterminé que bAs subit une transition structurale de la phase basse pression A17 (bAs) à la phase A7 (As gris) à 4,7 GPa. Elle est attribuée à la formation de nouvelles liaisons inter-couches alors que les liaisons intra-couches sont rompues. Une autre transition de phase se produit à 10,8 GPa, où nous proposons une transition de phase de A7 à une phase cubique simple (SC). Les résultats de la transformation de Fourier montrent la formation de liaisons inter-couche As-As à 4,7 GPa ; les longueurs de liaison deviennent progressivement plus courtes dans toute la gamme de pression.

université PARIS-SACLAY

ÉCOLE DOCTORALE
Physique en Île-de-France (PIF)

Title : Investigation on the Electrical Transport Properties and the Structural Evolution of Emerging Energy Materials under High Pressure

Keywords : High pressure, perovskites, impedance spectroscopy, photocurrent, 2D layered materials, X-ray absorption spectroscopy

Abstract : To solve the environmental problems caused by the use of traditional fossil fuels, scientists are actively exploring new energy materials to develop and utilize renewable and clean energy. Perovskite solar cell materials and two-dimensional layered materials have attracted worldwide attention as solar harvesting materials because of their remarkable photovoltaic properties. Pressure is an important means which can alter the geometric and electronic structures of the materials, thereby changing the electrical transport and photoelectric properties of the materials. In this work, we select $CsPbBr_3$, ReS_2, and black arsenic (bAs) as the research objects, which are representative of perovskite and two-dimensional materials. The electrical transport properties of $CsPbBr_3$ were investigated under pressure by in-situ alternative current (AC) impedance spectroscopy and photocurrent measurements. The structural evolution of these materials was investigated under pressure using in-situ X-ray absorption spectroscopy (XAS) method. In these measurements, the detailed results of the study are as follows: 1) By in-situ high-pressure impedance spectroscopy measurements, we have systematically studied the electrical transport properties of $CsPbBr_3$. We found that $CsPbBr_3$ undergoes a structural phase transition at 1.2 GPa, and when the pressure is below 2.3 GPa, both electronic and ionic conduction coexist within $CsPbBr_3$. When the pressure exceeds 2.3 GPa, the ionic conduction disappears, and the transition from ion/electron mixed conduction to pure electronic conduction occurs. By in situ high-pressure photoconductive measurements, we found that the visible light response of $CsPbBr_3$ in the second phase was significantly better than that of the ambient phase, indicating that pressure can improve its photoelectric properties. The results of high-pressure XAS also confirmed that $CsPbBr_3$ undergoes a phase transition at 1.2 GPa, and through the analysis of the Fourier transform results, we know that the pressure causes the Pb-Br distance to decrease continuously, resulting in the distortions and contractions of the $PbBr_6$ octahedra, which induces the phase transition. 2) By in-situ high-pressure Extended X-ray Absorption Fine Structure (EXAFS) measurements, we investigated the local structure evolution of ReS_2. We found an intralayer transition at 6.0 GPa, which was associated with the counterclockwise rotation of S atoms around the chain of Re atoms leading to the interlayer S-S covalentlike bond formation, followed by an interlayer transition from disordered to ordered stacking at 20.4 GPa. The Fourier transformed results show that the Re-S bond lengths gradually become shorter as the pressure increases in the entire measurement range. We obtained the number of S atoms surrounding Re, the Debye-Waller value, and the accurate Re-S bond length, which decreases from 2.413 Å at ambient pressure to 2.378 Å at 20.4 GPa by the local structural fitting analysis. 3) We investigated the structure evolution of bAs by in-situ high-pressure EXAFS measurements. We found bAs undergo a phase transition from A17 (bAs) to the A7 (gray As) phase at 4.7 GPa, which is attributed to the new interlayer bonds formation while intralayer bonds are broken. Another phase transition occurs at 10.8 GPa, where we believe the phase transition from A7 to simple cubic (SC) phase. The Fourier transformed results show that the formation of the interlayer As-As bond at 4.7 GPa and the bond lengths gradually become shorter in the entire pressure range.

Acknowledgements

First and foremost, I would like to express my deepest gratitude and appreciation to my supervisors: Dr. François BAUDELET and Dr. Qingyu KONG. Without their guidance, I could not pass a hard time pursuing my Ph.D.

François was a very good teacher and physicist with solid knowledge, and a great sense of humor. He has shared with me his good research taste from which I will benefit in my career. All his insightful comments on my works have always been an invaluable source of inspiration to deepen my understanding. Over the past few years, despite suffering from cancer, he was still very optimistic about life and still able to work with passion. Unfortunately, he died suddenly of illness a few months before my defense. I feel very sad about this. I still remember clearly. In the last days of his life, he was still helping me revise my thesis and giving me a lot of professional advice and guidance. I am very grateful and miss him. It's a pity that he didn't see me graduate. Although it was difficult, I finally completed the defense. I hope I didn't let him down.

I also would like to thank Qingyu for his patience and enlightening guidance. It was a very critical moment that I learned many skills from him in experimental measurement and data processing. The work went better after each discussion. I was very lucky to meet him in France. He has given me a lot of selfless help both at work and in life. He often accompanies me on experiments until midnight because he is worried about my safety. When I first came to France, he helped me solve many difficulties in life. Especially I am so grateful for the empathy he showed when my grandma passed away, I was so frustrated and heartbroken that I couldn't go back to China to meet her at the last moment. I

am so grateful for his companion and comfort in helping me through that dark time.

I would like to thank Anne BLEUZEN and Alain POLIAN, as members of the review committee, they listened to my report on the work of each year and gave me many constructive comments at the end of each academic year. Especially Alain also provided some help for my experiments and obtained good experimental results. In addition, I would like to thank my colleagues Jean CODUET, Lucie NATAF, and Anojh THEVARASAN for their help with my work.

I would like to thank all the friends that I have spent time with in France, including Zhesheng CHEN, Jingwei DONG, Yimin MIJITI, Dongjun WU, Jiuxiang ZHANG, Miao FENG, Guozhao ZHANG, Haiwa ZHANG, Wenyi WU, Kai ZHANG, Peiyuan SU, Shu ZHANG, Lu ZHAO, Yan GAO, Weiyan QI, Yuanyuan LIAO, Xuan LIU, Tongtong LÜ, Kai CHEN, Minghe ZHANG, Shengyu TANG, Qiang ZHANG..., the list can be endless and I have no way of naming them all. It is them who made my entire Ph.D. less tedious and more enriching, and our interactions have become some of the best memories of my life.

I express my deep gratitude to all the jury members: Dr. Anne BLEUZEN, Dr. Alfonso SAN-MIGUEL FUSTER, Dr. Andrea DI CICCO, Dr. Alain POLIAN, Dr. Rosa ANGELIKA, Dr. Xujie LÜ, Dr. Qingyu KONG and Dr. François BAUDELET. I am particularly honored for your attendance in my defense. A special thank Dr. Alfonso SAN-MIGUEL FUSTER, Dr. Andrea DI CICCO, and Dr. Alain POLIAN for correcting all details in my thesis. I really thank China Scholarship Council (CSC) for providing the Ph.D. Fellowship to me.

Finally, I sincerely appreciate my family for their continuous support and care. I wish to express my sincere appreciation for my beloved girlfriend Yujie XING, thanks for her warm accompaniment and encouragement during the most helpless time in my life.

Synthèse en français

Les combustibles fossiles traditionnels tels que le pétrole, le charbon et le gaz naturel donnent un élan continu au développement de la société et de l'économie modernes. Mais l'utilisation des combustibles fossiles entraîne une série de problèmes environnementaux. Pour résoudre ces problèmes, les scientifiques explorent activement de nouveaux matériaux énergétiques afin de développer et d'utiliser des énergies renouvelables et propres. Parmi les différentes technologies d'énergie verte, l'énergie solaire est considérée comme une technologie très prometteuse. L'obtention et la conversion de l'énergie solaire peuvent contribuer à résoudre les problèmes énergétiques et environnementaux actuels. Les matériaux de cellules solaires en pérovskite et les matériaux en couches bidimensionnelles (2D) ont attiré l'attention du monde entier en tant que matériaux de collecte solaire en raison de leurs remarquables propriétés photovoltaïques. D'une manière générale, ces matériaux sont largement utilisés dans divers dispositifs photovoltaïques. Afin d'améliorer les performances des dispositifs photovoltaïques basés sur ces matériaux, il est nécessaire d'explorer et d'améliorer leurs propriétés.

Pour comprendre et explorer pleinement les propriétés de ces matériaux énergétiques émergents, des outils et techniques appropriés sont nécessaires pour effectuer des mesures complètes. La pression est une variable thermodynamique fondamentale qui peut être facilement réglée dans l'expérience, permettant des avancées significatives dans des domaines scientifiques et technologiques aussi vastes que la physique, la chimie, la biologie, etc. Les études sous haute pression sont utiles pour comprendre les propriétés des molécules et des matériaux. Les expériences de spectroscopie

d'impédance en courant alternatif (AC), de photocourant et de spectroscopie d'absorption des rayons X (XAS) sous haute pression sont des méthodes importantes pour étudier les propriétés électroniques, photoélectriques et structurales.

La spectroscopie d'impédance AC est une technique expérimentale très importante pour étudier les propriétés électriques et les propriétés d'interface des matériaux. Après des années de développement, elle est désormais largement utilisée dans les domaines des sciences de la Terre, de la science des matériaux et de la fabrication de cellules solaires photovoltaïques. Dans la recherche sur les matériaux, la spectroscopie d'impédance AC peut aider à comprendre en profondeur les propriétés de transport électrique des matériaux. Étant donné que les ions et les électrons ont des réponses complètement différentes aux signaux AC de différentes fréquences lorsqu'ils traversent les grains et les joints de grains, c'est donc un moyen très efficace de distinguer la conduction ionique et électronique et la contribution des grains et des joints de grains. Le photocourant est une caractéristique importante du matériau photovoltaïque avec des applications pratiques. La mesure du photocourant permet d'observer très intuitivement la capacité d'absorption de la lumière du matériau photovoltaïque. La spectroscopie d'absorption des rayons X joue un rôle incomparable dans l'étude des propriétés locales dans des conditions extrêmes grâce à sa sélectivité des éléments et à sa sensibilité aux structures atomiques, électroniques et magnétiques locales. La spectroscopie d'absorption de rayons X en dispersion d’énergie (ED-XAS), en particulier, a été largement appliquée pour de telles études en raison de son optique de focalisation, de son temps d'acquisition court et de sa grande stabilité pendant la collecte des données. Dans ce travail de thèse, des mesures de spectroscopie d'impédance en courant alternatif et de photocourant sous pression ont été réalisées à l'Institut de Physique Atomique et Moléculaire et au State Key Lab

of Superhard Materials de l'Université de Jilin en Chine. Les expériences XAS ont été réalisées sur la ligne en dispersion d'énergie ODE de l'installation de rayonnement synchrotron SOLEIL en France.

L'émergence des matériaux pérovskites hybrides organiques-inorganiques (HOIP) a révolutionné le domaine du photovoltaïque. Au cours des dix dernières années, le rendement de conversion de puissance (PCE) des cellules solaires à base de HOIP a été considérablement amélioré. Cependant, malgré l'amélioration rapide du PCE, les matériaux HOIP ont encore un long chemin à parcourir pour passer du laboratoire à leur application, avec quelques défis à relever: 1) la stabilité à long terme dans l'environnement extérieur; 2) la diffusion des porteurs par les joints de grains dans les matériaux HOIP affectera les performances des dispositifs photovoltaïques, mais les raisons spécifiques ne sont pas encore claires; 3) la migration des ions dans les matériaux HOIP peut affecter l'efficacité de conversion des cellules solaires, ce qui doit être étudié. Parmi une grande variété de matériaux HOIP, le bromure de césium et de plomb ($CsPbBr_3$) présente des propriétés photoélectriques exceptionnelles, une stabilité thermique remarquable et une meilleure résistance à l'humidité par rapport aux autres composés pérovskites organiques-inorganiques, ce qui en fait un candidat idéal pour les futurs dispositifs photovoltaïques.

Les propriétés de transport électrique et les propriétés optoélectroniques du CsPbBr3 ont été étudiées à l'aide d'un dispositif à haute pression basé sur la cellule à enclume de diamant (CED), combiné à des méthodes de spectroscopie d'impédance AC in-situ à haute pression et de mesure du photocourant. Le mécanisme de conduction dans le $CsPbBr_3$ est une conduction mixte ionique/électronique. Il y a des changements discontinus dans les paramètres électriques au point de pression de la transition de phase. De plus, la transition de la conduction mixte ionique/électronique à la conduction électronique pure se produit après l'amorphisation du $CsPbBr_3$. Lorsque la pression augmente, la

contribution des joints de grains à la résistance devient de plus en plus évidente. Mais le joint de grain affecte seulement le changement de sa résistance et n'affecte pas ses propriétés intrinsèques telles que e sens du changement de résistance avec la pression, et la transition induite par la pression de la conduction ionique/électronique à la conduction électronique pure. La réponse photoélectrique du $CsPbBr_3$ peut être améliorée par la pression, le photocourant étant maximum à 1,4 GPa, qui est affecté par la migration des ions. Les ions qui migrent dans le $CsPbBr_3$ peuvent être divisés en deux parties: 1) les ions participant à la migration dans le noir, sans lumière; 2) les ions excités par la lumière pour participer à la migration sous éclairement. Les ions participant à la migration sont excités par la lumière, migrent dans la direction du champ électrique externe et s'accumulent à l'interface pérovskite-électrode pour former un nouveau champ électrique interne. La direction étant opposée à celle du champ électrique externe, ce dernier diminue, ce qui entraîne une diminution progressive du photocourant. En outre, l'évolution de la structure électronique du $CsPbBr_3$ a été étudiée par XAS à haute pression. La variation du spectre d'absorption des rayons X du $CsPbBr_3$ en fonction de la pression et les résultats du calcul théorique du spectre d'absorption confirment directement la transition de phase isostructurale à 1,2 GPa. La pression provoque une diminution continue de la distance Pb-Br, ce qui entraîne des distorsions et des contractions des octaèdres de $PbBr_6$, ce qui induit la transition de phase.

Pour les matériaux 2D en couches, leurs propriétés sont souvent affectées par le nombre de couches et la variation des forces de couplage entre les couches. Sous pression, la distance entre les couches diminue et l'interaction de couplage entre les couches est renforcée, ce qui favorise les transitions structurales et électroniques. La structure fine d'absorption des rayons X étendue (EXAFS) à haute pression peut nous aider à comprendre en profondeur ces types de matériaux, et fournir de nouvelles idées ou directions pour le développement

de nouveaux dispositifs photovoltaïques basés sur ces matériaux. ReS_2 et l'arsenic noir, b-As, sont des représentants de deux types de matériaux en couches 2D.

Pour ReS_2, la pression peut facilement affecter le couplage inter-couche en changeant la distance entre les couches, modifiant ainsi sa structure électronique. Nous avons effectué des mesures EXAFS au seuil Re L3 de ReS_2 et avons finalement déterminé que deux transitions de phase se sont produites à 6,0 et 20,4 GPa, respectivement. Lorsque la pression dépasse 6,0 GPa, l'interaction entre les atomes S inter-couches est renforcée, ce qui entraîne la formation de liaisons de type covalent S-S, la rotation des atomes S autour des atomes Re intra-couche, et la transition de phase de ReS_2 se produit. Lorsque la pression atteint 20,4 GPa, le couplage inter-couche est accru, ce qui entraîne que les différentes couches de ReS_2 passent progressivement d'un empilement désordonné à un empilement ordonné. Nous attribuons les transitions de phase à 6,0 et 20,4 GPa aux transitions intra-couche et inter-couche, respectivement.

Nous avons utilisé une méthode d'analyse similaire pour étudier la transition de phase du b-As sous pression. Les données EXAFS au seuil K de l'As ont été collectées de 0 à 20,1 GPa pour explorer l'évolution de la structure de b-As sous pression. Nous avons constaté que la transition de b-As (A17) à g-As (A7) (l'arsenic gris) s'est produite à 4,7 GPa. La transformation structurale de b-As en arsenic gris n'est pas causée par la compression et l'extension de la structure intra-couche dans une seule direction sous pression, mais plutôt par la formation de liaisons inter-couches et la rupture des liaisons intra-couches. En outre, pour la transition soudaine de l'intensité de la ligne blanche à 10,8 GPa, combinée aux résultats de recherches précédentes, nous spéculons que la transition de la phase gAs à la phase cubique simple se produit à 10,8 GPa.

La structure du présent travail de thèse est la suivante :

- Introduction des connaissances de base et de l'histoire du développement des matériaux énergétiques émergents tels que les pérovskites et les matériaux en couches 2D, puis brève explicationdu rôle des hautes pressions en science des matériaux, puis présentation de nos motivations de recherche ;
- Présentation des techniques expérimentales, telles que la CED, la spectroscopie d'impédance AC et la XAS, utilisées pour les expériences sous haute pression ;
- Présentation des mesures de spectroscopie d'impédance AC, de photo-courant, et de XAS et analyse des résultats de $CsPbBr_3$ sous pression ;
- Présentation des résultats d'EXAFS et étude de l'évolution de la structure électronique de ReS_2 et b-As sous pression ;
- Présentation succincte des collaborations avec d'autres personnes ;
- Résumé, conclusions et perspectives de ce travail.

De plus amples informations sur les détails techniques concernant les techniques expérimentales et l'analyse des données peuvent être trouvées dans la section texte suivante.

Contents

Chapter 1

High-pressure research on emerging energy materials: background

1.1 Emerging energy materials

The ever-increasing population of the world and the rapid development of industrialization have led to rising energy demand. Traditional fossil fuels such as oil, coal, and natural gas provide the continuous impetus for the development of modern society and the economy. The side products of fossil fuels combustion, such as toxic CO, CO_2, and SO_2, are harmful to human health and cause global warming.[1-5] Environmental concerns related to fossil fuels have driven scientists to explore alternative means for energy production and storage. New and innovative materials offer new options for solving these problems.[6] The exploration and research of emerging energy materials have always been carried out around the development and utilization of renewable clean energy. As shown in Figure 1.1, people have access to clean and renewable energy in a variety of ways and make use of it.

Among different green energy technologies, solar energy has been considered to be a very promising technology. The solar energy that radiates to the earth every day is more than the sum of the energy consumed every year in the world.[7] Obtaining and converting solar energy can help solve current

energy and environmental problems. Perovskite solar cell materials and two-dimensional layered materials have attracted worldwide attention as solar harvesting materials because of their remarkable photovoltaic properties.

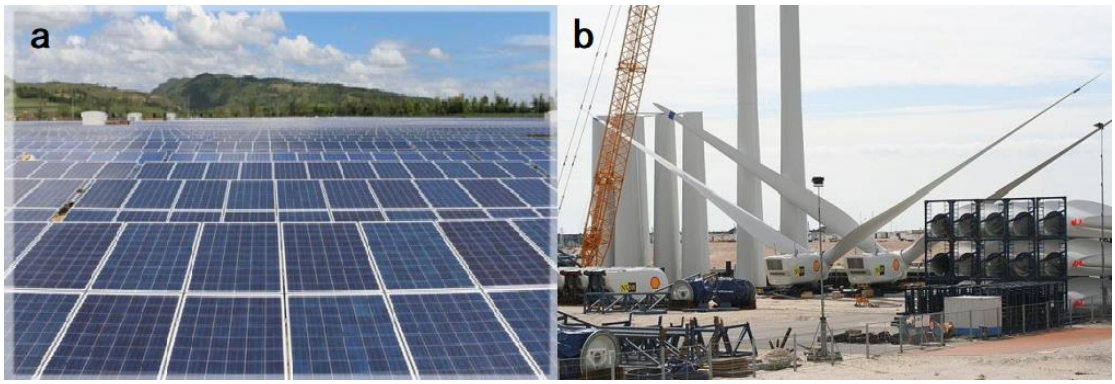

Figure 1.1 Access to clean and renewable energy: a) Photovoltaic solar panels; b) Wind power components.

1.1.1 Perovskite solar cell materials

Perovskites are a class of crystalline materials with the formula ABX_3, in which A is a monovalent organic cation (MA^+ (MA = CH_3NH_3), FA^+ (FA = $CH(CH_2)_2$)…), or an inorganic cation (such as Cs^+, Rb^+…), B is a metal divalent cation (Pb^{2+}, Sn^{2+}, Ge^{2+}…), X is a monovalent halogen element (Cl^-, Br^- and I^-…).[8] The structure comprises a set of fully corner-sharing $[BX_6]^{4-}$ octahedra organic cations coordinated by 12X anions as shown in Figure 1.2. By changing the compositions of A, B, and X, one can tune their optoelectronic properties to discover more properties in perovskite-structured photovoltaics.

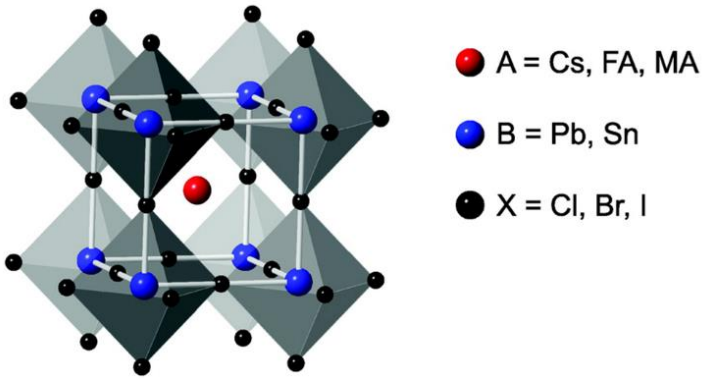

Figure 1.2 The structure of perovskite.

In 2009, Kojima and Miyasaka et al. applied organic-inorganic hybrid perovskites $CH_3NH_3PbBr_3$ ($MAPbBr_3$) and $MAPbI_3$ to sensitize solar cells for the first time, and obtained conversion efficiencies of 3.1% and 3.8%, respectively,[9] which opened the prelude to the research of perovskite solar cells. In 2012, the Park group and Grätzel group collaborated to use solid spiro-OMeTAD instead of traditional liquid electrolyte as a hole transport material, and $MAPbI_3$ as a light-absorbing material to develop all-solid perovskite solar cells (PSCs), in Figure 1.3. The power conversion efficiency (PCE) has been increased to 9.7%, and the stability has been greatly improved. It can work stably for about 500 hours. This research result has laid the foundation for the application and development of hybrid organic/inorganic perovskite (HOIP) materials in solar cells.[10]

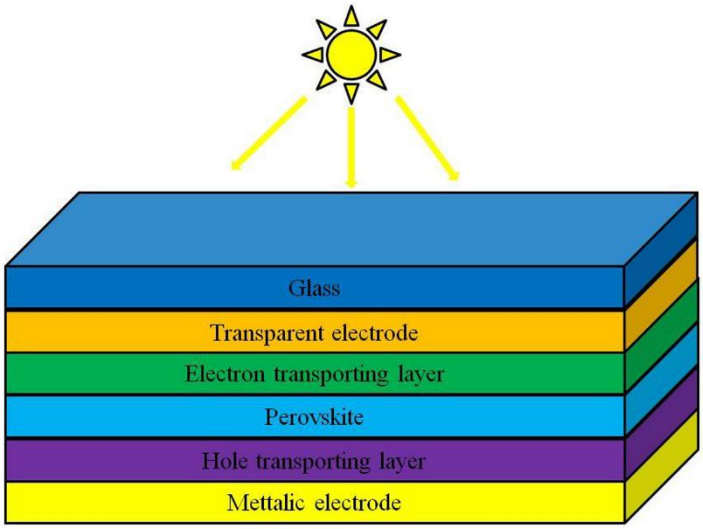

Figure 1.3 The structure of perovskite solar cells.

A year later, the Grätzel and Snaith groups further improved the efficiency of perovskite solar cells by optimizing the cell structure and material synthesis technology, breaking through 15%.[11-12] Because of the great achievements made in the research of perovskite solar cells in just a few years, both Nature and Science regard perovskite solar cells as one of the major scientific advances in 2013.[13] After that, due to the many advantages[14-21] and wide-ranging

applications[22-30] of perovskite materials, the emergence of new thin-film technologies, the application of new materials and new manufacturing processes, and the optimization of structure and surface interface engineering,[31-39] the development of perovskite solar cells was pushed to a climax. In the past ten years, the efficiency of perovskite solar cells has been continuously improving and has reached 25.7% today, as shown in Figure 1.4.

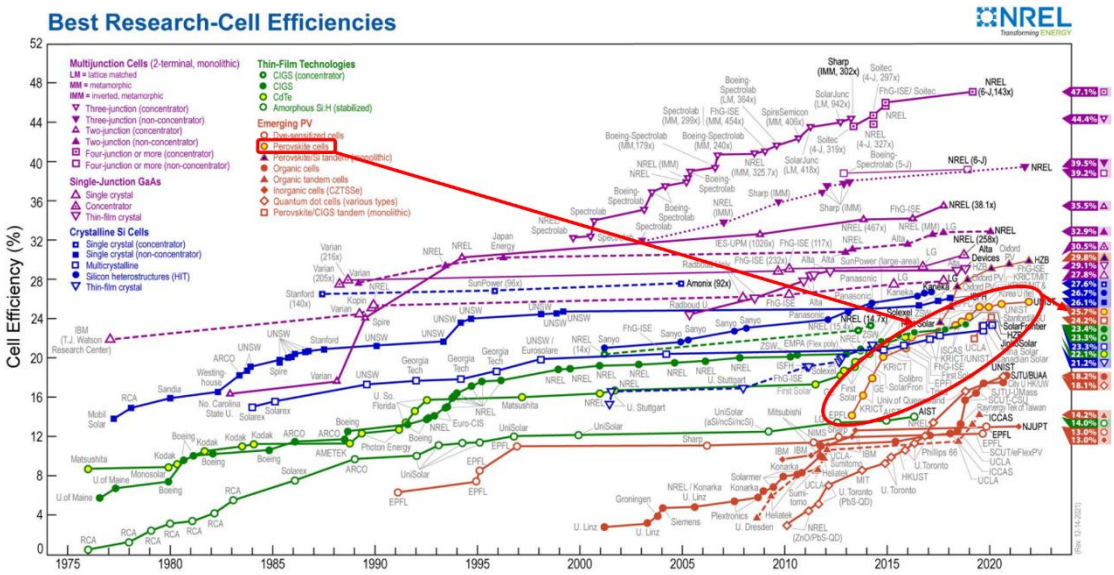

Figure 1.4 The Best Research-Cell Efficiency Chart.[40]

1.1.2 Two-dimensional layered materials

Two-dimensional (2D) layered materials refer to a class of materials artificially derived from layered van der Waals solids,[41-42] in which the atoms are held together by tight covalent or ionic bonds along 2D (in-plane) directions to form atomic layers, while the atomic layers are bonded together by weak van der Waals interactions along the third-dimensional (out-of-plane) direction.[43-44] Some 2D layered materials are shown in Figure 1.5.

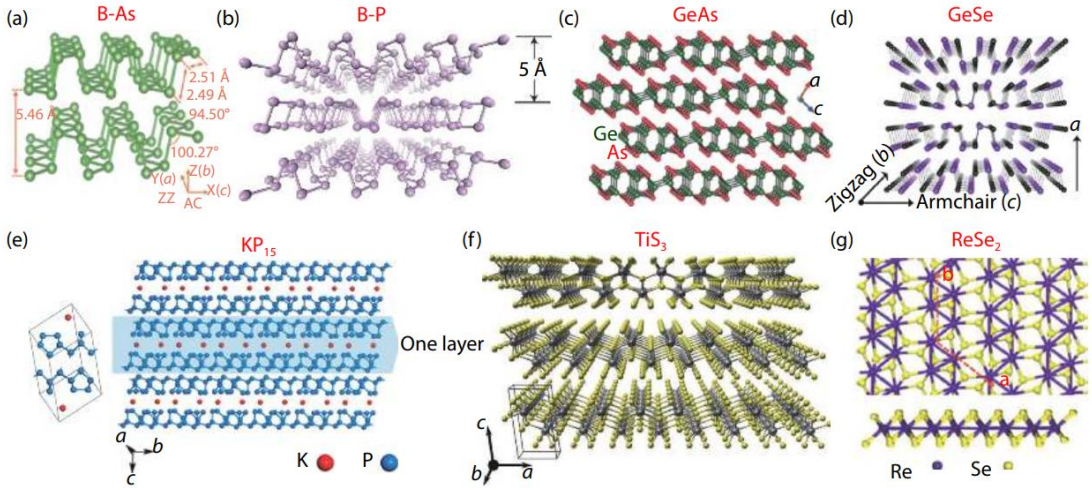

Figure 1.5 The crystal structures of several types of representative 2D layered materials (a) orthorhombic black-arsenic.[45] (b) Orthorhombic black-phosphorus.[46] (c) Monoclinic GeAs.[47] (d) Orthorhombic GeSe.[48] (e) Triclinic KP_{15}.[49] (f) Monoclinic TiS_3.[50] (g) Triclinic $ReSe_2$.[51]

Such weak van der Waals interactions between neighboring layers make it possible to cleave the layered materials into individual freestanding few-atom-thick or even single-atom-thick layers via mechanical[52-53] or liquid phase exfoliation[54-55] techniques. So far, more than ten different 2D semiconductors (with bandgap values spanning from a few millielectronvolts up to several electronvolts) have been experimentally isolated and there are potentially hundreds more that could be isolated soon. 2D materials have attracted considerable attention due to their exciting optical and electronic properties and demonstrated immense potential for next-generation solar cells and other optoelectronic devices. With the scaling trends in photovoltaics moving toward thinner active materials, the atomically thin bodies and high flexibility of 2D materials make them the obvious choice for integration with future-generation photovoltaic technology. Discovered in 2004, graphene, composed of a single layer of carbon atoms bonded together in a hexagonal honeycomb lattice, is the most famous 2D layered material[56] and has plenty of appealing electronic, optical, mechanical, and thermal properties.[57-59]

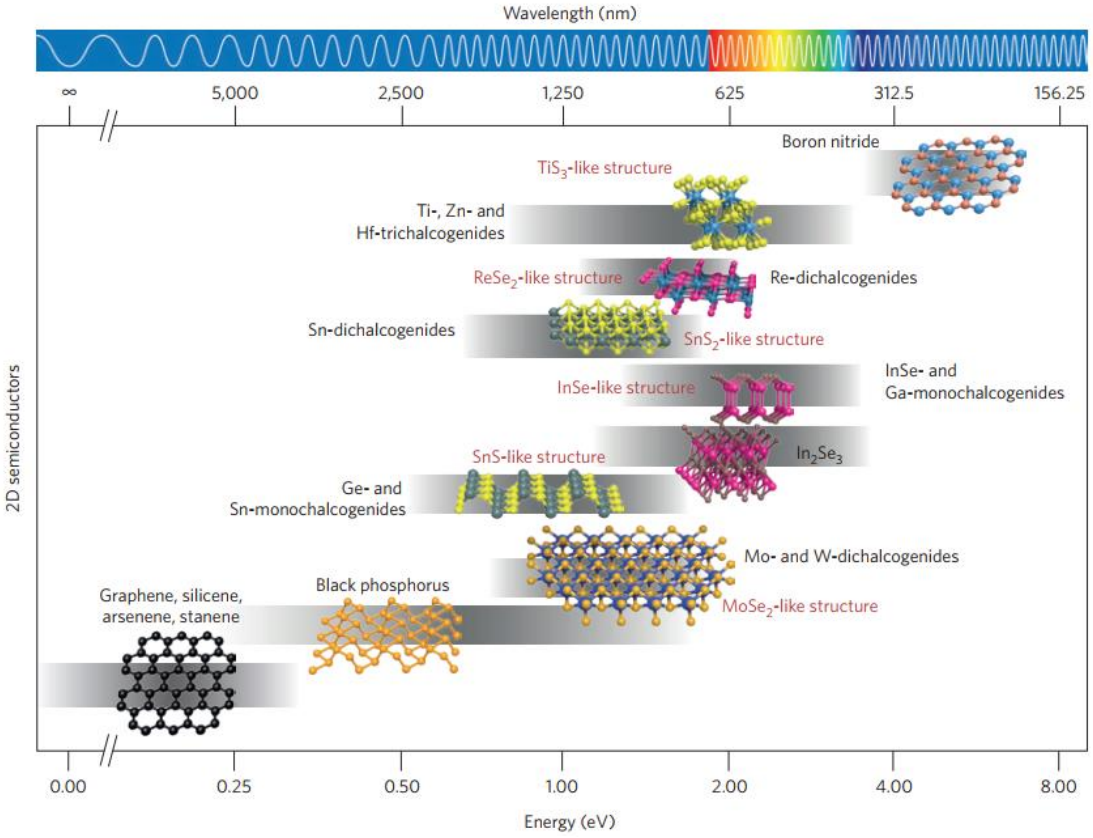

Figure 1.6 Comparison of the bandgap values for different 2D semiconductor materials families. The crystal structure is also displayed to highlight the similarities and differences between the different families. The gray horizontal bars indicate the range of bandgap values that can be spanned by changing the number of layers, straining, or alloying. This broad bandgap range spanned by all these 2D semiconductors can be exploited in a wide variety of photonics and optoelectronics applications, such as thermal imaging, fiber optics communication, photovoltaics, displays, and light-emitting diodes.[60]

Following the footprints of graphene, other atomically thin, layered semiconducting 2D materials emerged with their inherent distinctive properties.[60] With an intrinsic bandgap and different crystal structures, these 2D materials have become promising candidates for a wide variety of applications relating to next-generation electronics and optoelectronics.[42, 61-71] Figure 1.6 shows a catalog of 2D materials with varying bandgap utilized for various applications in different wavelength regimes.

Specifically, research and development of 2D materials like transition metal

dichalcogenides (TMDs)[42, 72-73], and black phosphorus[74-76] have progressed rapidly due to their excellent mechanical properties, which have played extensive roles in designing flexible and stretchable next-generation electronic devices.[77-78] These materials have attracted much attention not only due to their semiconducting nature but also due to their ultralightweight, high Young's modulus,[79] and high tensile strength. Also, the in-plane and out-of-plane mechanical properties of these materials are different from each other. Recently, they have been found to play promising roles in photovoltaic devices,[80-83] as shown in Figure 1.7.

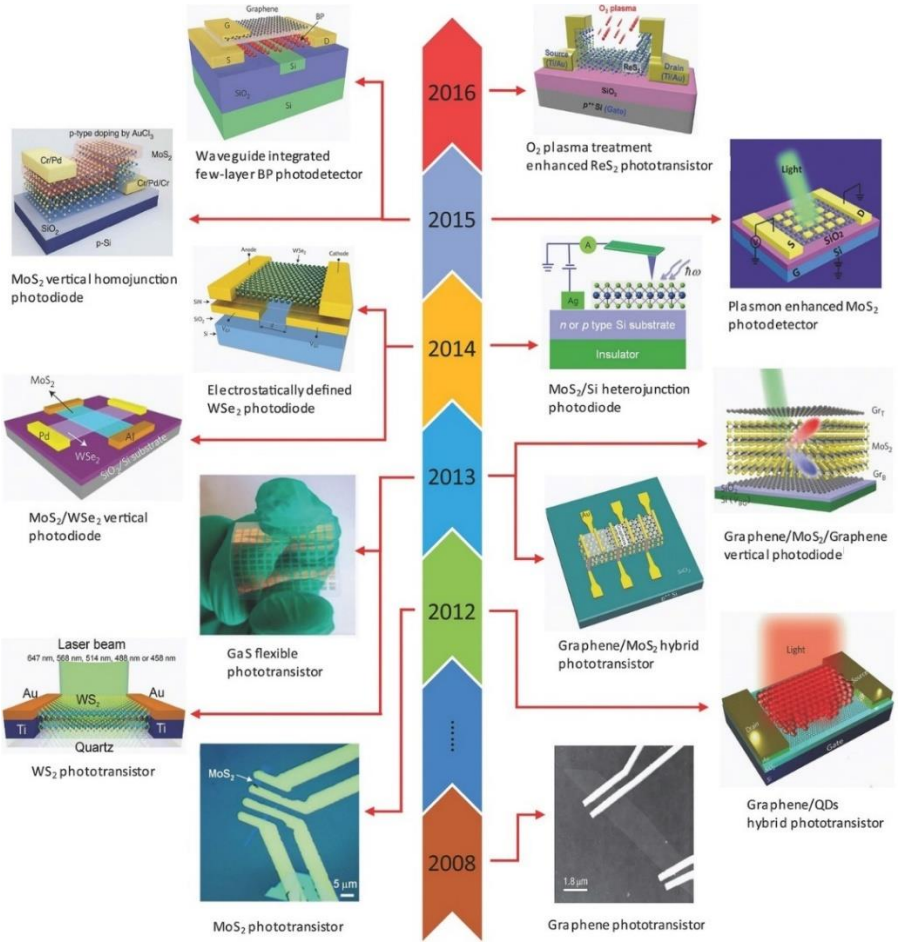

Figure 1.7 Timeline showing the development of the applications of graphene and other 2D layered semiconductors in photodetectors based on different principles.

1.2 The role of pressure in the material sciences

Pressure is a fundamental thermodynamic variable that can be easily tuned in the experiment, leading to significant advances in such extensive areas of science and technology as condensed matter physics, geophysics, astrophysics, chemistry, biology, etc.[84-88] Pressure possesses one of the greatest ranges among all physical parameters, over 60 order of magnitude.[89] High-pressure investigations are useful for understanding the properties of molecules and materials. From the fascinating phenomena represented in Figure 1.8, it is very easy to understand the origin of the increasing interest in high-pressure studies. The significant effect of high pressure is the shortening of interatomic and intermolecular distances accompanied by the reduction of volume. On one hand, high-pressure studies can acquire knowledge about the behavior of materials under extreme conditions which is necessary for understanding the physical and chemical evolutions occurring in the Earth and planetary interiors[90]. On the other hand, in many cases, scientists and engineers can use the high-pressure technique to synthesize innovative materials with high elastic moduli and hardness.[91-92] Moreover, these materials may have interesting optoelectronic, thermal, magnetic, semiconducting, or superconducting properties which can be recovered to ambient conditions. Due to substantial technological advances during the past few decades, research in the field of high-pressure chemistry has also progressed significantly.[93] Furthermore, the treatments of biological materials under high pressure are of considerable interest.[94] Because of its outstanding importance, high-pressure science and technology are giving significant contributions to our deepest understanding of the ultimate properties of matter.[95]

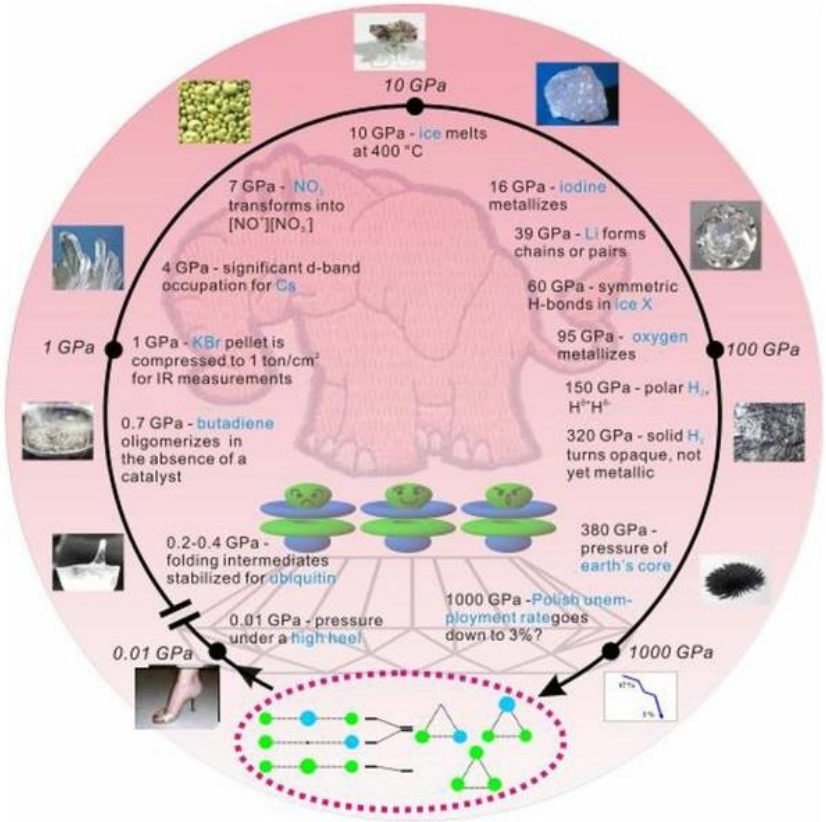

Figure 1.8 The selected fascinating phenomena under high- pressure with selected examples.[96]

High pressures can be relatively easily applied to small samples in a controlled manner in the laboratory, and the resulting changes in material properties can be explored systematically using in situ high-pressure techniques. During the past decades, high-pressure scientists and engineers have focused on pressure cell modifications and the integration of analytical techniques with high-pressure apparatus.[97] As a result of the developments in high-pressure techniques, such as the diamond anvil cell (DAC) and the large volume press (LVP),[98-99] it is possible to significantly expand the pressure-temperature range under static conditions. Principles of high-pressure experiments using DAC will be briefly introduced in Chapter 2.

The static compression experiments require in situ measurements under such extreme pressure and temperature conditions. Many kinds of in situ measurement methods based on high-pressure apparatus,[97] such as Raman

scattering, X-ray diffraction (XRD), electrical measurements, magnetic studies, will enable detailed insight into the changes of atomic structures in materials. Due to the very small size of the samples (of order 100 μm), the brilliant and small beams of synchrotron radiation have a profound effect on high-pressure research. The advent of synchrotron radiation as a light source allows nanometer-sized crystals to be used because an intense beam can be focused down to a size smaller than that of samples in DAC. Additionally, using synchrotron radiation techniques, both the quality of signals and the measurement time have improved significantly, and the available pressure-temperature range is now much larger than before.[100]

1.3 The motivation for this thesis work

The emergence of organic-inorganic hybrid perovskites (HOIPs) has revolutionized the field of photovoltaics. The simple preparation process, low cost, and high conversion efficiency give this material good application prospects in the future. However, perovskite solar cells still have a long way to go from the laboratory to their application with some challenges:

1. Long-term stability under external environment (such as moisture, temperature, light, etc.);

2. In practical applications, the scattering of carriers by grain boundaries in HOIP materials will affect the performance of photovoltaic devices, and the specific reasons are unclear;

3. The ion migration in perovskite will affect the conversion efficiency of solar cell devices, and the ion migration behavior in HOIP materials also needs to be explored.

Here, we selected HOIP materials to study the electrical transport properties under high pressure. The structure of the HOIP material can be changed

through high pressure. Impedance spectroscopy can be used to analyze the conductivity types of HOIP materials such as electronic conduction, ionic conduction, or mixed conduction. In addition, impedance spectroscopy can also distinguish the contribution of grains and grain boundaries to the resistance and the transport mechanism. The photocurrent can reflect the photoelectric response-ability of the material. The larger the photocurrent, the higher the conversion efficiency of the device. X-ray absorption spectroscopy (XAS) can provide structural information on the local environment surrounding the absorbing atom, which can help us gain insight into the electronic and geometric evolution of HOIP materials under pressure.

For 2D layered materials, their properties are often affected by the number of layers and the variation in the coupling strength between layers. Under pressure, the interlayer distance of layered 2D materials will be reduced, and the interlayer coupling interaction will be enhanced, which promotes transition in their lattice and electronic structures. High-pressure EXAFS can help us to understand these kinds of materials deeply, and provide new ideas or directions for the development of new photovoltaic devices based on these materials.

Chapter 2

Experimental techniques: basic principles and applications

2.1 High-pressure techniques

2.1.1 Diamond anvil cell (DAC)

Since the pioneering work of P. W. Bridgman in the early 1900s, massive hydraulically driven Bridgman-anvil and piston-cylinder apparatus dominated high-pressure science until the late 1960s. From the advent of the diamond anvil cell (DAC) in the mid-1960s, due to its easy assembly and operation, many non-specialized laboratories became able to develop high-pressure experiments.[101] Diamond is the hardest known bulk material with high incompressibility and transparency, which is an ideal material for a high-pressure device.

Figure 2.1 illustrates the basic principle of DAC: the sample is placed in a hole of a gasket with a pressure transmitting medium between the flat faces (culets) of two opposed diamond anvils and its pressurization is achieved by applying a force on the anvil. The applied pressures depend on the culets' diameter of diamond anvils. Typically, a 500 μm diameter of the culet allows pressures up to ~25 GPa, while a 100 μm diameter allows pressures up to ~120 GPa.

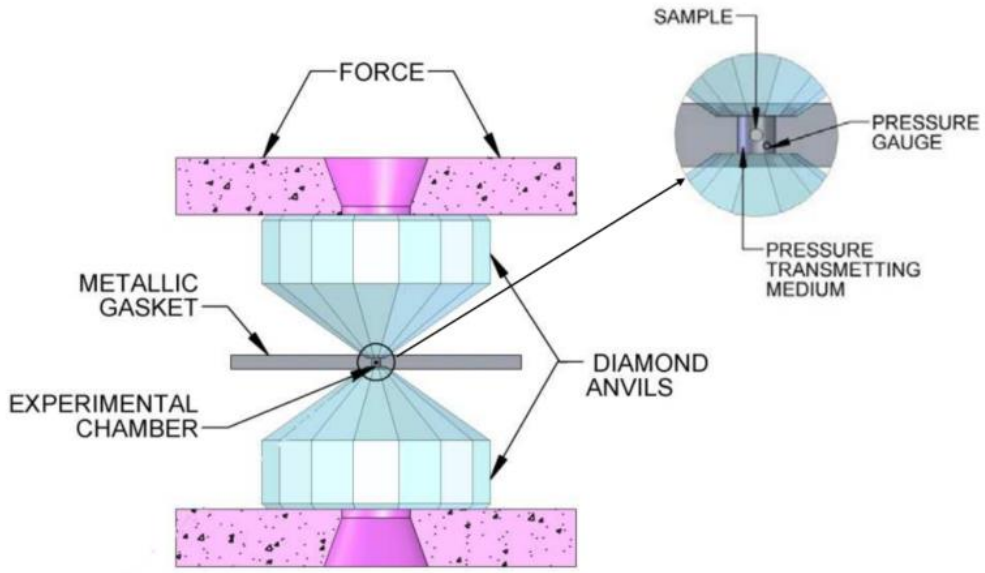

Figure 2.1 Principle of the diamond anvil cell.

DAC is currently the device that reaches the highest static pressure (~400 GPa).[102] One of the greatest advantages of DAC is the transparency of its anvils. So a sample can be observed during compression and in situ studied by various techniques: X-ray diffraction, X-ray spectroscopy, Raman, IR, UV, etc. There are plenty of pressurizing mechanisms and therefore plenty of kinds of DACs.[103] In our studies, we use two kinds of DAC, one is a mechanically pressurized DAC (MPDAC), and the other is membrane DAC (MDAC), which is a metallic toroidal membrane inflated with helium to push on the piston to provide pressure, as shown in Figure 2.2.

Figure 2.2 The picture of (a) MPDAC and (b) MDAC, (c) a stainless steel membrane is located in the cover. To generate pressure, helium is inflated into the membrane through the capillary tube.

Because electrical measurements require lead-in electrodes, the MPDAC provides a wide window to link electrodes and measurements. For MDAC, the membrane generates axial force, which is therefore homogeneously extended over all the pistons, permitting precise control of the pressure. The membrane is linked by a metallic capillary to a He bottle through a pressure pneumatic drive system (PDS). By using MDAC, pressure on the sample can be easily tuned without touching or displacing the cell, which is a great advantage for in situ synchrotron measurements. Using micro-valves also permits to "keep" an obtained pressure and meanwhile disconnect the cell from PDS for transportation or keeping it independently.

2.1.2 Measuring high pressures

The majority of DAC studies utilize one of two strategies for pressure measurement: (1) measuring the unit cell size of a material whose equation of state (EoS) is well known; (2)measuring the position of the fluorescence line of ruby (Al_2O_3 doped by Cr^{+3}) or YAG ($Y_3Al_5O_{12}$). The displacement of the fluorescence line as a function of pressure is well known. Ruby fluorescence is very commonly used for pressure measurement and has been widely used in the present work. Ruby is chemically inert and has strong luminescence when hit with green laser light. There are two peaks (R_1 of 6942.48 Å and R_2 of 6927.0 Å) in the luminescence spectrum of ruby at ambient conditions. The shift of R_1 with pressure has been well calibrated.[104-108] Up to 20 GPa, it is linear, whereas at higher pressure it can be determined from the following equation:[108]

$$P = \frac{0.274 \cdot \lambda_{R1}(0)}{B}\left[\left(\frac{\lambda_{R1}(P)}{\lambda_{R1}(0)}\right)^{B} - 1\right] \qquad 2.1$$

where B is a parameter related to the degree of hydrostaticity on the sample: B = 5 for non-hydrostatic conditions and B = 7.665 for conditions close to hydrostaticity. As the pressure increases both R_1 and R_2 broaden until there is a

complete overlap at a pressure. The signal-to-noise ratio decreases with increasing pressure, making precise high-pressure measurement more difficult. The position of the R_1 peak is also dependent on temperature.[109] When ruby is heated, its luminescence peaks broaden and decrease in intensity to a point just above 400°C where its position can no longer be measured. Despite this, for high-pressure experiments in DACs below 200°C ruby is the best pressure marker.

2.1.3 Pressure transmitting medium

The pressure transmitting medium (PTM) for DACs are soft solids and liquids or fluids. The role of PTM is to transmit pressure to the sample while minimizing the shear stress transmitted to the sample. Common PTM, which replaces the 4:1 mixture ethanol-methanol, is N_2, Ar, He, Ne, ethanol, methanol, and NaCl. "Gasses" such as He, Ne, or Ar are a highly desirable PTM, due to their chemical inertness. They are loaded into the cell only in a fluid state. The liquid PTM provides a true hydrostatic environment. However, many fluid media crystallize as pressure increases; thus a media that works well at lower pressure may crystallize and introduce error at high pressures.

2.1.4 Fabrication of DAC Gaskets

The DAC gasket is a thin sheet of metal that has a small hole about 1/2 diameter of the diamond anvil (cutlet face). Gaskets are typically prepared by pressing the diamonds into a thin metal sheet and then drilling a tiny hole through the indented portion of the gasket. The holes can be done either by electroerosion or by a high-energy focused ion beam. The indentation thickness also influences the maximum reachable pressures. Rhenium is commonly used for the gasket, but tungsten, stainless steel 301, Kapton, c-BN, Cu, Be are also mentioned in the literature.

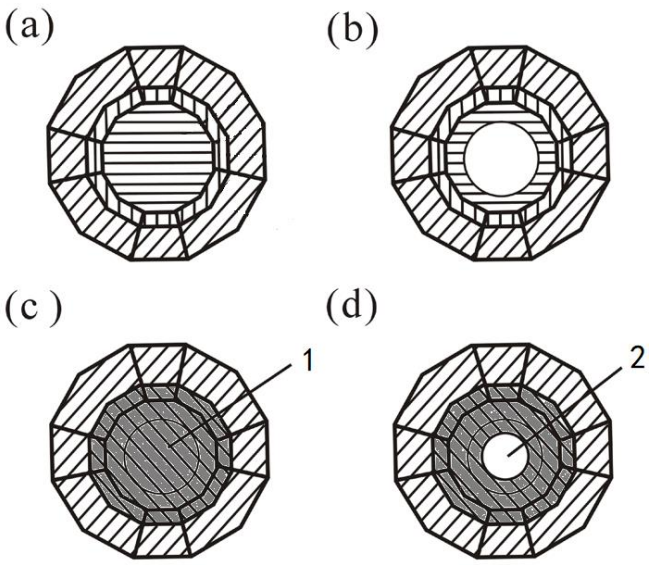

Figure 2.3 The fabricating process of the gasket: 1 is the insulating powder protective layer, 2 is the sample chamber.

The fabricating process of the gasket we used in this thesis (taking stainless steel T301 as an example) is shown in Figure 2.3:

(a) Select stainless steel T301 with a diameter of 10 mm and a thickness of 200 μm, and place it in the DAC (keeping the center coaxial) to pre-indented the T301 sheet with a thickness of ~50 μm;

(b) Drill a hole with the diameter of ~150 μm (smaller than the diameter of the diamond anvil) in the center of the pre-indented gasket;

At this time, the completed gasket can be used for optical measurement, but if it is to be used for electrical measurement, the gasket needs to be insulated.

(c) Press the insulating powder obtained by mixing alumina and epoxy resin according to a certain proportion into the hole of the gasket, to insulate the electrode and the gasket;

(d) Finally, use a laser to drill a hole in the center of the gasket with a diameter of ~100 μm (smaller than the diameter of the hole in the second step) as a sample champer to ensure insulation between the sample and the gasket.

2.1.5 Integration of thin-film electrodes on diamond

Traditional high-pressure electrical measurements are often performed by manually placing platinum (Pt) electrodes in the DAC. Although this method is relatively simple and will shorten the experimental preparation time, there are still some disadvantages: when the pressure reaches a high level, the Pt electrode is easily "tear-off" and the experiment will be interrupted in force; the platinum electrode will be stretched and deformed under high pressure, which will have a bad influence on the experimental measurement and data acquisition and analysis. The thin-film electrodes will not have these problems, and after more than ten years of development, the integration skill of thin-film electrodes has become very mature.

We take the integration of parallel plate electrodes as an example to introduce the integration process of thin-film electrodes, as shown in Figure 2.4:

(a) The diamond is placed in a mixture of concentrated sulfuric acid and nitric acid then heated and boiled, in this way, the surface of the diamond can be completely cleaned;

(b) Using magnetron sputtering equipment to sputter molybdenum (Mo) film on the cleaned diamond surface as electrode material;

(c) Photolithography of Mo thin-film electrodes on the diamond surface using UV lithography machine;

(d) Sputtering a layer of aluminum oxide film on the electrode after photolithography to insulate and protect the Mo electrode;

(e) The window connecting the electrodes was etched on the diamond sputtered with the alumina film, then the conductive silver glue was used to glue the wires to the window to connect the electrodes.

The advantage of the parallel plate electrode is that the electric field generated inside the sample is homogenous, and the data obtained are more accurate.

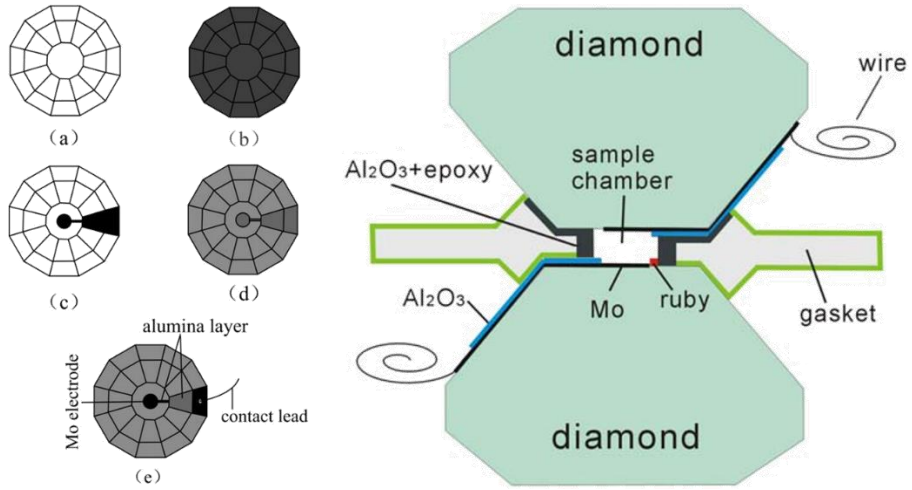

Figure 2.4 Parallel plate electrode model and assembly schematic.

2.2 Electrochemical Impedance Spectroscopy

R represents the resistance of the circuit element to the current flow. Ohm's law defines resistance as the ratio of voltage to current: R=E/I and only applies to circuit elements that have only one ideal resistance. An ideal resistor needs to satisfy several conditions: 1) Ohm's law is satisfied in all current and voltage ranges; 2) The resistance value is independent of frequency; 3) The AC voltage and the AC current through the ideal resistor are in the same phase. However, in the real world, there are many circuit elements with more complex behavior. These circuit elements force us to abandon the simple concept of resistance and introduce impedance. Similar to resistance: Impedance represents the resistance of a circuit to current flow. Unlike resistance, impedance is not limited to the properties of the above resistance.

Electrochemical impedance spectroscopy (EIS) measurements are usually performed by applying an AC potential to a given system and measuring the current through the system. Suppose we apply a sinusoidal AC potential, the

response to the potential is an AC current signal. This current signal can be analyzed as a sum of sinusoidal functions (Fourier series). In a linear (or pseudo-linear) system, the response of the current is a sine wave of the same frequency as the potential, but the phase is shifted as shown in Figure 2.5.

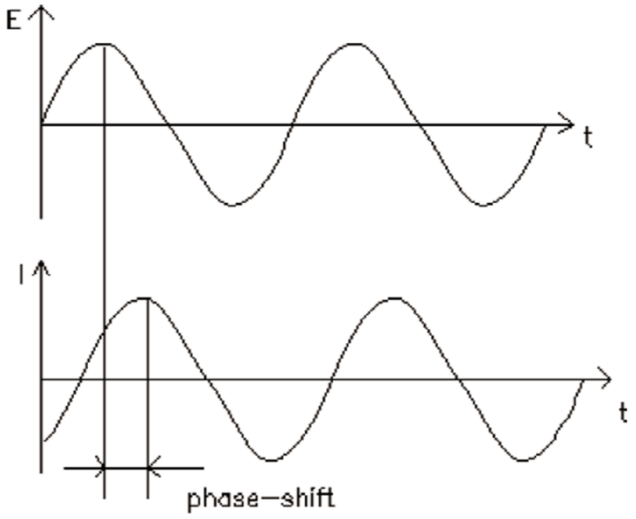

Figure 2.5 Sinusoidal Current Response of Linear Systems

The excitation signal (AC potential) is a function of time:

$$E_t = E_0 \sin(\omega t) \qquad 2.2$$

where E_t is the potential at time t, E_0 is the amplitude of the AC signal, and ω is the angular frequency (ω=2πf). In a linear system, the response signal (AC current) I_t is shifted by a phase angle $\emptyset$ and has a different amplitude than I_0:

$$I_t = I_0 \sin(\omega t + \emptyset) \qquad 2.3$$

Analogously to Ohm's law, impedance can be defined as:

$$\mathrm{Z} = \frac{E_t}{I_t} = \frac{E_0 \sin(\omega t)}{I_0 \sin(\omega t + \emptyset)} = Z_0 \frac{\sin(\omega t)}{\sin(\omega t + \emptyset)} \qquad 2.4$$

If the excitation signal is taken as the X-axis and the response signal is taken as the Y-axis, the resulting graph is an ellipse called a "Lissajous Figure" (see Figure 2.6). The Lissajous Figure on the analysis oscilloscope screen is an impedance spectroscopy measurement method before existing impedance

spectroscopy measurement instruments were available.

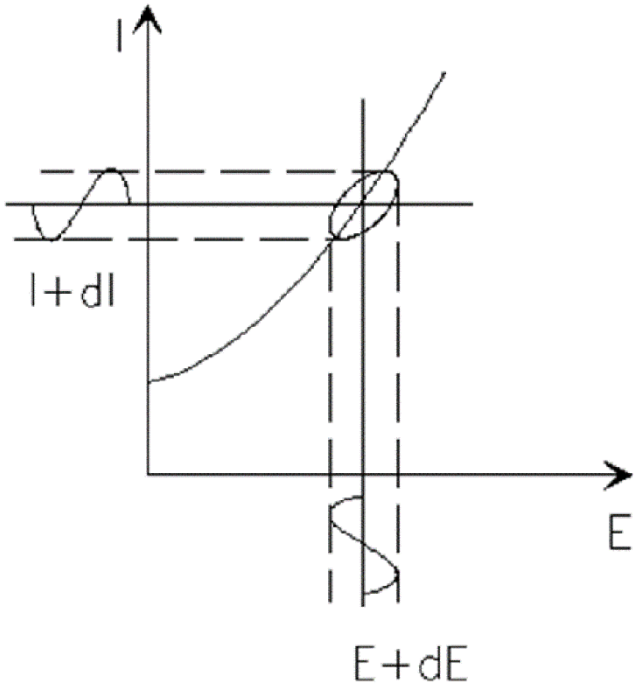

Figure 2.6 The Lissajous Figure.

With Euler's formula:

$$\exp(j\phi) = \cos\phi + j\sin\phi \qquad 2.5$$

The impedance can be converted into a complex form, and the excitation and response signals can be written as:

$$E_t = E_0 \exp(j\omega t) \qquad 2.6$$

$$I_t = I_0 \exp(j\omega t - \emptyset) \qquad 2.7$$

The impedance is represented as a complex number:

$$\mathrm{Z}(\omega) = \frac{E}{I} = Z_0 \exp(j\emptyset) = Z_0(\cos\emptyset + j\sin\emptyset) \qquad 2.8$$

The expression of Z(ω) consists of a real part and an imaginary part. Taking the real part as the horizontal axis and the imaginary part as the vertical axis, we get the "Nyquist Plot" of the impedance spectrum (see Figure 2.7).

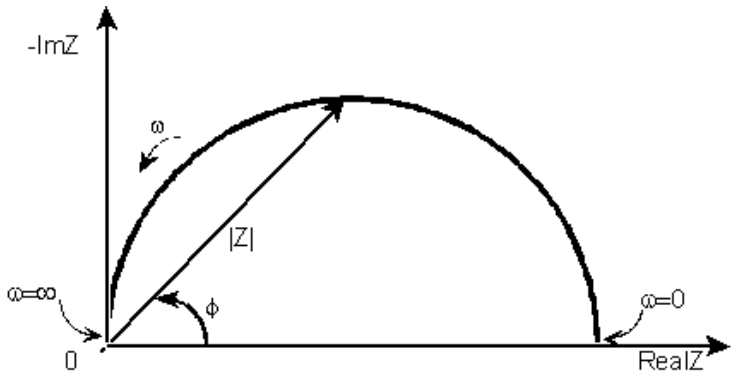

Figure 2.7 Nyquist Plot with Impedance Vector.

Note that in this plot, the vertical axis is negative, and each point on the graph corresponds to a frequency. Figure 2.7 shows the high to low frequencies of the corresponding data from left to right. On a Nyquist plot, impedance can be represented as a vector (arrow) of length $|Z|$. The angle $\emptyset$ between this vector and the horizontal axis is called the "phase angle".

AC impedance spectroscopy is a very important experimental technique to study the electrical properties and surface interface properties of materials. After years of development, it is now widely used in the fields of earth science, material science, and solar cell photovoltaic device manufacturing. In materials research, the measurement of AC impedance spectroscopy can help us deeply understand the electrical transport properties of materials. Since ions and electrons have completely different responses to AC signals of different frequencies when passing through grains and grain boundaries, therefore, it is also a very effective way to distinguish between ionic and electronic conduction and the contribution of grains and grain boundaries to matter.

2.3 Synchrotron radiation applications in high-pressure research

As an important and matured experimental method for probing materials' structure, synchrotron radiation attracts a huge amount of users including condensed-matter physicists, physical chemists, and chemical biologists to investigate the properties of matter by its unparalleled capability. High-pressure

experiment technologies provide a powerful probe for our understanding of the physical properties of molecules and materials. More and more researchers to take advantage of the unique characteristics of synchrotron radiation for high-pressure research, including a) high intensity in a broad energy spectral range, b) high brilliance (small angular divergence), c) tunable energy with the use of a monochromator, d) pulsed time structure, e) coherence, and f) high polarization of the radiation. The combination of high pressure and synchrotron radiation provides a significant and effective method to explore the detailed information of structure and physical properties under extreme conditions. Significant advances have occurred in high-pressure synchrotron X-ray diffraction, extended absorption, inelastic scattering, imaging, and emission spectroscopy. With the steady development of high-pressure techniques combined with synchrotron radiation, new windows are opened for exploring the novel behaviors of materials under extreme conditions, including atomic coordination, structures, and bonding character.[95]

2.3.1 General description of synchrotron radiation

Photon radiation occurred in the bending magnet of the synchrotron storage ring due to electrons deflecting is called synchrotron radiation. It dramatically differs from conventional radiation from the X-ray tubes. The following features of synchrotron radiation compared to ordinary one can be underlined:

- spectral continuity over a range from infrared to X-rays;
- small divergence of emission in the vertical plane;
- flux and luminance billions of times greater than those of classic sources of X-rays;
- linear and circular-polarization;
- temporal structure in pulses;

- certain spatial and temporal coherence.

Due to these qualities, synchrotron radiation is a particularly useful tool for providing in situ experiments, especially under extreme conditions.

The synchrotron is an accelerator of electrons. The general scheme of synchrotron construction is presented in Figure 2.8.

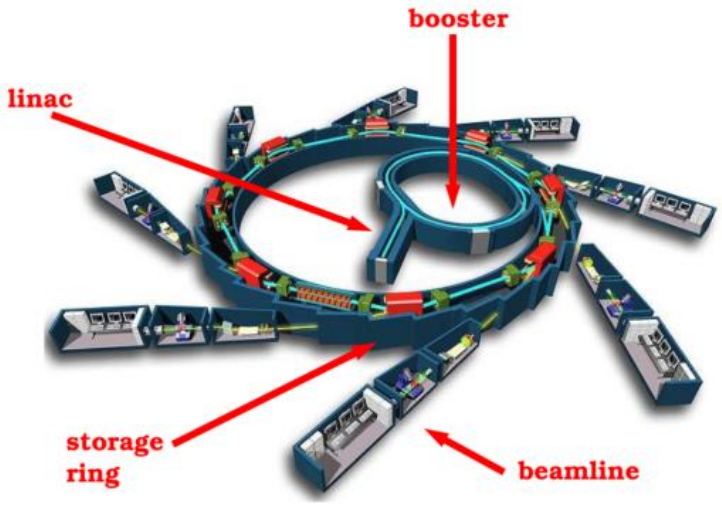

Figure 2.8 General arrangement of 3rd generation synchrotron.

A synchrotron can be divided into three main parts: Linear particle accelerator (LINAC); booster and storage ring with beamlines. The electrons produced and initially accelerated in LINAC are injected into the booster where they are accelerated up to GeV level in synchrotron mode. Finally, the electrons are injected into the storage ring where their circulation becomes stable in time and the electron energy reaches the "working value" (usually it is from 2 to 8 GeV).

In general, beamlines deliver X-ray beams from three different X-ray sources: wiggler, undulator, and bending magnet. Wiggler and undulator are insertion devices (ID) with periodic magnetic structures in the synchrotron storage ring. Their constructions are very close to each other. These magnetic structures, made up of a complex array of small magnets, force the electrons to follow an undulating, or wavy, trajectory (Figure 2.9). The magnetic bremsstrahlung

electromagnetic radiation is emitted at each consecutive bend. Consequently, the total quantity of emittances from one electron is significantly higher than in a bending magnet. Thus, both IDs deliver increased spectral brilliance compared with bending magnets (see Figure 2.9).

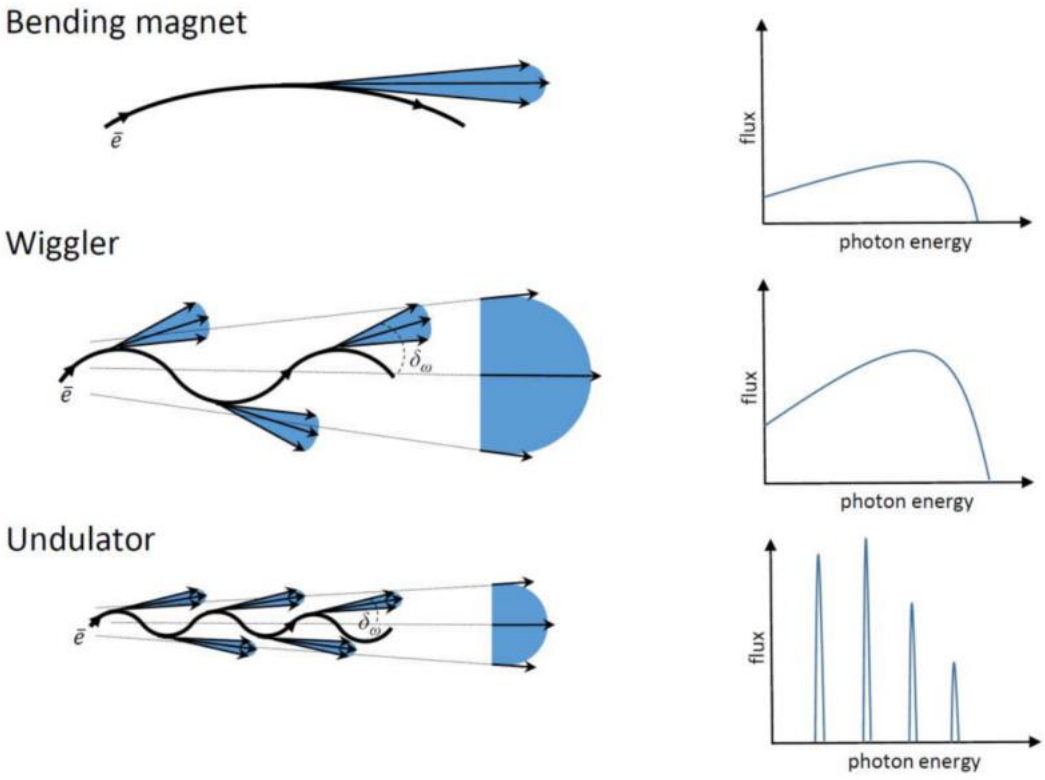

Figure 2.9 Different synchrotron radiation features; where δ_ω is a maximum deviation of electron bunch from the main trajectory.

Nevertheless, there is a difference between radiation emitted by wigglers and undulators. In the case of undulators, due to relatively weak magnet dipoles are, the electrons have only slightly deviated from their trajectory (a small value of δ_ω). Interference occurs between the radiations emitted by the same electron at different points along the trajectory. Due to interference at low δ_ω value and overlapping of emitted light, the flux of undulator radiation is dramatically higher than other IDs. The emitted photons are concentrated at certain energies (called harmonics, see Figure 2.9). By varying the gap between the rows of magnets the quantity and relative intensities of harmonics can be changed. The wigglers contain a less quantity of magnet dipoles but have a considerably

stronger periodic magnetic field. Because of this fact, the electron deviations are significantly larger (rather big δ_ω value), the interference effects between the emissions from the different poles can be neglected and the overall intensity is obtained by summing the contribution of the individual poles. The flux of such radiation is lower than that from the undulator. At a big δ_ω value, total harmonics number and their width increase, leading to a continuous photon spectrum (the same as bending magnet). Unlike undulator, wiggler delivers a white beam with flux a few times higher than the bending magnet.

2.3.2 Synchrotron radiation high-pressure techniques

Synchrotron X-ray techniques have had a significant impact on the development of material science. A great breakthrough in X-ray characterization of materials occurred when intense synchrotron X-ray sources became available in the mid-1970s. The combination of the high-pressure instruments with synchrotron radiation beam was pioneered by Buras et al in 1977.[110] They opened new directions in investigating the properties of materials under high pressure. By using brilliant synchrotron radiation, the high-pressure data are collected with markedly high speed, improved resolution, and low noise[111]. In the past few decades, many dedicated high-pressure beamlines have been built around the world. various synchrotron high-pressure techniques have been developed to investigate the crystal structure, electronic structure, and bonding information under pressure. For example, high-pressure synchrotron XRD experiments can identify the high-pressure phase; high-pressure inelastic X-ray scattering gives information on the arrangement of the atoms through the observation of the electron distributions at high pressure,[112] and high-pressure X-ray absorption spectroscopy allows a unique insight into the local structure and bonding information in many types of materials.[95]

2.3.3 X-ray absorption spectroscopy (XAS)

XAS is one of the most effective characterization techniques to study local atomic structure in condensed matter science. Depending on how the X-ray beams are absorbed near and above the core-shell binding energy levels, one can extract crucial information on the coordination number and geometry, oxidation state, and inter-atomic distances. Therefore, XAS measurements are used in numerous scientific fields including material science, chemistry, biology, and condensed matter physics.

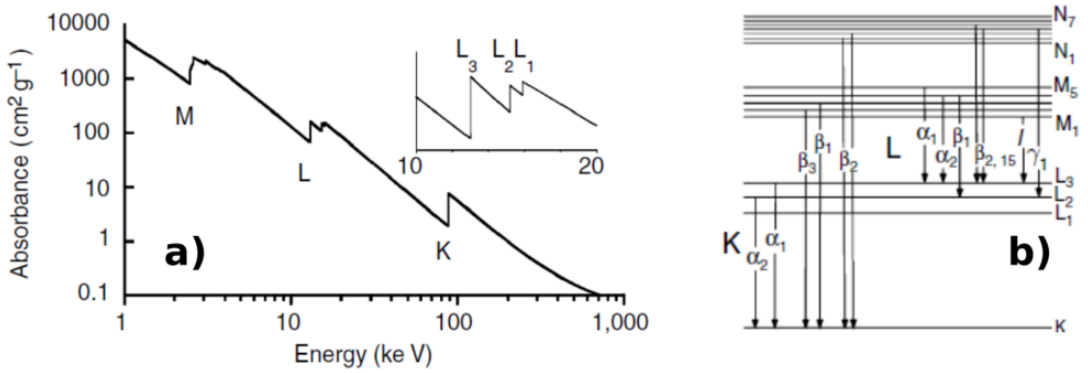

Figure 2.10 a) X-ray absorption spectrum of Pb element. Here K, L, and M radiations refer to different quantum numbers n being 1, 2, and 3, respectively. The inset shows L subshell radiations corresponding to 2s and 2p orbitals. b) X-ray emission lines of different shells.[113]

When a sample is subjected to incident X-ray beams with a range of energy, the cross-sectional absorbance decreases monotonously with increasing energy until an abrupt change at distinct energy for a certain element, what is called the absorption edge. The absorption edge can be defined as the discontinuity in the linear absorption coefficient that takes place when the incident beam reaches energy that can knock a core-shell electron out of its orbital. Each absorption edge is named depending on the binding energy of atomic subshells such as K, L, M, and N which correspond to different quantum states.

Traditionally, the XAS spectrum is divided into two regions, as shown in Figure

2.11. The structure in the vicinity of the edge is referred to as X-ray absorption near-edge structure (XANES). The oscillations above the edge, which can extend for several hundred eV or more, are referred to as extended X-ray absorption fine structures (EXAFS). The cut-off between the two regions is typically tens of electron volts above the absorption threshold. The distinction between XANES and EXAFS is ambiguous since the same fundamental physical principles govern the photoabsorption over the entire XAS region and there is no definite border that separates "near-edge" and "extended" structures. In some cases, week features that are referred to as pre-edge peaks may appear just below the edge energy.

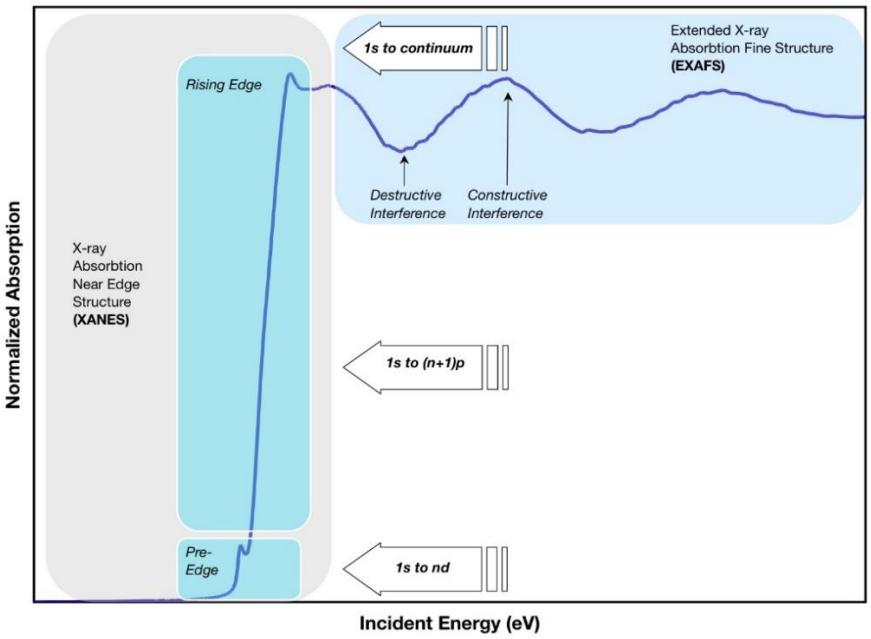

Figure 2.11 Two regions of XAS data.

The XANES part of the absorption spectra corresponds to an energy range of about~50 eV above the absorption edge where the scattered photo-electrons from the neighboring atoms have low kinetic energy. The absorption edge is generally taken as the maximum in the first derivative of energy or by convention the half-height of the peak. The unoccupied states are filled by the photo-electrons in this region, which gives rise to the change in the charge

density of the initial and the final states. This feature of XANES is used to distinguish the local coordination chemistry and the oxidation states of a selected absorber. Due to the complicated multiple scattering of the low kinetic energy photo-electrons interacting in the XANES region, there is no simplified equation for this part of the spectrum. Thus, the interpretation of XANES is generally qualitative in terms of coordination chemistry, band structure, and ionization states. Another important feature in the XANES region is the pre-edge interactions. These types of features are seen in most of the metals due to 1s to nd orbital transitions depending on dipole or quadripole selections.[114] Figure 2.12 shows different scattering processes triggered by an incident X-ray beam on a sample.

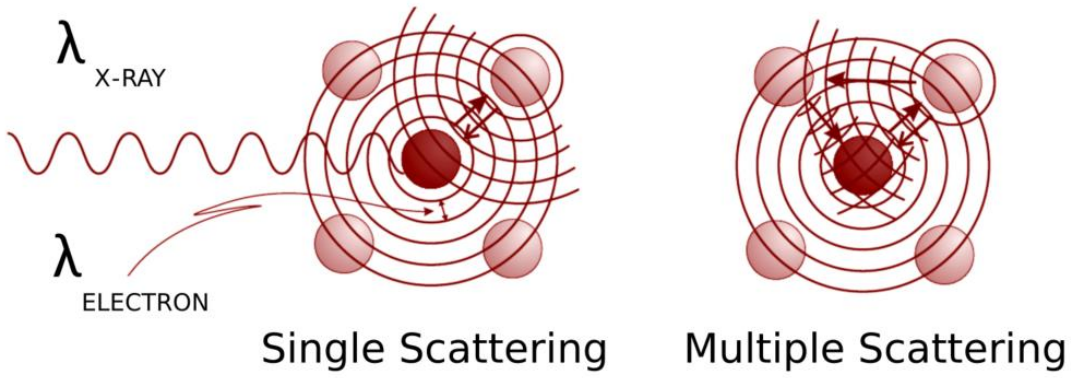

Figure 2.12 Schematic representation of single and multiple scattering of a photo-electron due to an incident X-ray beam.[115]

Unlike the XANES spectrum which is largely affected by the multiple scattering with the low kinetic energy of the photo-electron, the EXAFS part consists of the modulations of the absorption coefficient μ due to the interaction of the outgoing and the back-scattered waves of photo-electrons. The oscillations that can be seen in the marked EXAFS region in Figure 2.11 occur due to the constructive and destructive interference of such interactions. As the X-ray energy increases, the resulting photo-electron has greater kinetic energy and the EXAFS effects occur mostly due to the single scattering event

from an absorber to a scatterer and because of such effects, the absorption coefficient μ varies. In EXAFS, the signal measured in χ(k) is represented as:

$$\chi(\mathrm{k}) = \frac{\mu(E)-\mu_0(E)}{\Delta\mu_0(E)} \quad 2.9$$

where μ_0 is the absorption coefficient in the absence of the EXAFS modulations. The value of EXAFS signal χ(k) depends on many parameters as follows:[116-117]

$$\chi(\mathrm{k}) = \sum_s \frac{N_s A_s(\mathrm{k}) S_0^2}{kR_{as}^2} \exp(-2R_{as}/\lambda(\mathrm{k}))\exp(-2k^2\sigma_{as}^2)\cdot\sin(2kR_{as}+\phi_{as}(\mathrm{k})) \quad 2.10$$

Here N_s is the coordination number of scattering atoms around the absorber. Of special importance is that the EXAFS signal responds inversely to the distance between absorber and scatterer, denoted as R_{as}. λ(k) and as represent the energy dependence of the scattering and the mean free path of the photo-electron, respectively. The phase shift that depends on the scattering atom is given by ϕ_{as}. Finally, S_0^2 is the amplitude reduction parameter which has a value between 0 and 1 while σ_{as}^2 is the Debye-Waller factor which reflects the variance of the multiple absorber-scatterer distance differences. This value can also be interpreted as the mean square displacements of the scatterer atoms in some cases. Note that in EXAFS measurements, the extracted distances are averaged, therefore σ_{as}^2 holds an important meaning of the errors of the fitting and variations in the structure.

As mentioned above, a simplified quantitative analysis of the XANES spectrum is lacking due to its complicated nature. Fortunately, data analysis of the EXAFS spectrum is well established.[118-119] The EXAFS signal, χ(k), is obtained after removing the background modeled by polynomial splines and then normalizing the magnitude of the oscillations to the edge jump. Since the EXAFS oscillations occur due to the damping of $\sin(2kR_{as})$ term (see equation 2.10), the Fourier transform of these oscillating frequencies concerning the k vector results in the inter-atomic distances between the absorber and the

scatterer through various scattering paths. The EXAFS signal χ(k) is generally weighted with a power of k and the oscillations are truncated using a window function. The truncation range is determined by the noise level of the weighted EXAFS signal. Subsequently, a Fourier transformation is applied from reciprocal to real space and a radial distribution function (RDF) of the first neighbors is obtained. Figure 2.13 illustrates the schematic of the EXAFS data refinement procedure.

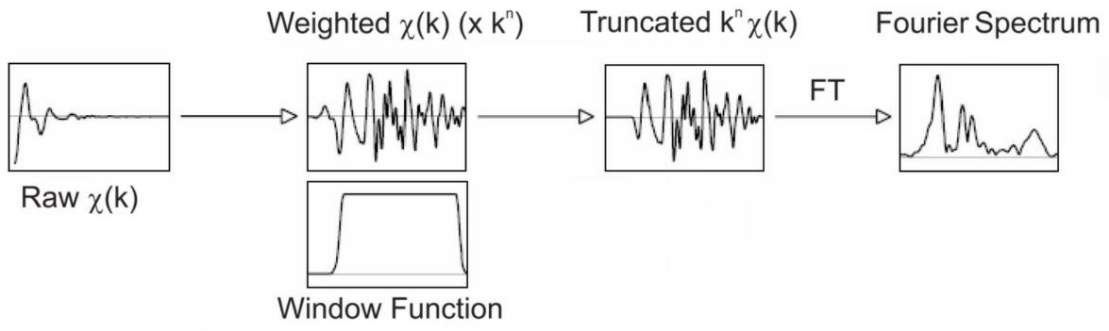

Figure 2.13 Schematic of the standard EXAFS data reduction.[115]

In this thesis, XAS data were analyzed using the ATHENA and ARTEMIS programs of the IFEFFIT package.[120-121]

2.3.4 XAS experiments with DAC

The coupling of this technique with DACs in the last four decades[122-125] opened a great possibility to provide unprecedented insights into the physical phenomena occurring at a wide range of pressure and temperature conditions.[126] However, full exploitation of the XAS together with DACs was limited until very recently due to several technical challenges. A major restricting problem for the applications of DACs for high-pressure XAS measurements was the presence of glitches in the energy range of interest due to the Bragg peaks of single-crystal diamond anvils. The number and energy position of the glitches are related to the x-ray energy and relative orientation between the DAC and x-ray beam, respectively. Below 10~12 keV, the relatively

less amount of DAC induced glitches could be removed in a wide XAS energy range by slowly rotating the DAC cell, so quantitative EXAFS analysis (with limited k range) was possible in some cases [124]. However, for higher photon energies a large number of glitches greatly reduce the useful energy range and restricted XAS applications to the XANES range, hindering the use of EXAFS. More recently, the successful synthesis of pure large-size nano-polycrystalline diamonds (NPD)[127] and its application as diamond anvils was found to be a satisfactory solution for this long-standing problem of diamond-induced glitches in the XAS data.[128-129] The Bragg glitches from the NPD anvils are continuous and broad, superimposing a uniform background on the EXAFS data. Figure 2.14 shows a comparison of Xe K-edge XAS data measured through NPD anvils and single-crystal diamond anvils.[126]

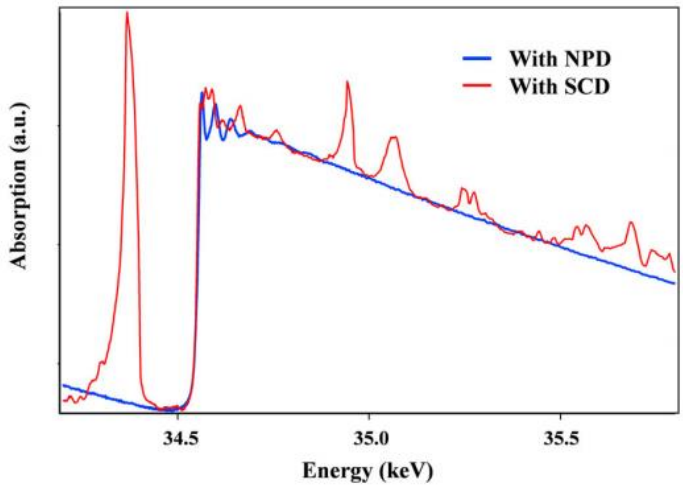

Figure 2.14 Comparison of the Xenon K-edge absorption spectra recorded at high pressure using single crystal diamond and NPD anvils.[129]

The typical diamond culets to reach 50~100 GPa P range are around 150~300 μm, and the sample chamber diameters range between 50~150 μm. As a result, the required focal spot dimensions of the X-ray beam should be 30~100 μm to perform high-pressure XAS experiments in the 100 GPa region. In addition, the position and intensity of the focal spot must remain stable on the sample

throughout the whole XAS acquisition process. In standard general-purpose scanning energy beamlines, however, focal spot sizes of the beam are usually quite larger (500 μm to 2 mm). On the other hand, the step-by-step energy scanning mode is not convenient for removing diamond glitches by DAC rotations. Therefore, conventional energy scanning modes have been regarded as poorly suited for high-pressure XAS measurements with DACs, and such measurements were initially coupled to the energy-dispersive XAS setup.

Using the dispersive geometry at synchrotron radiation facilities, a focused beam of adequate (30~70 μm at ODE, Soleil) spot size can be achieved and allow easy alignments of the DAC sample. Moreover, the whole energy range of the XAS data is collected by a position-sensitive detector (in 0.1~0.2 s of time) allowing a fast glitch removal process and keeping the intensity and position of the focal spot unchanged throughout the acquisition process so increasing the quality of data collections. Nowadays, with the recent upgrades of the x-ray focusing optics in some energy scanning EXAFS beamlines, and the use of NPD anvils, it is now possible to measure very high-quality EXAFS in Mbar pressure ranges.[130]

The co-axial transmission geometry (most common mode) of XAS experiments with DACs can be carried out for photon energies higher than 7 keV since the absorption of the thick diamond windows (3 to 4 mm for two anvils) increases considerably at low energy (flux decreases approximately to 10^{-4} at 7 keV). Luckily, with the recent progress of tailored anvil designs, it is now possible to use DACs for XAS measurements even at lower x-ray energies.[131] The XAS data discussed in this thesis have been collected at the ODE beamline of Synchrotron SOLEIL.[132] Details of the ODE experimental setup and its application for high-pressure XAS experiments will be introduced shortly in the following paragraph.

2.3.5Experimental setup for high-pressure XAS at ODE beamline

The energy dispersive geometry was developed in the 1980s for time-resolved EXAFS experiments to monitor dynamical processes.[133] The main idea is the use of a bent crystal to focus the polychromatic x-ray beam onto the sample and correlate the position of the measured outgoing beam to energy. This method allows the collection of XAS data in a large energy range using a solid-state position sensitive detector (with a typical ms time resolution) without any mechanical movement. Also, small beam dimensions (30∼70μm) on the sample can be obtained thanks to the focusing optics. These advantages were found to be very suitable for studying small samples, particularly the pressurized samples in the DACs, ensuring stable data acquisitions and convenient alignments of the DAC orientation (for removing glitches). Therefore, most of the pioneering XAS studies with DACs performed since the late 1980s were carried out at dispersive EXAFS beamlines. In particular, a series of high-pressure XAS studies on semiconductors and other materials[124, 134-135] was realized at the energy-dispersive D11 end station of the LURE-DCI synchrotron (Orsay, France).[136-137] The legacy of the activities related to that pioneering beamline was the starting point for designing the dispersive beamline (ODE[132]) at the new French synchrotron radiation facility (SOLEIL synchrotron, Paris-Saclay, 2006).

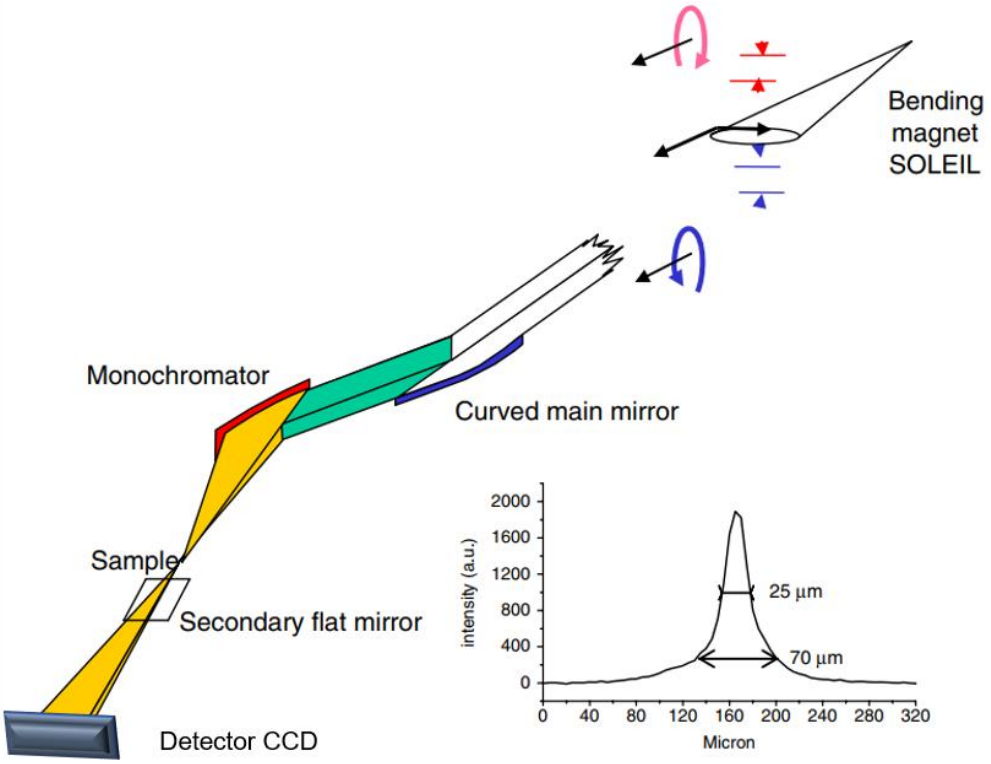

Figure 2.15 Scheme of the ODE beamline optical set-up.[132]

ODE (acronym of optic dispersive EXAFS) is a hard x-ray EXAFS station installed on a bending magnet of SOLEIL synchrotron, the preferred source for the high stability of the emitted beam.[132] The scheme of the beamline layout is shown in Figure 2.15. The incident whitebeam from the bending magnet is (higher) harmonically rejected and vertically focalized by a 1.2 m bent mirror. Subsequently, the beam is focalized by an elliptically curved crystal polychromator. The energy dispersed beam is sent through the sample at the focal point, after a complete harmonic suppression using a small secondary mirror, then diverges toward a position-sensitive detector (CCD coupled with a fluorescent screen). The pixel-energy relationship is approximately linear and can be directly calibrated using a polynomial function[138] and absorption standards, using different tools (developed by several authors including the ESRF-ID24 calibration tool and a python script available at SOLEIL).

The absorption coefficient (XAS spectrum) is obtained by taking the

logarithm ($-\frac{1}{t}\ln\frac{I}{I_0}$) of the incident ($I_0$) and transmitted (I) beam intensities. At ODE, either 111 or 311 oriented Si blades (30 cm long) are used according to the need of the designed experiment. The Si 111 blade provides higher photon flux and wider energy domains (500eV, typically) with a typical energy resolution of 1eV and is usually preferred for EXAFS measurements. The 311 blade provides a reduced photon flux and a narrower energy range (300eV, typically) with a better energy resolution of 0.5 eV, and is usually preferred for XANES measurements. Using these polychromators, the ODE beamline is currently able to provide a hard x-ray beam with photon energy ranging from 5 keV to 25 keV. Based on this experimental setup, we have obtained a lot of high-pressure XAS data. The details of the data analysis will be clarified in the next chapter.

Chapter 3

Pressure-induced structural phase transition and the optimization of photoelectric properties in $CsPbBr_3$

3.1 Introduction

In the process of exploring emerging photovoltaic technologies, dye-sensitized solar cells have attracted extensive attention for nearly 30 years since they appeared in 1991.[139] However, no substantial improvement in the efficiency of the prototype solar cell has been made until 2009 when the hybrid organic/inorganic perovskite (HOIP) was used as the photosensitizer of dye-sensitized solar cells. This new type of photoelectric material brought a new opportunity to improve the power conversion efficiency (PCE) of solar cells. 2012 is a milestone in the practical application of HOIP,[10] in which $CH_3NH_3PbI_3$ is used as the light-absorbing layer in all-solid-state solar cells. In the past ten years, the hybrid organic/inorganic perovskite has set off a "HOIP rush" due to its excellent properties such as large absorption coefficient, high carrier mobility, long carrier diffusion length, and surprisingly high tolerance to defects,[10, 14-16, 18-21, 140] and have been widely used in the fields of photovoltaics, photonics, and optoelectronics.[22-30] Great efforts have been made to improve the PCE from 3.8% to a record of 25.5% in just a few years.[9, 40] Despite the rapid improvement in

PCE, one basic issue, that is, the relatively fragile stability of HOIP-based solar cells has never been resolved. Pioneering studies revealed that ion-migration behavior in HOIP has important implications in terms of the long-term stability and performance of perovskite solar cell devices.[141-142] This phenomenon will hamper further efficiency boost and commercialization of perovskite solar cells. Hence, a detailed understanding of the ionic transport properties of lead halide perovskites is highly desirable.

In a large variety of perovskite materials, cesium lead bromide ($CsPbBr_3$) exhibits outstanding photoelectrical properties,[143-145] preferable thermal stability, and moisture-resistant merits[146-147] compared to organic-inorganic perovskite compounds, which make it an ideal candidate for future photovoltaic devices. $CsPbBr_3$ is acknowledged as an ionic conductor in which the mobile ions are Br^- and Cs^+ ions,[148-151] and the ionic transport properties can be tuned by temperature because of temperature-induced phase transition.[148, 152-153] In parallel with temperature, pressure is another way to alter the lattice and electronic configurations of materials. More recently, the pressure effects on the structure and optical properties of $CsPbBr_3$ have been studied.[34, 154-155] Nagaoka et al. reported that the initial phase of the superlattice $CsPbBr_3$ nanocube sample is a mixture of cubic and orthorhombic phases under ambient pressure. At 0.4 GPa, it changes to a pure orthorhombic phase, which remains at 5.1 GPa. The superlattice $CsPbBr_3$ nanocubes become amorphous at higher pressures. Nagaoka believes that there is a tetragonal phase in the amorphous process. Accompanied by the structural phase change, the photoluminescence (PL) intensity of the $CsPbBr_3$ single crystal nanosheets increased by six times at 0.1 GPa, The PL peak blue-shifted at 0.1 GPa then red-shifted with increased pressure and disappeared around 1.3 GPa. Compared with the initial superlattice $CsPbBr_3$ nanocubes, the PL intensity still maintains an increase of 1.6 times after decompression, indicating that the ensemble lifetime is

prolonged after the pressure treatment.[155] Zou et al. conducted high-pressure optical experiments on orthorhombic $CsPbBr_3$ nanocrystals and found that the isostructural phase transition occurred at 1.2 GPa, which is different from the results of Nagaoka et al. because of the different initial phases of the samples. In the PL measurement, no blue shift process was found due to the short phase transition interval of the $CsPbBr_3$ nanocubes with high surface energy. At the same time, they also found that the bandgap narrowed and the carrier lifetime prolonged. In the high-pressure experiment of the bulk $CsPbBr_3$, it was also found that the pure orthorhombic $CsPbBr_3$ undergoes an isostructural phase transition at 1.2 GPa. The initial bandgaps of bulk and nanomaterials are 2.32 eV and 2.52 eV, respectively. During the pressurization process, the bandgaps of bulk and nanomaterials decreased to 2.29 eV and 2.41 eV. The bandgap evolutions of bulk and nano-$CsPbBr_3$ under pressure are shown in Figures 3.1 and Figure 3.2.

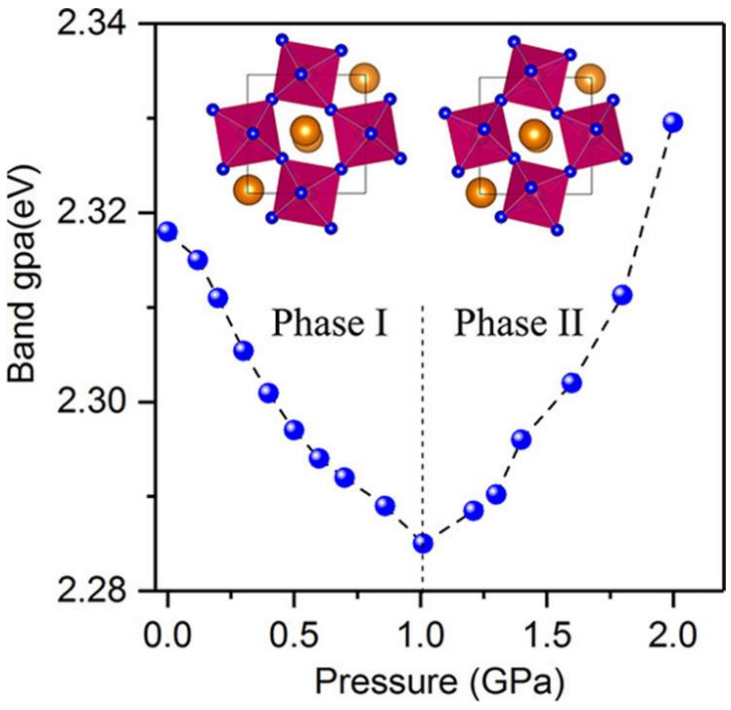

Figure 3.1 Bandgap evolutions of bulk $CsPbBr_3$ crystals as a function of pressure.[154]

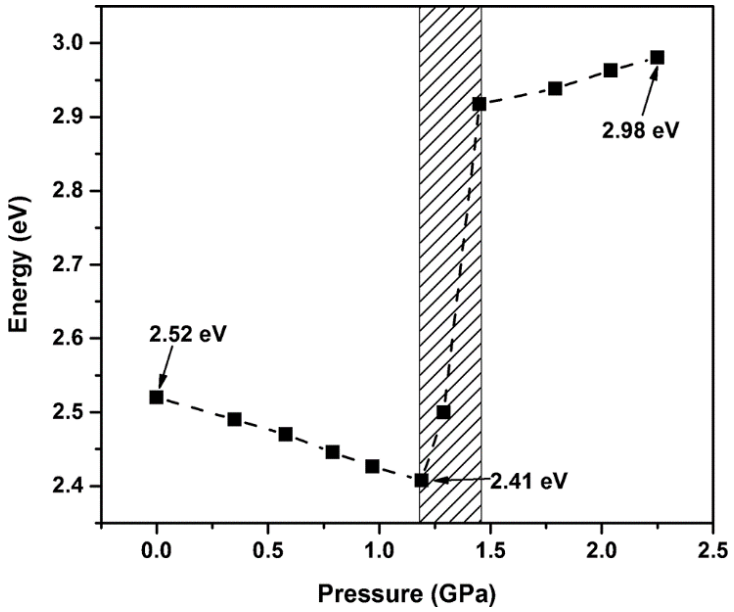

Figure 3.2 Bandgap evolutions of $CsPbBr_3$ nanocrystals as a function of pressure.[156]

However, no systematic experimental investigation of ionic transport properties for $CsPbBr_3$ under high pressures has been reported to date. Therefore, the ionic conduction processes in compressed $CsPbBr_3$ are still not clear. Furthermore, the excellent optoelectrical character is responsible for the high PCE of perovskite solar cells. In our previous work,[157-158] we know that the photoresponse capacity of both $MAPbI_3$ and $MAPbBr_3$ can be enhanced by moderate pressure (generally about 1 GPa) as shown in Figure 3.3. Whether pressure can enhance the photoresponse capacity of this kind of all-inorganic lead halide perovskites or not, maybe we can find some clues and enlightenment from photocurrent measurements on $CsPbBr_3$.

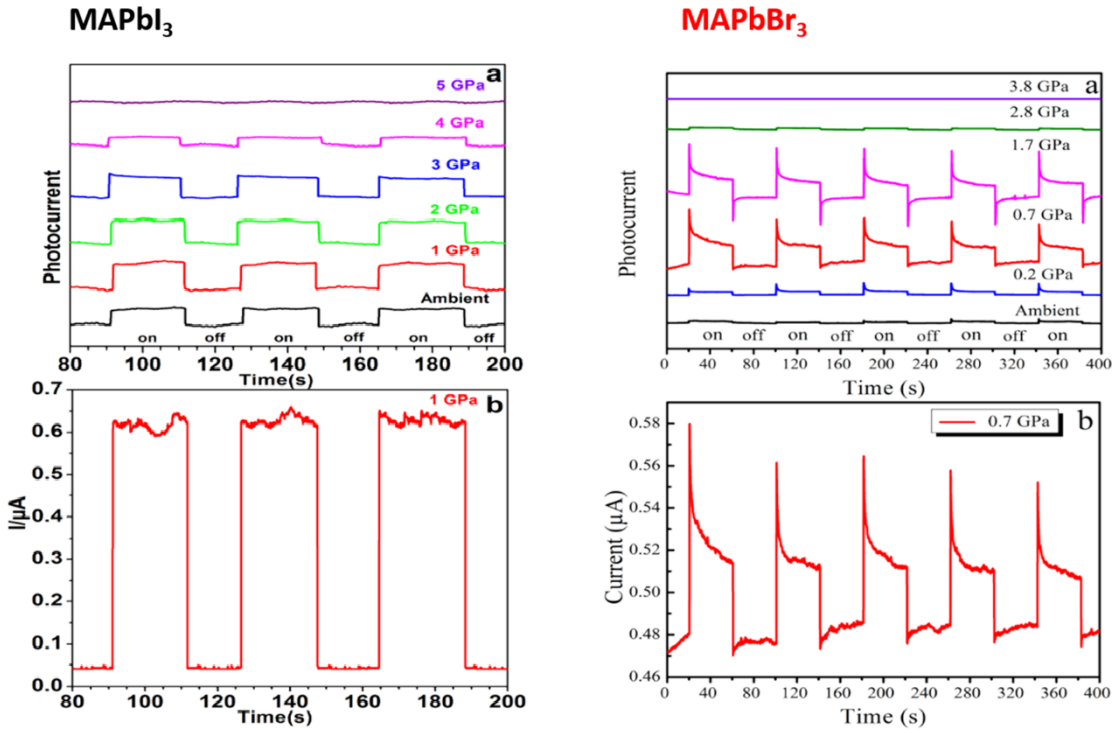

Figure 3.3 Left: (a) the pressure dependence of photocurrents in $MAPbI_3$, (b) the detailed response of photocurrent at 1.0 GPa; Right: (a) The pressure dependence of photocurrents in $MAPbBr_3$, (b) The detailed response of photocurrent at 0.7 GPa.

The nano-/micro-polycrystalline $CsPbBr_3$ film is usually used in solar cells, light-emitting diodes, and laser fields.[159-161] The abundant grain boundaries in $CsPbBr_3$ play an important role in the performance of photovoltaic devices. In traditional polycrystalline semiconductor absorbers such as $Cu_2ZnSnSe_4$,[162] Cu(In, Ga)Se_2,[163] and CdTe,[164] the grain boundaries often detrimentally affect the performance of solar cells. In contrast, the grain boundaries in lead halide perovskite materials are intrinsically benign[165] or beneficial for charge transport.[166] The grain boundaries have also been considered as nonradiative recombination centers, and their passivation leads to improved carrier separation.[166-169] However, how grain boundaries affect the electrical transport properties of $CsPbBr_3$ under compression is poorly understood.

To resolve the issues mentioned above, both the $CsPbBr_3$ powder samples containing many grain boundaries and the $CsPbBr_3$ single crystal whose grain

boundaries can be neglected are chosen as the research subjects. We have carried out in-situ high-pressure AC impedance spectroscopy measurements on them. Our goal is to explore how pressure modulates the ionic transport properties and the electrical parameters of $CsPbBr_3$ and how grain boundaries affect the electrical transport properties of $CsPbBr_3$ under compression. We have also performed photocurrent measurements to explore how pressure modulates the optoelectrical properties of $CsPbBr_3$. Finally, we analyzed the electrical transport property and the photoresponse of $CsPbBr_3$ at the microscopic level, which helps optimize the performance of $CsPbBr_3$-based photovoltaic devices.

3.2 Experimental details

$CsPbBr_3$ powder with a purity of > 99 % was bought from Xi'an Polymer Light Technology Corporation. The samples are air-sensitive and were stored in an Argon-filled glovebox. The quality of $CsPbBr_3$ was characterized by XRD and scanning electron microscopy (SEM) at ambient conditions. SEM was measured with an FEI MAGELLAN-400 microscope operating at 20 kV, Figures 3.4 and 3.5 show the SEM image and XRD pattern of $CsPbBr_3$ particles, respectively. Comparing all the diffraction peaks of the $CsPbBr_3$ sample with previous reports,[156, 170] we can confirm that the $CsPbBr_3$ powder sample has a pure orthorhombic phase structure and purity is high, which can satisfy our experimental requirements. The particle size of the powder sample is ~3 μm.

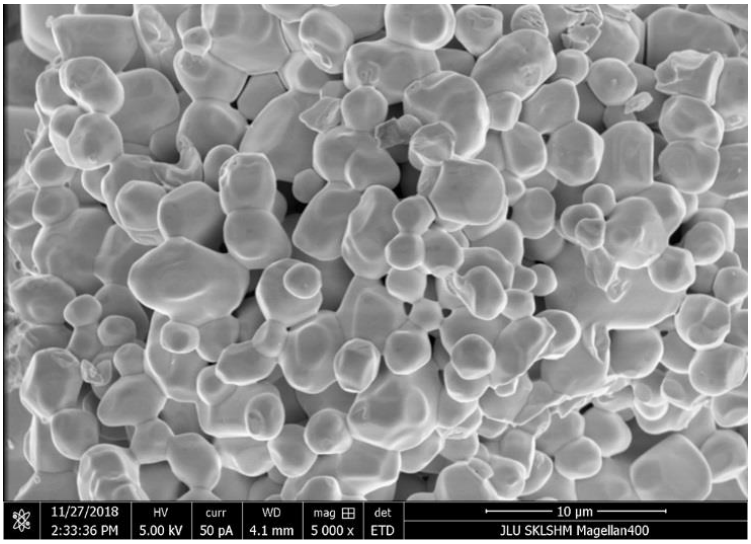

Figure 3.4 The SEM image of $CsPbBr_3$ powders.

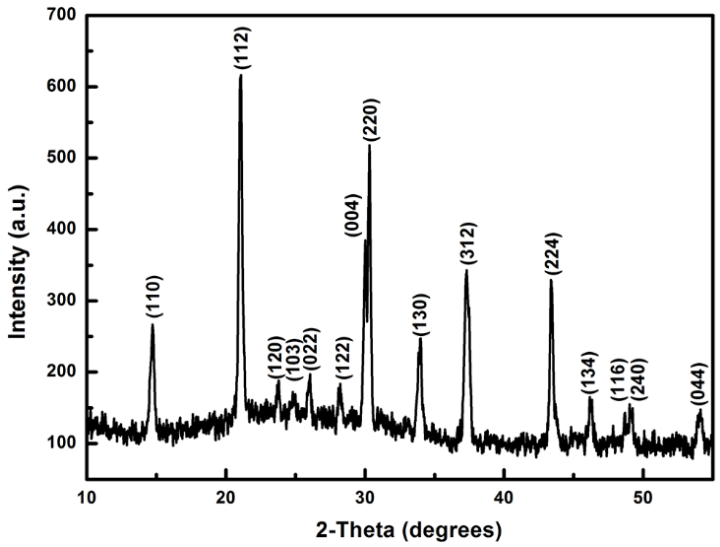

Figure 3.5 The XRD pattern of $CsPbBr_3$ powders.

In this experiment, a diamond anvil cell with a culet diameter of 400 μm was used to generate high pressure. High pressure in situ AC impedance spectroscopy and photocurrent measurements were measured by using symmetrical Mo electrodes, which were integrated on the surface of one of the diamond anvils. The specific integration process of Mo film electrodes can be found in previous studies.[171-172] One sheet of T301 stainless steel was pre-indented to a thickness of 70 μm, and a hole of 250 μm in diameter was drilled in the center of the indentation by laser. Then, a mixture of alumina power and

epoxy was compressed into the indentation. Subsequently, another hole of 130 μm was drilled and served as the sample chamber. The pressure was calibrated by the R1 fluorescence peak of the ruby ball with a diameter of about 5 μm.[173] In order to avoid the introduction of other interferences in AC impedance spectroscopy and photocurrent measurements, no pressure transmitting medium was used.

In the high pressure in situ AC impedance spectroscopy measurements of the $CsPbBr_3$ single crystal, NaCl is used as the pressure transmitting medium to get a quasi-hydrostatic condition since the $CsPbBr_3$ single crystal may not be able to completely fill the sample cavity. The single crystal chips with random planes for high pressure in situ AC impedance spectroscopy measurements are cut up from the big single crystal. The big single crystal is bought from Chemsoon Co., Ltd. as shown in Figure 3.6.

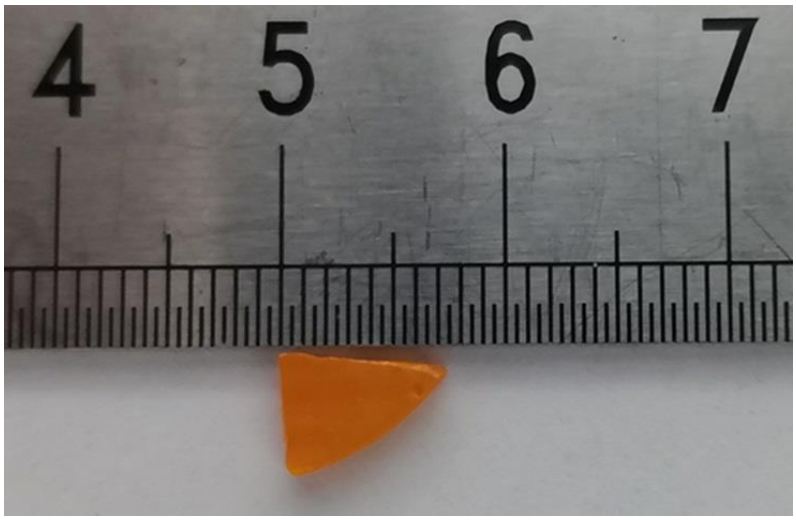

Figure 3.6 The photograph of the $CsPbBr_3$ single crystal.

The AC impedance spectroscopy was measured by a Solarton 1296 impedance analyzer equipped with Solarton 1260 dielectric interface. A 1 V sine signal was applied to the sample, and the test frequency ranged from 10^{-2} to 10^6 Hz. To shield the other signal interference and light-generated carriers, we placed the DAC in a metal box. The photocurrent was recorded by CHI660D

electrochemical workstation, the illumination was AM 1.5 simulated sunlight with the intensity of 2 $W \cdot cm^{-2}$ provided by 3A class solar simulator (UHE-16, ScienceTech Inc.), and then a constant DC voltage of 3 V was applied on the sample. The interval time Δt between light on and off was 40 seconds.

The high-pressure Br K-edge and Pb L3-edge XAS measurements at room temperature have been performed using the dispersive XAS setup (Figure 2.15) at the ODE beamline of Synchrotron SOLEIL.[132] Theoretical XAS spectra were calculated based on the first principle one electron full multiple scattering (FMS) theory using the CONTINUUM code embedded in MXAN.[174-176] To avoid diffraction from a single crystal diamond. Nanodiamond with a size of 400 μm, a steel gasket, and silicon oil as the pressure transmission medium were used in the measurement.

3.3 In-situ impedance spectroscopy study of $CsPbBr_3$ under pressure

The high pressure in situ AC impedance spectroscopy measurements was used to characterize the electrical transport properties of ionic conductor $CsPbBr_3$ powders. As presented in the Nyquist plot in Figure 3.7, clear changes in impedance with pressure are observed. From ambient pressure to 9.2 GPa, these spectra can be classified into three groups according to their shapes and variation trends as shown in Figures 3.7 (a)–(c), respectively. At pressures below 2.3 GPa, these spectra exhibit two distinct charge-transport regimes, and the semicircles closest to the origin are attributed to the process that ions or/ and electrons vibrate around the rigid lattice points back and forth at high frequencies. The semicircles' diameter equals the transfer resistance of the process which characterizes the difficulty in ion or/and electron transport in the lattice. The inclined straight lines at low frequencies are attributed to the impedance arising from the mass transfer of ionic diffusion. These

characteristics indicate that both ionic and electronic conductions dominate the transport process of $CsPbBr_3$ powders under 2.3 GPa as shown in Figures 3.7 (a) and (b). When the applied pressure exceeds 2.3 GPa, the inclined straight lines disappear, indicating that pure electronic conduction dominates the transport process of $CsPbBr_3$ powders as shown in Figure 3.7 (c).

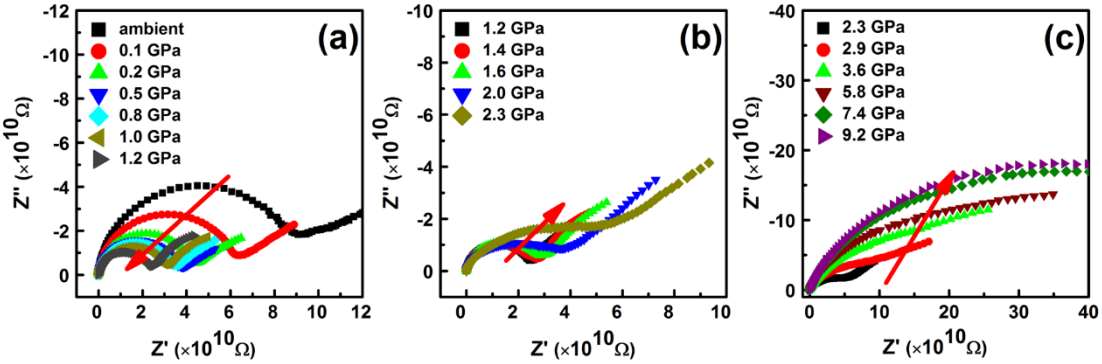

Figure 3.7 The Nyquist plots of $CsPbBr_3$ powders measured at pressures up to 9.2 GPa. (a) 0–1.2 GPa; (b) 1.2–2.3 GPa; and (c) 2.3–9.2 GPa.

The selection of simulation equivalent circuit models plays a key role in the analysis of pressure-dependent electrical transport mechanisms of $CsPbBr_3$. According to the different ac impedance spectral shape and variation trend in $CsPbBr_3$ powders shown in Figure 3.7, we use three kinds of suitable equivalent circuit models to fit the impedance spectra as shown in Figure 3.8.

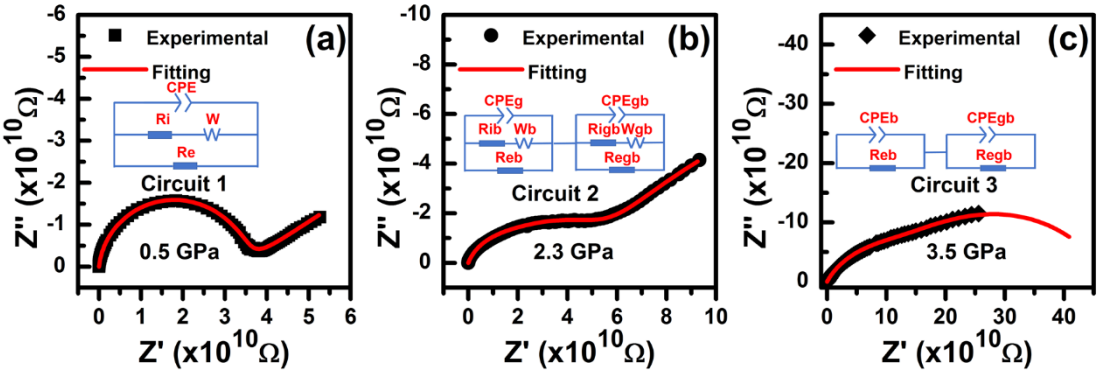

Figure 3.8. The experimental and fitting data for $CsPbBr_3$ powder impedance spectra at different pressures. (a) 0.5 GPa; (b) 2.3 GPa; and (c) 3.5 GPa.

The impedance spectrum of $CsPbBr_3$ powders at 0.5 GPa is selected as an example to demonstrate the process of deducing the electrical parameters of ion and electron migration with the equivalent circuit (Circuit 1) in Figure 3.8 (a). In Circuit 1, R_i and R_e which present a parallel relationship denote ionic and electronic resistances, respectively. W is the Warburg impedance of ion diffusion, and CPE (Q) is the constant phase element. The impedance of $CsPbBr_3$ can be expressed as:

$$Z = \frac{1}{\frac{1}{R_e}+\frac{1}{R_i+Z_W}+\frac{1}{Z_Q}} \quad 3.1$$

where Z_W and Z_Q are the impedances of Warburg and CPE equivalent elements, respectively.

At pressures below 2.3 GPa, the semicircles of impedance spectra are highly symmetrical; it is meaningless for us to distinguish the contributions of bulk and grain boundaries to the total electrical resistance because big bulk/grain boundary resistance errors will appear in the simulation process. At 2.3 GPa, $CsPbBr_3$ begins to be amorphous[154] and generates more grain boundaries, the semicircle turns into two arcs which represent the bulk resistance and the grain boundary resistance, respectively, and their values are simulated by the equivalent circuit (Circuit 2) as shown in Figure 3.8 (b). In Circuit 2, R_{ib} and R_{igb} represent the ionic resistance, while R_{eb} and R_{egb} represent the electronic resistance in bulk and grain boundaries, respectively. At this time, the impedance of $CsPbBr_3$ can be expressed as:

$$Z = \frac{1}{\frac{1}{R_{eb}}+\frac{1}{R_{ib}+Z_{Wb}}+\frac{1}{Z_{Qb}}} + \frac{1}{\frac{1}{R_{egb}}+\frac{1}{R_{igb}+Z_{Wgb}}+\frac{1}{Z_{Qgb}}} \quad 3.2$$

With the applied pressure exceeding 2.3 GPa, the Warburg impedance disappears and the electronic conduction is the only detectable process, and so, we employ another equivalent circuit (Circuit 3) in Figure 3.8 (c). In the Figure, the impedance spectrum of $CsPbBr_3$ powders at 3.5 GPa is selected as an

example to demonstrate the process of electron migration in bulk and grain boundaries. In Circuit 3, R_{eb} and R_{egb} represent the electronic resistances in bulk and grain boundaries, respectively. The impedance of $CsPbBr_3$ of the Circuit 3 can be expressed as:

$$Z = \frac{1}{\frac{1}{R_{eb}}+\frac{1}{Z_{Qb}}} + \frac{1}{\frac{1}{R_{egb}}+\frac{1}{Z_{Qgb}}} \quad 3.3$$

The specific parameters of electrical transport in the $CsPbBr_3$ powder samples were obtained by fitting the impedance spectra with three equivalent circuits. The detailed fitting parameters are provided in Table I.

TABLE I. Detailed fitting parameters.

Circuit 1	**CPE_1-T**	**CPE_1-P**	**R_i**	**W_1-R**	**W_1-R**	**W_1-R**	**R_e**
	3.40×10^{-13}	0.933	3.452×10^{10}	4.06×10^{12}	1.51×10^{7}	0.377	3.2×10^{12}
Circuit 2	**CPE_b-T**	**CPE_b-P**	**R_{ib}**	**W_b-R**	**W_b-R**	**W_b-R**	**R_{eb}**
	2.60×10^{-12}	0.78	4.0×10^{10}	4.67×10^{10}	5	0.4	2.6×10^{10}
	CPE_{gb}-T	**CPE_{gb}-P**	**R_{igb}**	**W_{gb}-R**	**W_{gb}-R**	**W_{gb}-R**	**R_{egb}**
	7.20×10^{-12}	0.72	3.790×10^{10}	3.66×10^{10}	4.8	0.32	2.8×10^{11}
Circuit 3	**CPE_b-T**	**CPE_b-P**	**R_{eb}**	**CPE_{gb}-T**	**CPE_{gb}-P**	**R_{egb}**	
	1.58×10^{-12}	0.6796	1.292×10^{11}	6.47×10^{-12}	0.6855	3.48×10^{11}	

By fitting the impedance spectra with Circuit 1, we obtained the pressure dependence of R_i, R_e, and R_{total} [$R_{total} = R_iR_e/(R_i + R_e)$] from ambient pressure to 2.3 GPa. With Circuit 3, we obtained the pressure dependence of R_b, R_{gb}, and R_{total} ($R_{total} = R_b + R_{gb}$) from 2.9 to 9.2 GPa. The pressure-dependence of electrical parameters including R_i, R_e, R_b, R_{gb}, and R_{total} is shown in Figure 3.9 (a). It can be seen that the electrical parameters including R_i, R_e, and R_{total} show discontinuous changes at 1.2 GPa, which can be attributed to the pressure-induced structural phase transition from the orthorhombic (P*bnm*) phase (Phase I) to the orthorhombic (P*bnm*) phase (Phase II).[154] From ambient pressure to 2.3 GPa, R_i

is always about 1 or 2 orders smaller than R_e, indicating that ionic conduction dominates the transport process. The total resistance is therefore nearly equal to the ionic resistance.

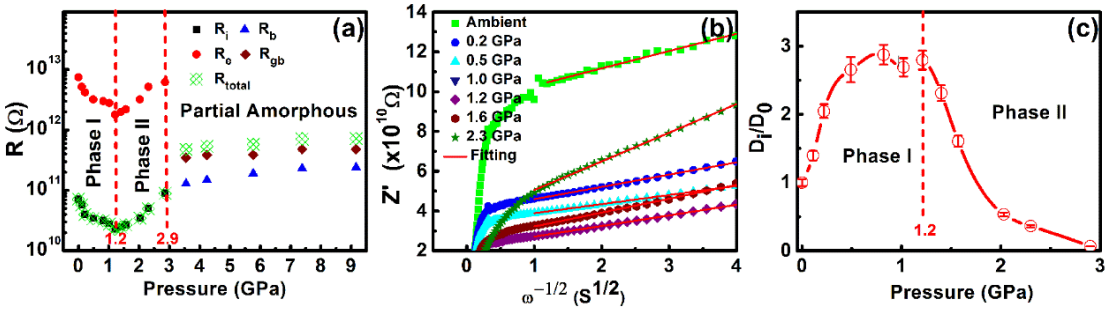

Figure 3.9 (a) Pressure dependence of R_i, R_e, R_b, R_{gb}, and R_{total}. (b) Z′ as a function of $\omega^{-1/2}$ plots at low frequencies from ambient pressure to 2.3 GPa. (c) Pressure dependence of the relative ionic diffusion coefficient from ambient pressure to 2.3 GPa.

To discuss the internal mechanism of electrical parameter changes in $CsPbBr_3$, we take $MAPbI_3$, which has been deeply studied as an example to illustrate the ion migration and migration channels in HOIPs. Theoretically, all ions in $MAPbI_3$, such as I^-, $Pb^{2+,}$ and MA^+, may participate in migration. Other ions like H^+ involved in migration may come from the decomposition or contamination of materials.[177] Eames et al. compared the activation energies of I^-, Pb^{2+} and MA^+ ions in $MAPbI_3$ by theoretical calculations and believed that I^- is the most likely ion to migrate due to its lowest activation energy.[151] The schematic diagram of the ion movement path is shown in Figure 3.10. In their model, I^- ions move along a slightly curved path on the edge of the PbI_6 octahedron I^-—I^- (as shown in Figure 3.10 b, path A), with the smallest activation energy E_A of 0.58 eV. The MA^+ ions on the (100) plane are transported along the <100> direction (as shown in Figure 3.10 b path D), and the activation energy E_A is 0.84eV. The Pb^{2+} ion moves along the diagonal of the unit cell in the direction of <100> (as shown in Figure 3.10 b path B), and its activation energy E_A is 2.31eV.

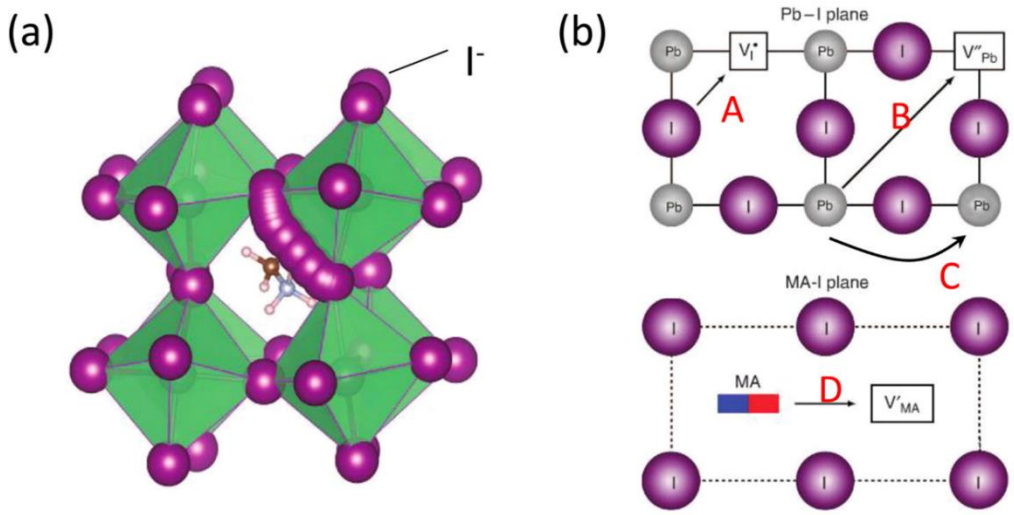

Figure 3.10 The schematic diagram of the ion movement paths in $MAPbI_3$.

Eames et al. obtained the activation energy E_A of 0.60-0.68 eV for I^- in the photocurrent relaxation experiment, which is close to the theoretical value of 0.58 eV.[151] Therefore, they believe that I^- is the key migration ion in $MAPbI_3$with a diffusion coefficient of 10-12 cm^2s^{-1} at 320 K. In addition, Azpiroz et al. believed that I^- ions can migrate through the $MAPbI_3$ film within 1 μs based on their calculated activation energies of I^-, Pb^{2+} and MA^+, which are 0.08 eV, 0.80 eV, and 0.46 eV, respectively,[178] where the activation energy E_A of I^- ions is very small. This time constant of 1 μs can't explain the hysteresis effect with a time scale of 0.1—100s in the $MAPbI_3$ device. Therefore, Azpiroz believes that most of the ions mainly involved in migration in $MAPbI_3$ are MA^+ and Pb^{2+} ions. Subsequently, Haruyama et al. obtained the activation energies (E_A) of 0.33 eV and 0.55 eV for I^- and MA^+ migrations, respectively.[179] Although the calculated activation energies depend slightly on the theoretical methods, they agree that I^- is easier to migrate than MA^+ and Pb^{2+}. It is worth noting that none of these models consider ion migration through interstitial sites (Frenkel defects). According to theoretical calculations, the Frenkel defect formation energies of $I^-$and MA^+ are 0.23-0.83 eV and 0.20-0.93 eV, respectively, which are comparable to the activation energies of I^- and MA^+,[180] thus can't be neglected to understand the ion migration phenomenon in HOIPs. The H^+ ion has the

smallest radius, Egger et al. calculated the activation energy E_A to be 0.29eV, which is considered to be the only ion that migrates through the Frenkel defect. $CsPbBr_3$ and $MAPbI_3$ have a similar perovskite structure. Therefore, in the following discussion, we believe that the ion migration paths in $CsPbBr_3$ are the same, that is, the migration of cations and halide ions. The research results of Chen et al.[181] and Zhang et al.[182] also confirmed the migration of Br ions and Cs ions in $CsPbBr_3$ through theory and experiments.

From Figure 3.9 (a), we observe that R_i decreases in Phase I and increases in Phase II with increasing pressure. We used the well-known relative ionic diffusion coefficients[183] to characterize the pressure-dependent ionic resistance variation trend in $CsPbBr_3$ powders. To obtain the relative ionic diffusion coefficient, we plot Z' as a function of $\omega^{-1/2}$ [Figure 3.9 (b)], which shows a linear behavior in the low-frequency regime, and the slope is the Warburg coefficient. Based on the Warburg coefficients obtained from Figure 3.9 (b), we get the pressure-dependent relative ionic diffusion coefficients[184] which are shown in Figure 3.9 (c). In Phase I of $CsPbBr_3$, the relative ionic diffusion coefficients increase with pressure, which indicates that pressure enables ions to migrate more easily in the crystal lattice by decreasing the ionic resistance. This phenomenon can be attributed to the pressure-induced reduction of crystal lattice parameter,[154] corresponding to a continuous decrease in the ions' hopping distance as pressure increases.[158] In Phase II of $CsPbBr_3$, the relative ionic diffusion coefficients decrease with pressure which leads to the increase of the ionic resistance. This phenomenon can be explained by the serious distortion of the Pb-Br bond length and $PbBr_6$ octahedra, which result in the gradual closure of hopping channels.[154, 158]

As seen in Figure 3.9 (a), the electronic resistance (R_e) decreases between 0 and 1.2 GPa then increases between 1.2 and 2.3 GPa. This is associated with the pressure-induced bandgap narrowing in Phase I and broadening in Phase II of

$CsPbBr_3$.[156] After 2.3 GPa, the ionic conduction disappears and the electronic conduction dominates the electrical transport process. Bulk and grain boundary resistances are distinguished by the simulation process. We can see that R_b is always larger than R_{gb}, indicating that the grain boundary shows a larger contribution than bulk to the total resistance of $CsPbBr_3$ powders. R_b, R_{gb}, and R_{total} increase with pressure from 2.9 GPa to 9.2 GPa, which is attributed to the structural disorder and amorphization[154] in $CsPbBr_3$ powders.

As the electrical transport properties are critically dependent on grain boundary effects, at this stage, we do not know whether the pressure-induced ionic-electronic to pure electronic conduction transition occurring at 2.3 GPa was affected by the grain boundaries or not. In order to eliminate the grain boundary effects and clarify the reason, we have conducted the AC impedance spectroscopy measurements on the $CsPbBr_3$ single crystal whose grain boundary effects can be ruled out. In the high pressure *in situ* AC impedance spectroscopy measurements of $CsPbBr_3$ single crystal, two pieces of platinum foils are used as the electrodes. The micrographs of $CsPbBr_3$ single crystal at different pressures in a DAC for AC impedance spectroscopy measurements are shown in Figure 3.11.

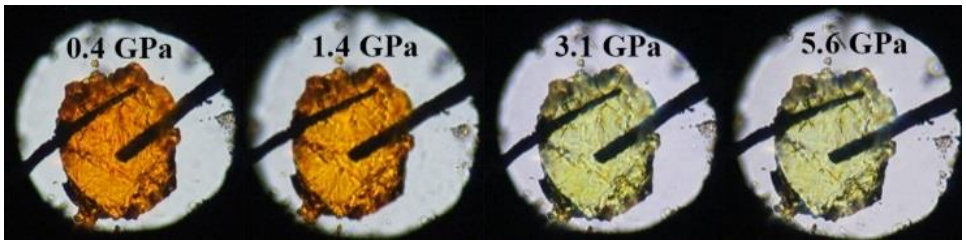

Figure 3.11 The micrographs of $CsPbBr_3$ single crystal at different pressures for AC impedance spectroscopy measurements.

The sample chamber is about 200 μm and the $CsPbBr_3$ single crystal chips in the sample chamber are about 120 × 100 × 40 μm^3. During the pressurization process, the $CsPbBr_3$ single crystal remained intact, and the electrode position did not change, but the color of the $CsPbBr_3$ single crystal changed due to the

change in the light absorption of the sample with pressure.[154]

The Nyquist plots from the AC impedance spectra of the $CsPbBr_3$ single crystal from ambient pressure to 6.8 GPa are shown in Figure 3.12 which can also be classified into three groups according to their shape and variation trends. At pressures below 2.3 GPa, mixed ionic and electronic conduction in $CsPbBr_3$ single crystal is observed as shown in Figure 3.12 (a) and (b). When the applied pressure exceeds 2.3 GPa, only pure electronic conduction in $CsPbBr_3$ single crystals is observed as shown in Figure 3.12 (c). By comparing the pressure-dependent AC impedance spectra of $CsPbBr_3$ powders (Figure 3.9) with $CsPbBr_3$ single crystal, we observed that both samples exhibit similar electrical transport properties under compression including: (i) the pressure-dependent electrical impedance value variation trends and (ii) 2.3 GPa is the turning point of ionic-electronic to pure electronic conduction transition. The only difference in the two samples is the pressure-dependent electrical impedance values which can be attributed to the grain boundary effects. Thus, we can conclude that the pressure-induced ionic-electronic to pure electronic conduction transition which occurs at about 2.3 GPa is intrinsic in $CsPbBr_3$.

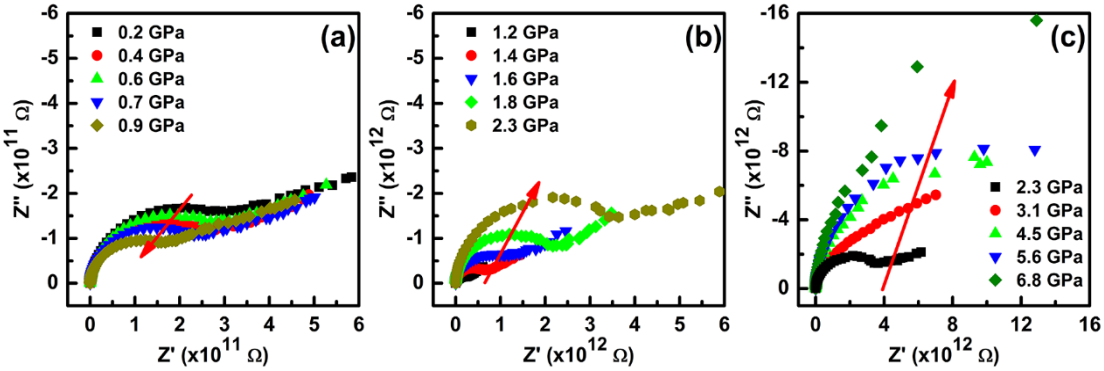

Figure 3.12 The Nyquist plots from AC impedance spectroscopy of $CsPbBr_3$ single crystal measured at (a) 0.2-0.9 GPa; (b) 1.2-2.3 GPa; (c) 2.3-6.8 GPa.

3.4 In situ photocurrent study of $CsPbBr_3$ under pressure

Considering that the photocurrent parameter reflects the light-harvesting ability of photovoltaic materials, we also measured the pressure-dependent photocurrent of $CsPbBr_3$ up to 2.9 GPa as shown in Figure 3.13.

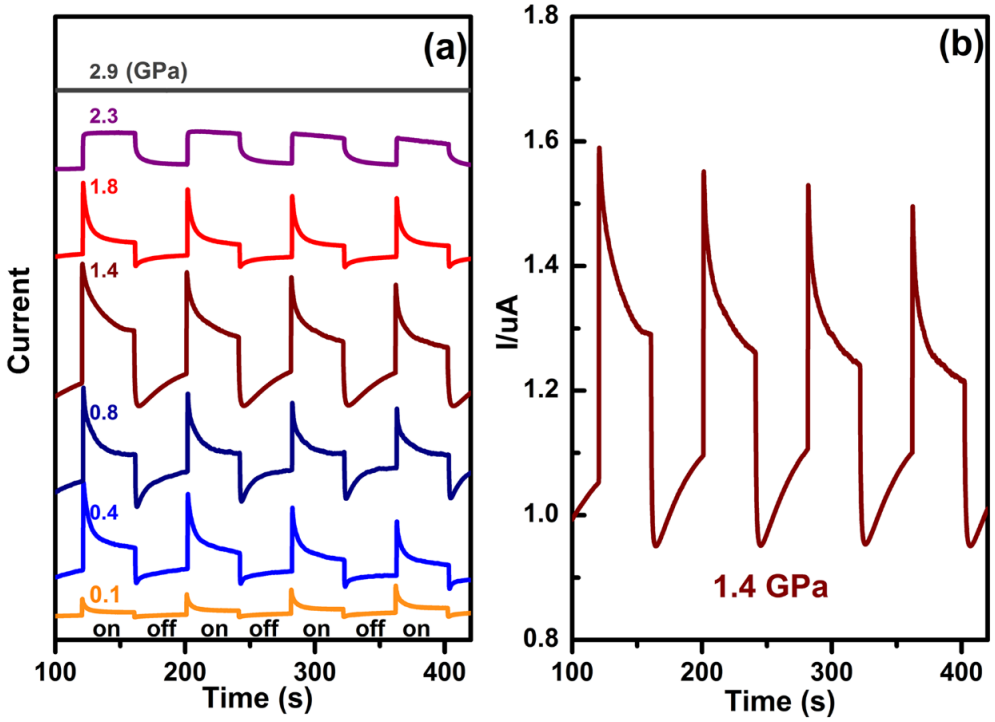

Figure 3.13 (a) The pressure-dependent photoresponse of $CsPbBr_3$. (b) detailed photo-response of $CsPbBr_3$ at 1.4 GPa.

The total current is the sum of dark current and photocurrent. As shown in Figure 3.13(a), the photocurrents of $CsPbBr_3$ under pressure are significantly higher than the value measured under ambient conditions. Specifically, at 1.4 GPa, $CsPbBr_3$ exhibits the strongest photoresponse [Figure 3.13 (b)], suggesting that pressure can improve the photovoltaic properties of $CsPbBr_3$. Noticeably, an extremely sharp and needle-like peak emerges at every moment of light irradiation and then transforms into a gradual decrease in photocurrent until the light is off, which can be attributed to the mixed conduction within $CsPbBr_3$. The phenomenon can be explained as follows: All the ions appearing in the sample can be divided into two parts: preexisting ions (in dark) and photo-

excited ions[185] (under illumination). The pre-existing ions migrate to the contacts along the external electric field to create a double layer under dark and illumination conditions. They will be blocked at the perovskite-electrode interface, and finally, a dynamic equilibrium built-in electric field is formed. When the light is on, a lot of photon-generated electrons/holes and photo-excited ions appear instantaneously, leading to a sharp increase in photocurrents. Electrons can pass through the perovskite electrode interface freely, while the photo-excited ions migrate to the contacts along the external electric field and accumulate at the electrodes with time to form a new built-in electric field, resulting in a gradual decrease in photocurrents. When the light is off, the photo-generated electrons can be quenched on the spot immediately, which causes a sudden decrease in photocurrent. But photo-excited ions cannot be quenched in time locally. Most of them have to drift a long distance to empty interstitial sites for quenching. So, it will take a relatively long time for the accumulated photo-excited ions to disperse away from the perovskite-electrode interface, correspondingly causing a sequence of associated results, including the continuous decrease in the built-in electric field, the increase in the net electric field, and the moderate increase in dark currents. Both photo-generated carrier recombination and lattice distortion are also possible reasons for explaining the experimental data which have been discussed in previous work.[158, 186-187] At the pressure of 2.3 GPa, the extremely sharp and needle-like peak disappears which is associated with the disappearance of ionic conduction in $CsPbBr_3$. As the pressure exceeds 2.9 GPa, the photocurrents of $CsPbBr_3$ could hardly be detected, which is believed to be from the amorphization of the samples.

3.5 In situ XAS study of $CsPbBr_3$ under pressure

As mentioned above, we already know that pressure-induced phase transition

and bandgap evolution affect the photoelectric properties of $CsPbBr_3$. To obtain a deep understanding of the electronic and geometric structures and the bandgap evolution of $CsPbBr_3$ under pressure, pressure-dependent X-ray absorption spectroscopy (XAS) at the Br K-edge and the Pb L3-edge were collected as shown in Figure 3.14.

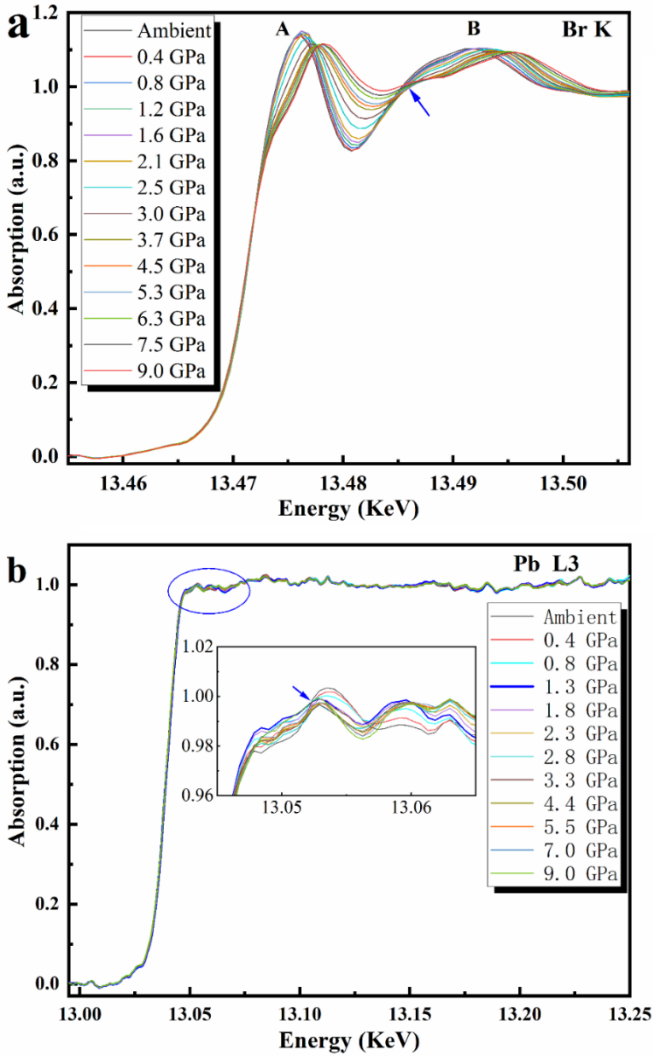

Figure 3.14 Experimental XAS spectra of $CsPbBr_3$ at Br-K (a) and Pb-L3 (b) edges. The inset zooms on the near-edge region of Pb.

The features at the Br-K absorption edge are attributed to the transition from 1s to the hole density in the 4p (pre-edge) and 5p (near-edge) orbitals in the Br^- ion. The features appearing at the Pb-L3 absorption edge can be assigned to the dipole-allowed transition from 2p to empty nd states (n> 5) in Pb^{2+} ions.

Because the 5d orbitals of Pb are filled, the white line signal is weak, pressure-induced changes of XAS signals are not as obvious as those at Br K-edge.

Due to diamond diffractions, glitches appear in the extended X-ray absorption fine structure (EXAFS) spectra, which makes it difficult for fine structural analysis. The data analysis at Br K-edge has focused on X-ray absorption near-edge spectroscopy (XANES). At Pb L3 edge, diamond diffractions are not obvious some glitches can be moved away by rotating the diamond anvil cell, we tried to obtain EXAFS data. There is no obvious edge shift at Br K-edge and Pb L3 edge up to 9 GPa (see Figure 3.14), indicating that the oxidation state of Br and Pb remains constant with pressure. The presence of an isosbestic point (see the blue arrow in Figure 3.14) illustrates the coexistence of two phases and the gradual structural change of $CsPbBr_3$ with pressure.[188-190]

$CsPbBr_3$ is an orthorhombic structure with space group Pbnm under ambient pressure.[191] A Pbnm to Pbnm isostructure phase transition at 1.2 GPa has been proposed by the recent XRD experiment.[170] In fact, the isostructural phase was difficult to identify, similar atomic positions and slightly different lattice constants were used for the structural refinements. In order to understand the possible spectral changes associated with such a subtle structural transition, we have simulated XANES spectra for both Pbnm (0 GPa) and Pbnm (1.2 GPa) structures using the same atomic positions and slightly different lattice constant (see Tables 1 and 2).

Table 1: Crystal structure parameters of Pbnm phase at P = 0 GPa.[191]

Atom	X	Y	Z	Site
Cs1	0.99	0.971	0.25	4c
Br1	0.046	0.505	0.25	4c
Br2	0.793	0.205	0.025	8d
Pb1	0.5	0.0	0	4b
a = 8.207 Å b = 8.255 Å c = 11.759 Å $\alpha = \beta = \gamma = 90^{o}$				

Table 2: Crystal structure parameters of Pbnm phase at P = 1.2 GPa.[170]

Atom	X	Y	Z	Site
Cs1	0.98625	0.98664	0.25	4c
Br1	0.04042	0.55129	0.25	4c
Br2	0.80345	0.19722	0.03027	8d
Pb1	0.5	0.0	0	4b
a = 7.9506 Å b = 8.1652 Å c = 11.5781 Å $\alpha = \beta = \gamma = 90^{o}$				

The 3D visualization of the Pbnm-0 GPa and Pbnm-1.2 GPa structures were plotted in Figure 3.15.

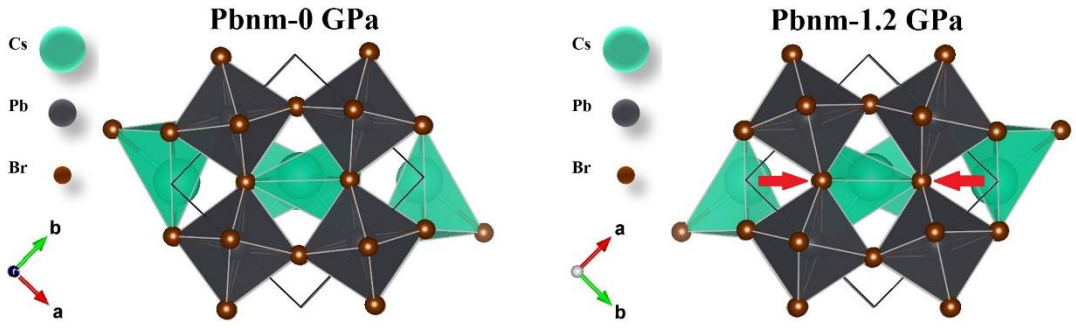

Figure 3.15 Pbnm-0 GPa and Pbnm-1.2 GPa structures of $CsPbBr_3$. Pressure-induced lattice compression can be seen in the place marked by the red arrows, the width is narrower at 1.2 GPa than at 0 GPa.

As shown in Figure 3.16, the theoretical calculation results of XANES are consistent well with the experimental XAS signals. Thus it is reasonable to

assume that the present XANES experiment identifies the possible Pbnm phase at 1.2 GPa.

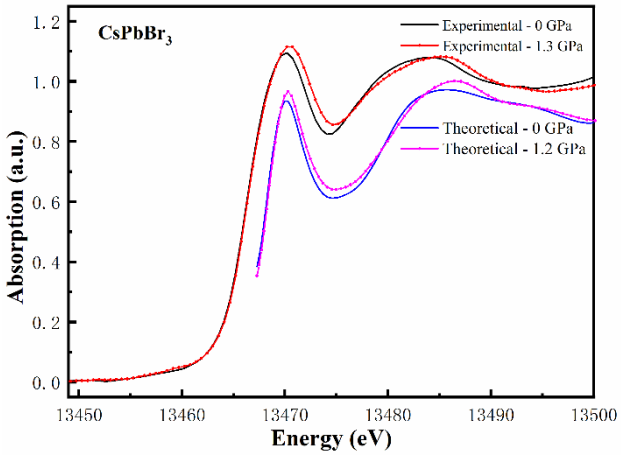

Figure 3.16 XANES simulations for Pbnm-0 GPa and Pbnm-1.2 GPa structures.

The XANES region contains fruitful electronic structural information and can be used as a fingerprint to obtain the electronic structural changes with pressure. To see the changes of the position and the shape of the main features as a function of pressure clear, the spectra are separated vertically as shown in Figure 3.17. With the increase of pressure, the white line peak (labeled A) becomes broader and shifts to higher energy by 1.95 eV, the second peak (labeled B) also shifts to higher energy by 3.88 eV, these are direct evidence of the shortening of the distances between Br and its surrounding neighbors,[192, 193] which is Br-Pb bond according to the structure of $CsPbBr_3$.

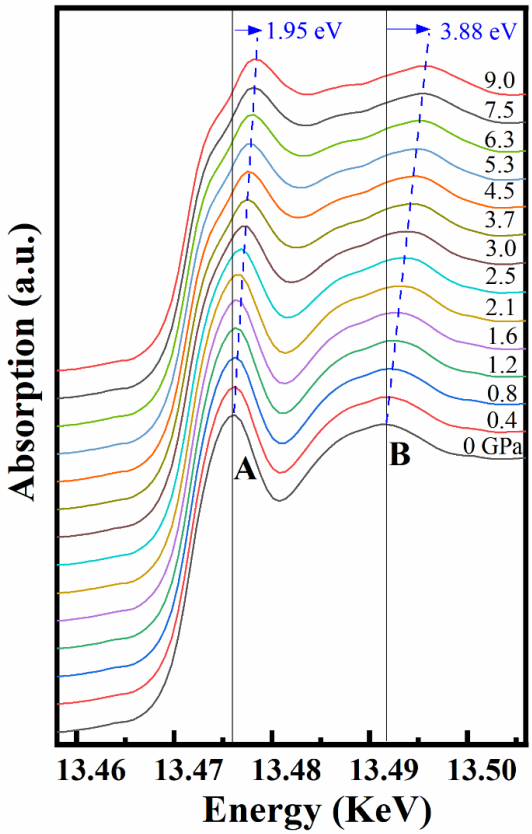

Figure 3.17 The vertically shifted absorption spectra of Br K-edge under pressure.

The white line intensities shown in Figure 3.15 illustrate the changes of the unoccupied electron density state of the 5p orbital in Br, which will have a sharp change when phase transition happens. We integrated the white line area and its changes with pressure are shown in Figure 3.18. We believe that the change at 1.2 GPa is caused by the phase transition of $CsPbBr_3$, and the inflection point at 3.7 GPa is where $CsPbBr_3$ starts to become amorphous.[170]

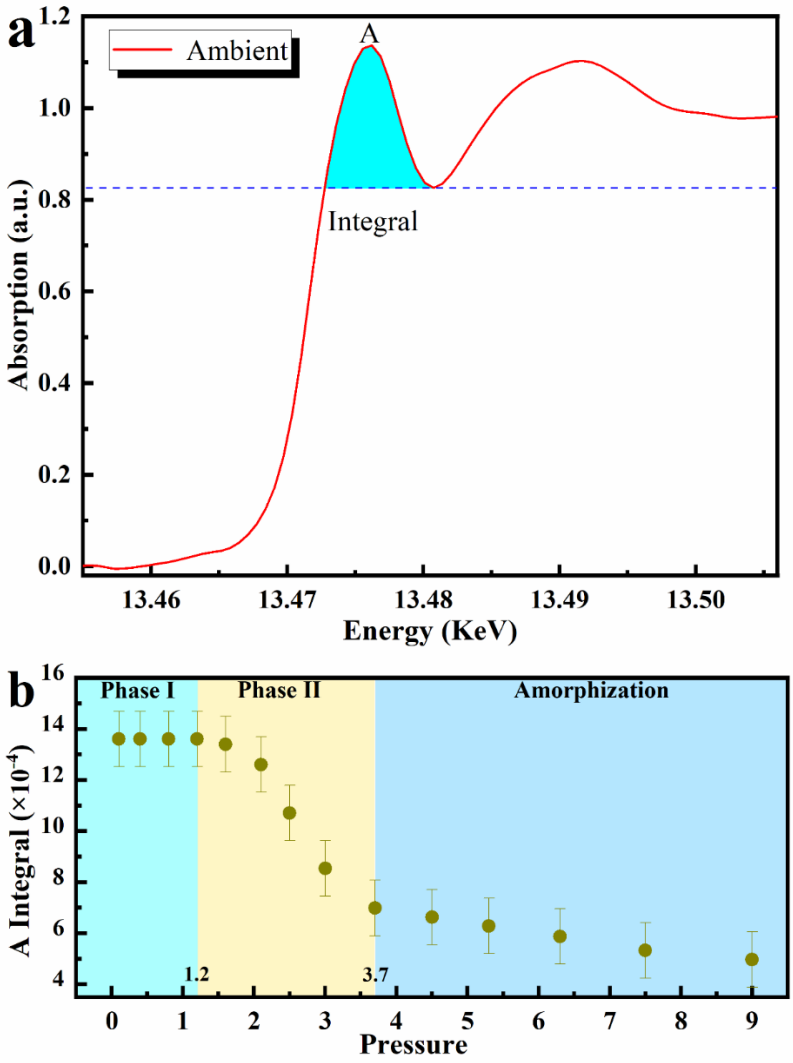

Figure 3.18 The area of the white line peak for integration and its change with pressure.

Previous studies have shown that the competition between the two compression effects, which originated from the bond length contraction and the octahedral distortions, was responsible for the structural evolution and bandgap.[170] In Phase I, the contraction of the Pb-Br bond and the distortion of the octahedron are coexistent under pressure, but the effect of bond length contraction is stronger than octahedral distortion. Therefore, the bandgap is gradually reduced, but it has less effect on the electronic structure. So, the integral of the white line does not change below 1.2 GPa. On the contrary, in Phase II, the compression of the crystal structure mainly comes from the octahedral tilt and distortion, which strongly affect the electronic structure

compared to Pb-Br bond contraction in this regime. Thus, the integral of the white line decreases with pressure increasing. This is associated with the pressure-induced bandgap broadening in Phase II of $CsPbBr_3$. When the pressure exceeds 3.7 GPa, $CsPbBr_3$ begins to be amorphous, resulting in the integral of the white line decreasing continuously.

To obtain an intuitive view of the structural changes of $CsPbBr_3$ under pressure, we performed Fourier transform (FT) on the EXAFS data at Pb L3-edge as shown in Figure 3.19. With the limited energy range of the EXAFS data, we can only get the first-neighbor distance, the bond length R of Pb-Br. As shown in Figure 3.19 (a), the Pb-Br distance decreases continuously with increasing pressure.

Figure 3.19 (b) plots the Pb-Br distance (top) and peak intensity (bottom) changes with pressure, we can see that there are two inflection points at 1.3 and 3.7 GPa, which are caused by the phase transition. From ambient to 1.3 GPa, the Pb-Br distance decrease slowly due to the compression of the lattice by pressure. This will also change the bandgap of $CsPbBr_3$. As is known, the bandgap was exclusively distinguished by the separation of the conduction band minimum (CBM) and valence band maximum (VBM). The previous studies[156] have shown that the $CsPbBr_3$ perovskites exhibited an inverted band structure since the VBM was identified as the antibonding hybridization between the Pb 6s and Br 4p orbitals, whereas the CBM state was governed by the orbital interactions between Pb 6p and Br 4s orbitals in the $[PbBr_6]^{4-}$ octahedral network. Note that the VBM state has mainly come from the Br 4p character, owing to the higher energy level of the Br 4p orbital compared with that of the Pb 6s state. The CBM was almost totally contributed from the Pb 6p state because the Pb 6p orbital possessed a much greater energy level than the Br 4s state. When the pressure was applied to $CsPbBr_3$ perovskites, the CBM was mostly a nonbonding localized state of Pb 6p orbitals, which is less sensitive to

external pressure stimulus. Therefore, the band-gap evolution of $CsPbBr_3$ perovskites was initially determined by the change of VBM when pressure is applied.[194] With the increase of pressure, the Pb-Br distance became shorter, the enhanced orbital coupling between the Pb 6s and Br 4p states pushed up the VBM due to its antibonding character, which explains the red-shift of the bandgap with pressure (as shown in Figure 3.1 and 3.2).

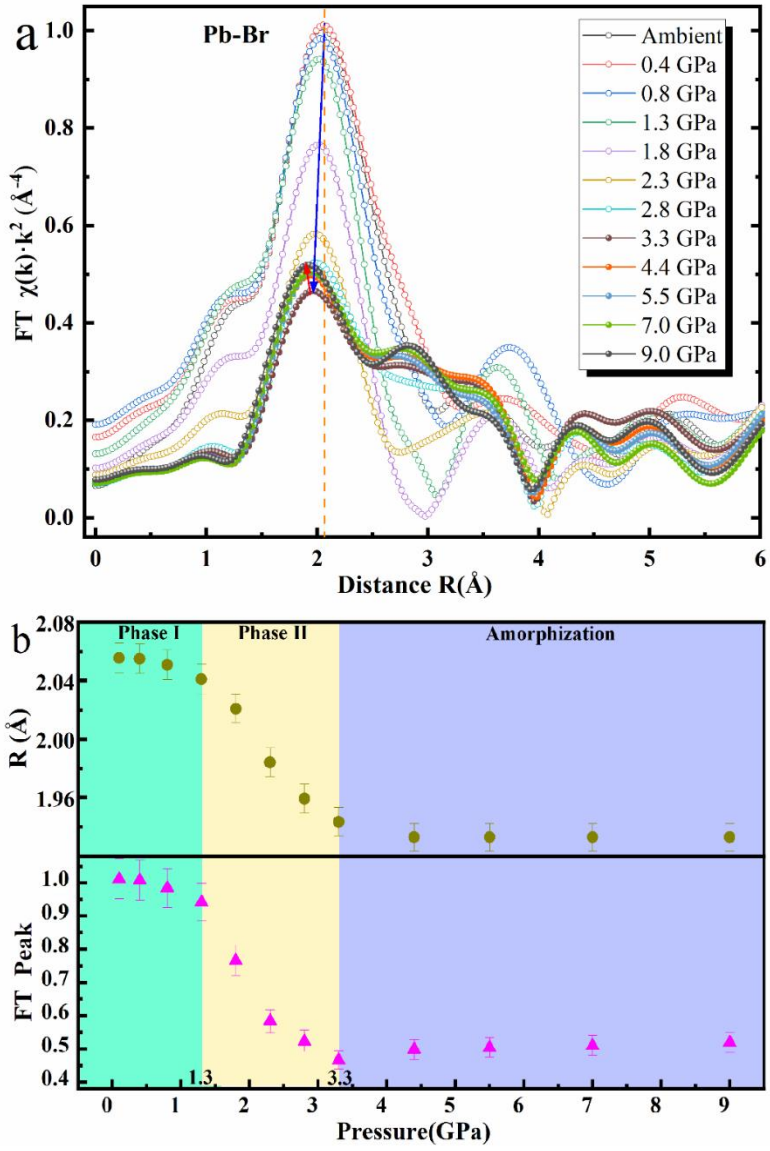

Figure 3.19 (a) The Fourier transformed EXAFS of $CsPbBr_3$, (b) Pressure dependence of the Pb-Br distance and the intensity of the Pb-Br peak.

From 1.3 to 3.7 GPa, the Pb-Br distance continues to decrease, which is

attributed to the distortions and contractions of the $PbBr_6$ octahedra.[170] When the Pb-Br distance continues to decrease under high pressure, the CBM happened to be dominated by the strong coupling of the Pb 6p and Br 4p orbitals. Accordingly, the CBM shift to the higher energy level by the application of pressure, thereby leading to the widened bandgap. When the pressure exceeds 3.7 GPa, $CsPbBr_3$ begins to be amorphous, the trend of the changes of Pb-Br distance and peak intensity becomes gentle.

The intensity of the FT peak reflects the number of Br atoms around Pb, it decreases continuously from ambient pressure to 3.7 GPa (as shown by the blue arrow in Figure 3.19 (a) then increases when the pressure is above 3.7 GPa (red arrow). Since the $PbBr_6$ octahedra are stable, loss of Br is not expected at 3.7 GPa. One possibility is that the distortion of the octahedron induced by pressure changes the positions of the Br atoms and the distances between Pb and Br. Further studies are needed.

3.6 Conclusions

In situ AC impedance spectroscopy, photocurrent, and XAS measurements under high pressure were performed on $CsPbBr_3$ samples using the high-pressure diamond anvil cell technique. The measurement results of AC impedance spectroscopy showed that with the increase of pressure, the electrical parameters of $CsPbBr_3$ powder changed discontinuously at 1.2 GPa and 2.9 GPa, which was caused by the phase transition. $CsPbBr_3$ undergoes an isostructural phase transition from (Pbnm-0 GPa) to (Pbnm-1.2 GPa) at 1.2 GPa, and amorphization started from 2.9 GPa. The dependence of electronic resistance, ion resistance, grain boundary resistance, grain resistance, and ion diffusion coefficient with pressure was obtained by different equivalent circuit fitting, and the reason for the change of ion resistance was explained by the ion diffusion coefficient. By comparing the impedance spectroscopy data of

$CsPbBr_3$ powder and single crystal, we found that the transition from mixed ionic/electronic conduction to pure electronic conduction occurred at 2.3 GPa for both samples. Therefore we believe that the property of pressure-induced ion/electron conduction to electron conduction in $CsPbBr_3$ is an intrinsic property of $CsPbBr_3$. Grain boundaries affect the value of impedance, but not its trend. The photocurrent measurement results show that the pressure can enhance the photoelectric response of $CsPbBr_3$, and the photocurrent reaches the maximum at 1.4 GPa.

The measurement results show that $CsPbBr_3$ undergoes a phase transition at 1.2 GPa, and the sample becomes amorphous when the pressure exceeds 3.7 GPa. We confirmed the possibility of isostructural phase transition from Pbnm to Pbnm at 1.2 GPa using theoretical calculations using the MXAN code. In addition, we can accurately obtain the change of Pb-Br bond length with pressure through the Fourier transform results and analyzed the effect of the change of bond length on the bandgap. Our work not only provides insight into the microscopic electrical transport properties of $CsPbBr_3$ but also suggests that the conversion efficiency of $CsPbBr_3$-based devices can be improved by pressure.

Chapter 4

The EXAFS investigation of local structural changes in 2D layered materials at high pressure

4.1 EXAFS study of TMDs under pressure

4.1.1 Introduction

The transition metal dichalcogenides (TMDs) MX_2 (M, transition metal, W, Mo, Re, Rb, Tc, etc; X, chalcogen, S, Se, Te) have become a topic of interest in recent years due to their unique structural, electronic, optical, and tribological properties.[52, 195-203] Up to now, there are approximately more than 60 TMDs reported,[204] and most of them have a layered structure resembling graphite, but the stacking of these layers is different. In the layers of TMDs, a transition metal atom layer is sandwiched by two chalcogen atom layers, forming an X–M–X sandwiched structure. The X–M–X trilayers then stack together via weak van der Waals (vdW) interaction, resulting in the different phases in TMDs such as T (trigonal), H (hexagonal), or R (rhombohedral) phase.[205-210] Eleven different polytype structures have been observed up to now in TMDs.[205, 211] Therefore, TMDs exhibit a variety of exotic transport properties such as quantum spin Hall effect,[212] charge-density waves,[213-215] and superconductivity,[216-218] thus enabling many potential applications.

The most common form in TMDs is the H phase, whereas T phases are reported to be metastable. However, ReS_2 is an exception, in which the most stable form under ambient conditions is a distorted 1T phase with triclinic symmetry, due to the pronounced Peierls distortion.[204, 219-221] Unlike in other TMDs, Peierls distortion of the 1T structure of ReS_2 weakens the interlayer coupling interaction, which in turn hinders S-Re-S layers from stacking orderly[219] in the bulk ReS_2.

High pressure has been proved an effective way to tune the physical properties of materials via modifying the atomic and electronic structures.[195, 198, 222-223] In 2010, Hou et al. reported that ReS_2 undergoes a phase transition around 10.5 GPa based on x-ray diffraction studies. Unfortunately, the crystal structure of the high-pressure phase could not be determined due to the insufficient quality of XRD data.[224] Then, Wang et al. investigated the structure evolution, electrical transport, vibrational properties, and visible-light response of ReS_2 under high pressure up to 50 GPa combined with ab initio calculations. Both in situ XRD and theoretical calculations suggest that ReS_2 undergoes a structural transition from the distorted-1T to distorted-1T' phase at ~7.7 GPa or lower pressure.[225] From the inflection points in the ratio of Raman mode intensities and change in the slope of Raman mode values with pressure in combination with first-principles calculation, an intralayer transition followed by an interlayer transition in the range of 8–19.6 GPa is reported by Yan et al.[226] The structural transformation of ReS_2 from distorted-1T to distorted-1T' phase is only due to the change of the stacking order,[227] which is difficult to distinguish. Therefore, the results obtained by different groups are not consistent.

EXAFS is a powerful method for studying local atomic configurations and electronic structures. In this work, we studied the local geometric and electronic structural changes of ReS_2 up to 70.3 GPa by quantitatively analyzing the EXAFS data at Re L3-edge.

4.1.2 Experiments

The studied ReS_2 crystals were grown by the chemical vapor transport technique (CVT). Additional details regarding the sample synthesis can be found in Ref. [228] and [229]. The layered ReS_2 crystals have a thickness of 20-100 μm, an area of 5-200 mm^2, and a purity higher than 99.99%. The Raman spectrum of ReS_2 crystals we measured is shown in Figure 4.1, which is consistent with the previously reported result,[225-226] confirmed no contamination.

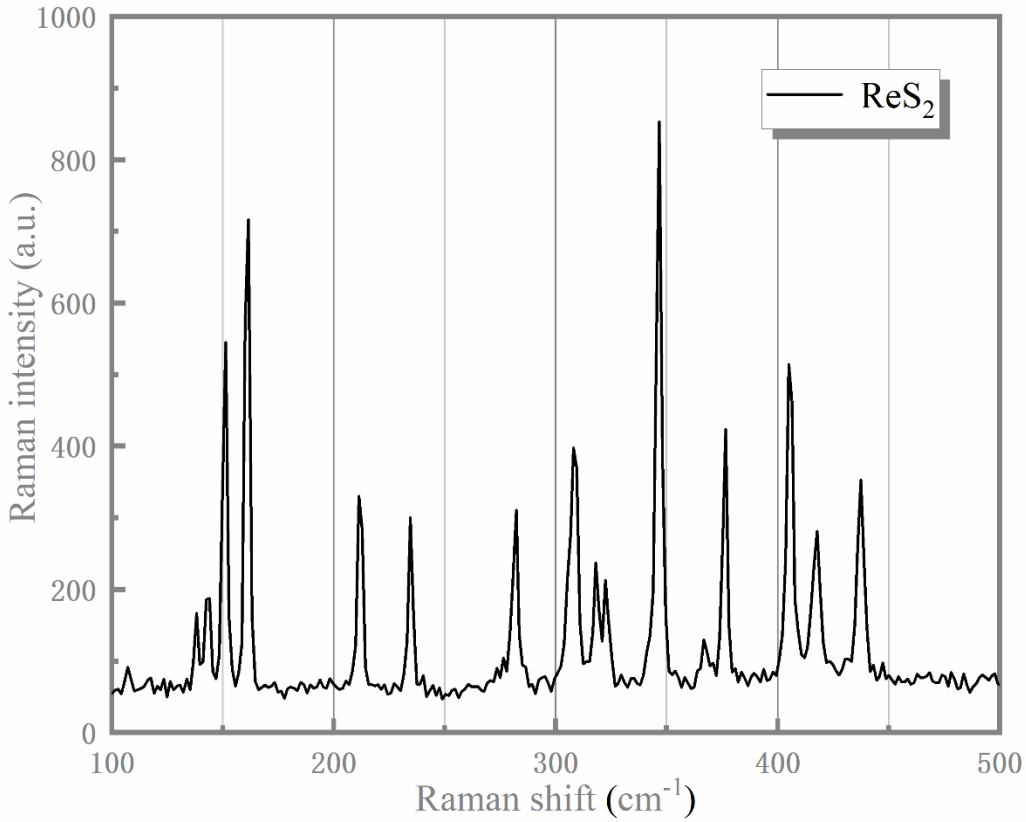

Figure 4.1 Raman spectrum of ReS_2 crystals.

The high-pressure Re L_3-edge EXAFS measurements at room temperature have been performed using the dispersive XAS setup (Figure 2.12) at the ODE beamline of Synchrotron SOLEIL.[132] A rhenium gasket was pre-indented to a thickness of 50 μm, and a hole of 125 μm in diameter was drilled in the center. ReS_2 samples have been loaded into the hole with silicone oil as the pressure

medium and subjected to high pressure up to 70.3 GPa in a membrane DAC with a diamond size of 300 μm. The pressure was measured in a standard way using the ruby fluorescence line shift. The normalization of the spectra and the EXAFS signal treatments were carried out using the Demeter package.[121]

4.1.3 Experimental results and data analysis

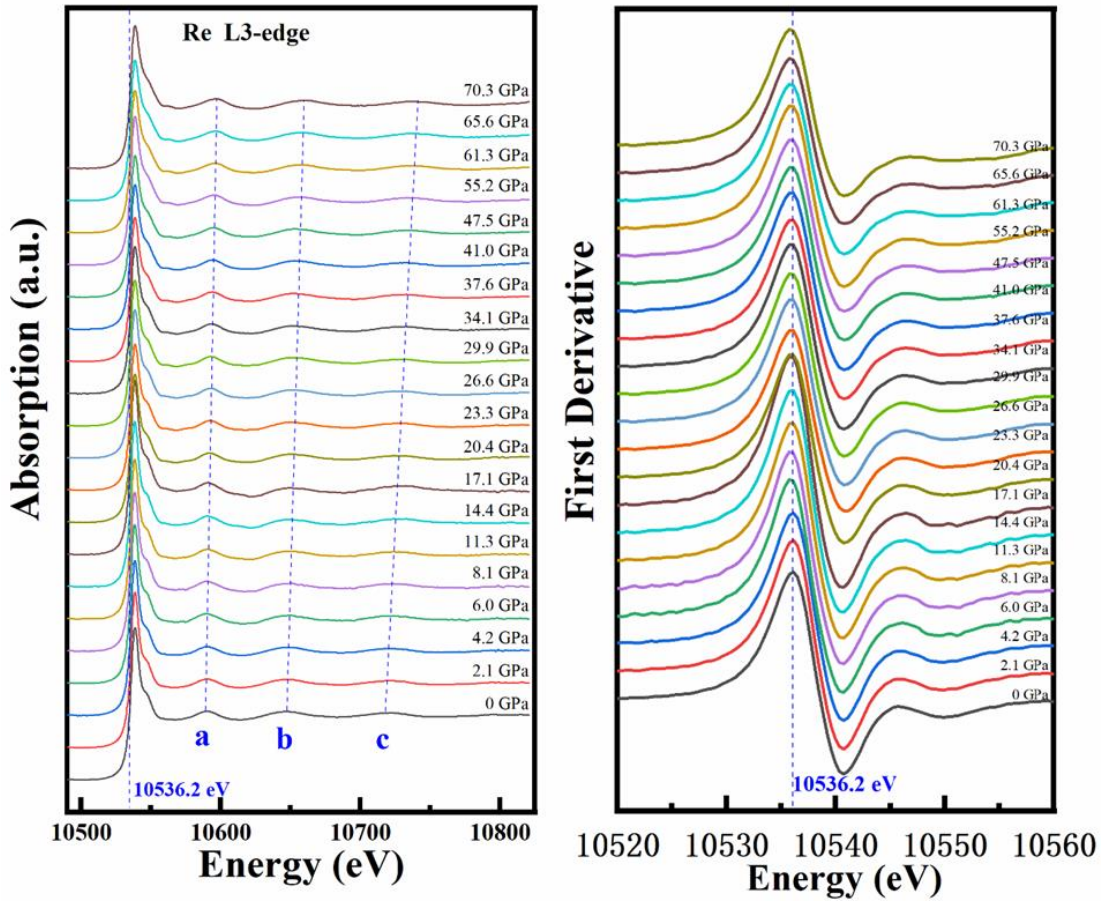

Figure 4.2 The vertically shifted XAS spectra (left) at Re L3-edge and the first derivative of the spectra (right) under various pressure.

Figure 4.2 shows the pressure dependence of X-ray absorption spectroscopy (XAS) of ReS_2 at the Re L3-edge up to 70.3 GPa. All the spectra were normalized. The white line, which comes from the $2p_{3/2} \rightarrow 5d$ dipole allowed transition, reflects the unoccupied electron density of the Re 5d orbitals. The absorption-edge energy E_0 (10536.2 eV) was obtained at the first maximum of the first derivative of the absorption spectra. We noticed that no significant change of

E_0 was observed across the entire pressure range, as illustrated by the position of the dotted line in Figure 4.2. But as the pressure increases, the white line peak gradually widens.

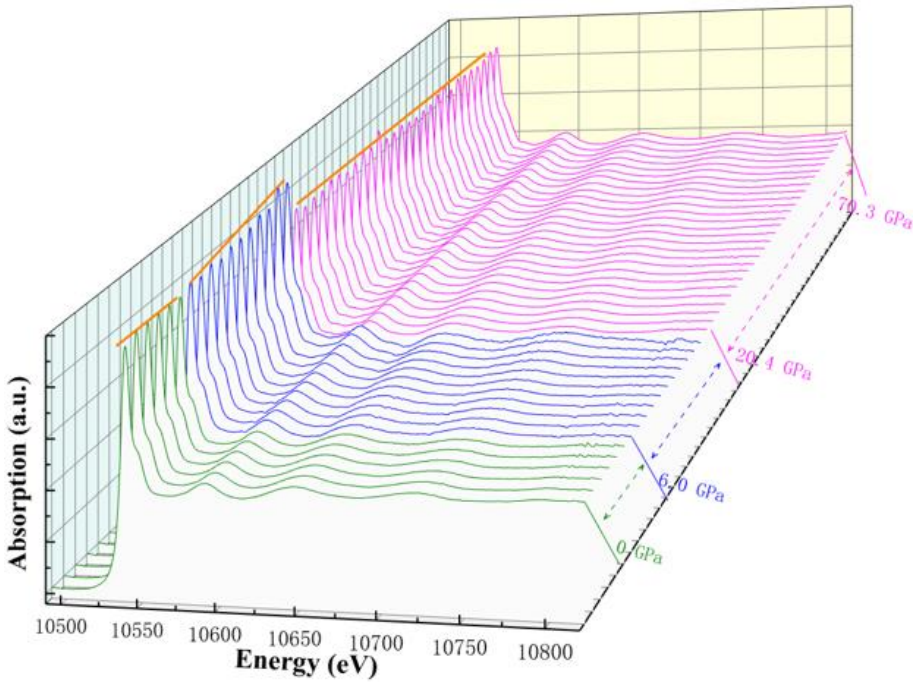

Figure 4.3 The three-dimensional plot of Re L3-edge XAS under pressure.

The height of the white line changes with pressure, which can be seen more intuitively from the three-dimensional plot as shown in Figure 4.3. The white line from 0 to 6 GPa did not obviously change and gradually increased from 6 to 20.4 GPa. When the pressure exceeds 20.4 GPa, the white line changes significantly. Previous research believed that broadening of the Re 5d electronic band with increasing pressure is introduced by lattice contraction because of the enhanced overlap between Re 5d electronic orbitals. This gives rise to a decrease in density of state in the occupied and unoccupied 5d states, resulting in changes in the height and width of white-line profiles.[125] Previous studies have shown that the VBM and CBM of ReS_2 mainly contribute from hybridized Re-d and S-p states.[225, 230] The VBM state has mainly come from the S 3p character, and the CBM state comes from the Re 5d character.[226] However, the

bandgap tends to change with pressure. These changes are often associated with pressure-induced structural phase transition.

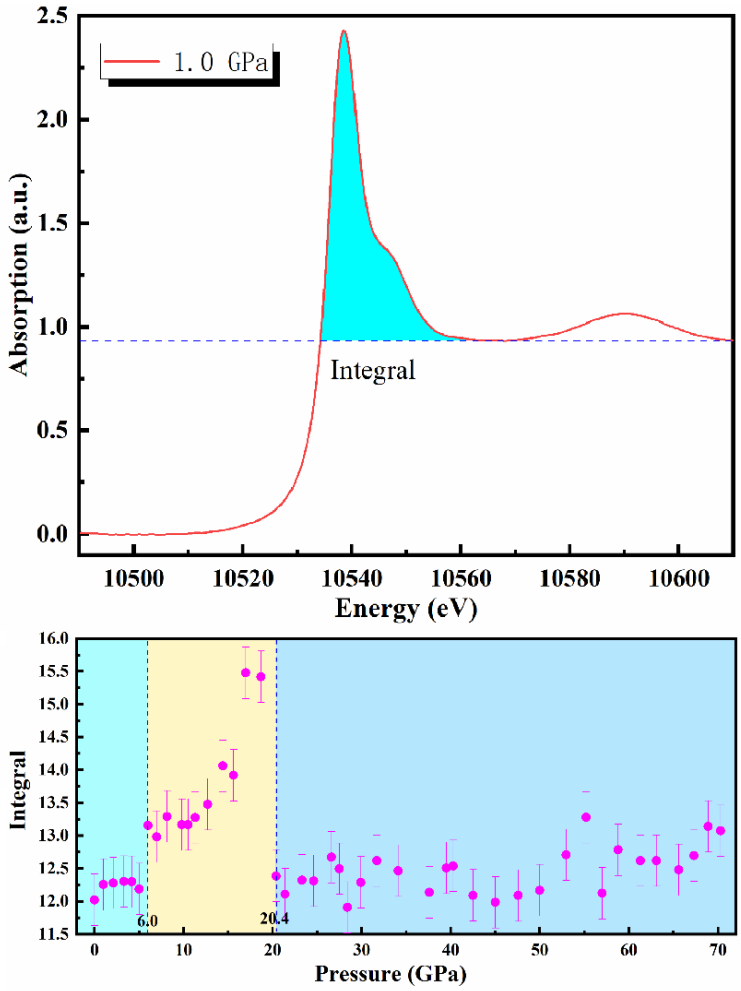

Figure 4.4 The integrated area of the white line peak (top) and its change with pressure (bottom).

We integrated the white line area and their changes with pressure are shown in Figure 4.4. We believe that the abrupt intensity changes at 6.0 and 20.4 GPa are caused by the phase transition of ReS_2. Previous experimental and theoretical results by Hou et al.[224] and Wang et al.[225] showed that ReS_2 undergoes a structural transition from the distorted 1T to distorted 1T' phase around 7.7 GPa or lower pressure, as illustrated in Figure 4.5.

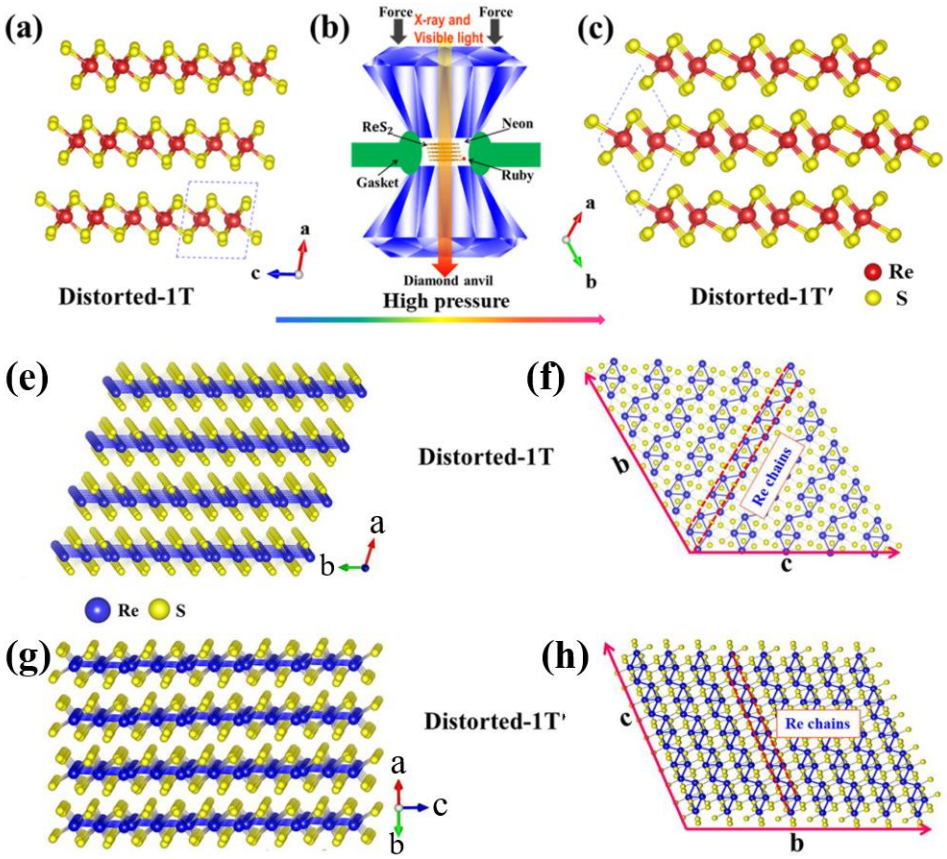

Figure 4.5 (a) The cross-section illustration of layered distorted-1T ReS_2. (b) Schematic diagram of the high-pressure diamond-anvil cell setup. (c) The cross-section illustration of layered distorted-1 T' ReS_2. (e-h) Structure details of distorted 1T and 1T′ ReS_2. (e) The cross-section illustration of distorted 1T ReS_2 layers direction along a-axis. (f) Top view of the layer structure of a monolayer distorted 1T ReS_2. Unit cell and Re chains are highlighted. (g) The cross-section illustration of distorted 1T′ ReS_2 layers along $\overrightarrow{xy}$ direction. (h) Top view of the layer structure of a monolayer distorted 1T′ ReS_2. Unit cell and Re chains are highlighted.[225]

As shown in Figure 4.5 (a), in each layer sulfur atoms form octahedral coordination around rhenium atoms. By sharing the edges, [ReS_6] octahedra are packed together in the bc plane, forming the ReS_2 monolayer perpendicular to the a-axis. From 0 to 6 GPa, different layers are compressed along the c-axis as the pressure increases, but not enough to break the [ReS_6] octahedron. Therefore, the integral of the white line does not change significantly. The electron localization function (ELF) calculation by Yan et al.[226] also showed the same result. Increased pressure will lead to the obvious enhancement of the S-

S interaction between the layers, the formation of covalentlike bonding of S–S at high pressure,[225] and the electrons between the layers tend to be delocalized gradually. Therefore, when the pressure exceeds 6 GPa, the integral of the white line increases rapidly with the increase of pressure. Referring to previous high-pressure Raman results, this interlayer transition (S-S covalentlike bond) was mainly caused by the counterclockwise rotation of S atoms around the chain of Re atoms.[226] The theoretical calculation results of Zhou et al. also confirmed this conclusion.[204] Hence, we attributed the change at 6.0 GPa to the intralayer transition.

Previous XRD studies on ReS_2 under high pressure did not discover the phase transition around 20 GPa.[224-225] But in our work, the integral of the white line changes significantly at 20.4 GPa, as shown in Figure 4.4 bottom. Yan et al's high-pressure Raman study showed that the layered ReS_2 undergoes an interlayer transition around 19.6 GP.[226] Specifically, previous theoretical calculations have indicated that ambient ReS_2 is randomly stacked because shifting one ReS_2 monolayer over another does not lead to any significant change in total energy owing to its weak interlayer coupling.[219] However, the stacking configuration upon compression should be quite different from that at ambient conditions as the stronger interlayer coupling under high pressure would prompt an ordered stacking,[231-232] which leads to the electrons between layers becoming localized. Thus, the white line integral decreases abruptly at 20.4 GPa, but this transition from disordered to ordered stacking does not change the phase structure of ReS_2. Pinku Saha et al. reported that after the distorted 1T to distorted 1T' phase transition in ReS_2, the distorted 1T' phase remained up to 42 GPa,[233] so the integral of the white line remained in a relatively stable range without significant change. Here, we attribute the phase transition at 20.4 GPa to the interlayer transition from disordered to ordered stacking.

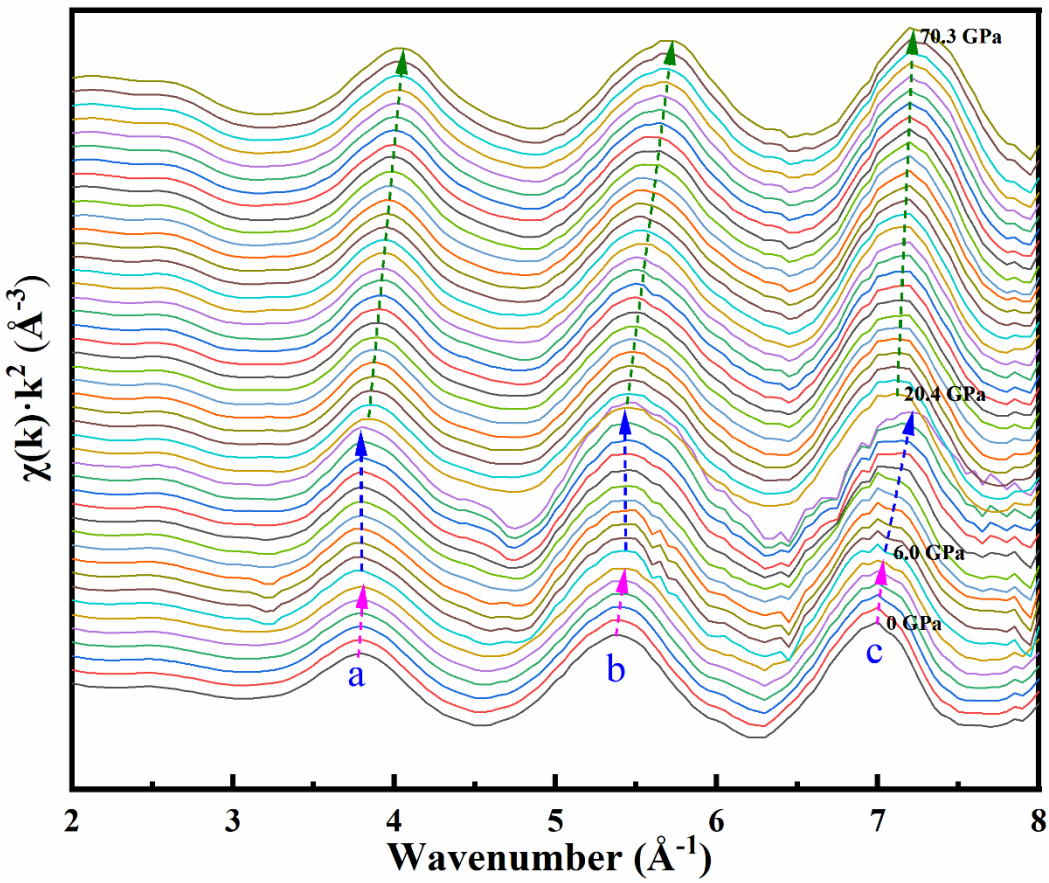

Figure 4.6 Re L3-edge EXAFS $\chi(k)k^2$ spectra at selected pressure points. The pressures shown in the figure start from 0 to 70.3 GPa with a step of 1~2 GPa.

As shown in Figure 4.6, pressure-dependent experimental Re L3-edge EXAFS $\chi(k)k^2$ spectra of ReS_2 were obtained following the conventional procedure[234] using the Athena package,[121] the details have described in Chapter 2. The photoelectron wavenumber k is defined as $k = \sqrt{2m(E - E_0)}/\hbar$, where m is the electron mass, $\hbar$ is Plank's constant, E is the X-ray photon energy, and E_0 is the origin of the photoelectron kinetic energy. With increasing pressure, a shift of the EXAFS oscillations to higher k values is usually expected due to the contraction of bond lengths. But the evolution of all peaks is not like this, and two discontinuous changes at 6.0 and 20.4 GPa are clearly, as shown in Figure 4.6. This is strong evidence in favor of a structural transformation in the ReS_2.[235]

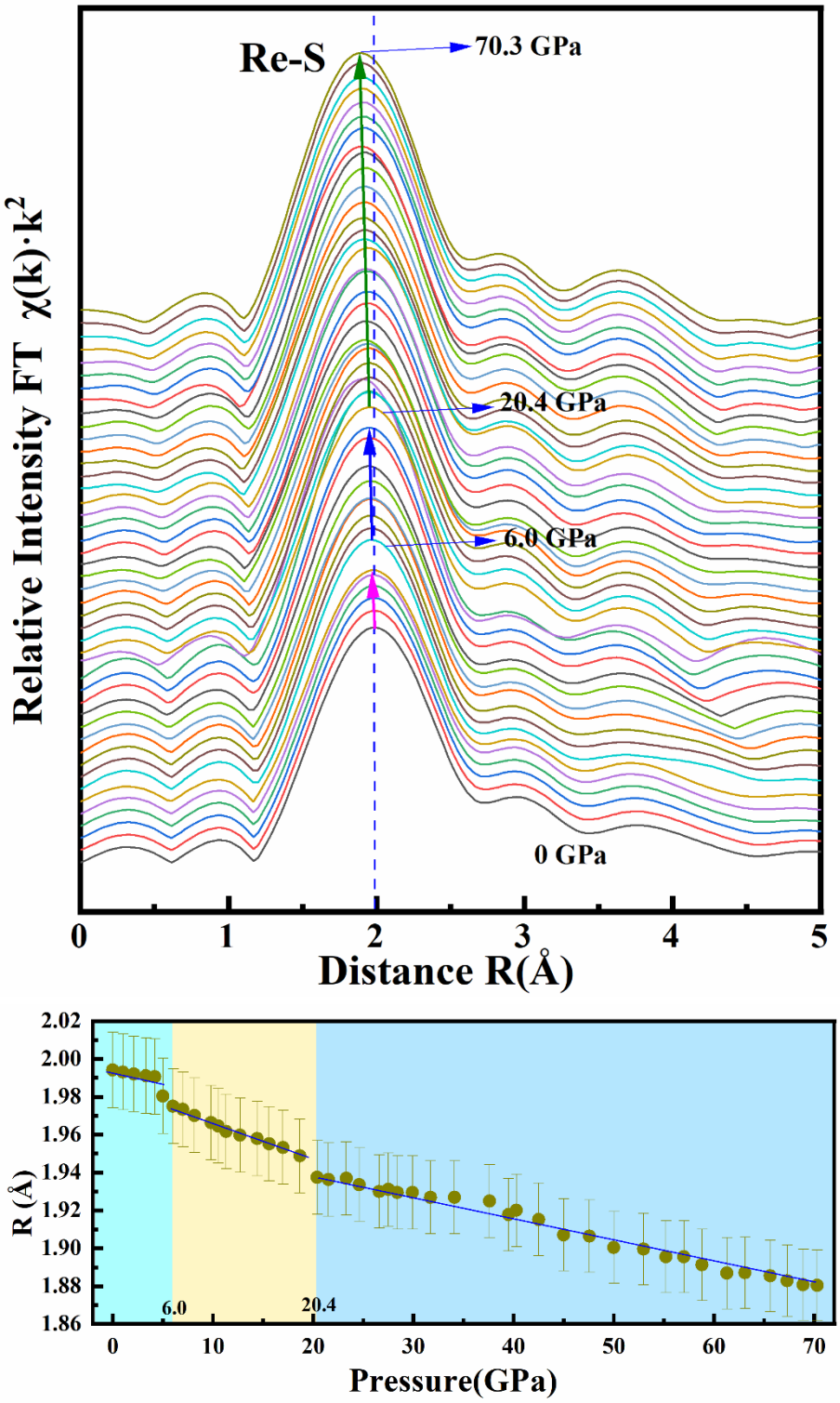

Figure 4.7 The Fourier transformed EXAFS of ReS_2 (top), and pressure dependence of the Re-S distance (bottom).

The Fourier transforms (FTs) at selected pressure points are shown in Figure 4.7. With the limited energy range of the EXAFS data, we can only get the first-neighbor distance, the bond length R of Re-S. The FTs were calculated in the k-

space range of 3-8 $Å^{-1}$. In the entire pressure range, the Re-S bond lengths gradually become shorter as the pressure increases, and two discontinuous changes at 6.0 and 20.4 GPa are clear, which are caused by intralayer and interlayer transition respectively. Note that the FTs were not corrected for the backscattering phase shift of atoms; therefore, the positions of all peaks are displaced to smaller distances relative to their crystallographic values.

As mentioned above, when the pressure is below 6.0 GPa, the [ReS_6] octahedron is relatively stable, different layers are compressed along the c-axis direction, and there is no structural phase transition, so the Re-S bond lengths became shorter slightly. At 6.0 GPa, ReS_2 undergoes a structural phase transition from the distorted 1T to distorted 1T' phase, with enhanced interlayer coupling and S-S covalentlike bond formation between layers, which is mainly caused by the counterclockwise rotation of S atoms around the chain of Re atoms, this causes a sudden change in the R-S bond length and still became shorter. When the pressure exceeds 20.4 GPa, ReS_2 undergoes an interlayer transition from disordered to ordered stacking, and the Re-S bond length was further shortened.

A quantitative analysis of the EXAFS signals was carried out using the ARTEMIS package.[121] Combining the existing structural information of ReS_2 at ambient and high pressure,[225, 236] we can fit the Re-S bond length using the FEFF6 code accurately, and then obtain the local structural information at the selected pressure point, as shown in Figure 4.8. The fitting range was 1.15-2.7Å.

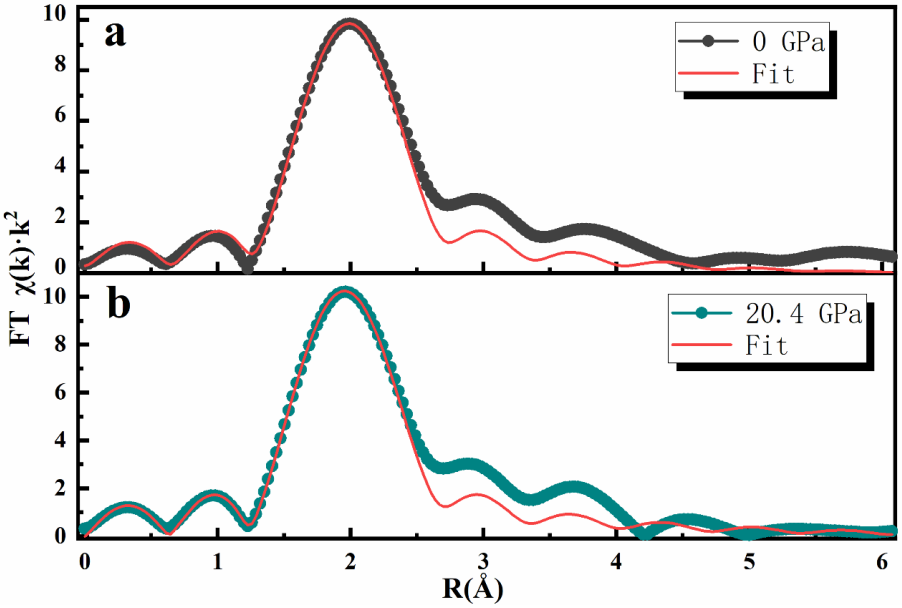

Figure 4.8 Local structural fitting analysis at 0 and 20.4 GPa.

Table 1 Corresponding fitting parameters in Figure 4.8 a and b.

Pressure	N	S_0^2	$\Delta\sigma^2(Å^2)$	ΔE_0 (eV)	ΔR(Å)	Reff(Å)	R(Å)	R-factor
0 GPa	6.000	0.864	0.00309	12.514	0.08735	2.32600	2.41335	0.0079591
20.4 GPa	6.000	0.873	0.00336	13.350	0.05038	2.32750	2.37788	0.0068923

From our fitting analysis, we obtained the number of S atoms surrounding Re, the debye-waller value, and the accurate Re-S bond length, which decreases from 2.413 Å at ambient pressure to 2.378 Å at 20.4 GPa.

4.2 EXAFS study of black Arsenic under pressure

4.2.1 Introduction

Since the successful exfoliation of graphene by Geim et al in 2004,[237] numerous layered materials, such as transition metal dichalcogenides,[238-241] transition metal oxides,[242] black phosphorus (bP), and hexagonal boron nitride,[243-247] have become the focus of research in the field of 2D materials because of their unique electronic, optical, and thermal properties. Layered black arsenic (bAs),

a cousin of bP, with the A17 phase, has a puckered honeycomb structure similar to bP. bAs is a metastable phase of arsenic. It is found that the bandgap of bAs depends strongly on their thickness. For example, bulk bAs is a semiconductor with a direct bandgap of ~0.3 eV. Its bandgap increases up to 1.4 eV at the monolayer limit because of the quantum confinement effect. The bandgap remains direct from its bulk to the bilayer state, while that for the monolayer state is indirect.[248] In addition, bAs show strong in-plane anisotropic electronic and thermal properties.[45] With these unique properties, bAs are therefore promising for novel field-effect transistors and photodetectors. The structural, electronic, and optical properties of materials can be manipulated using certain effective means, such as applying pressure, an electric field, a magnetic field, or a substrate.[225, 249-252]

Among the three allotropes, bAs, gray arsenic (gAs), and yellow arsenic (yAs).[45, 253] The bAs that are used for electronic devices are from natural minerals.[254] However, as bAs is a metastable phase, there has been little research on its stability, which is important for its synthesis and electronic and optical applications. Hydrostatic pressure is a powerful means of modifying the structure and physical properties of materials.[98] Some progress has been made in the study of 2D materials under high pressure. For example, Cheng et al reported that a pressure-induced phase transition from 2Hc to 2Ha occurs in bulk and monolayer MoS_2 at ~19 GPa and ~25.6 GPa, respectively,[255] and for multilayered single-crystal MoS_2 there is a transition in the electronic structure from semiconducting to metallic at ~19 GPa.[222] Gong et al reported that pressure induces a topological Lifshitz transition from semiconductor to Dirac semimetal for bulk bP at ~1.2 GPa,[256] and Li et al reported that pressure induces a phase transition from bP (A17) to blue phosphorus (A7) at ~5 GPa and then to a simple cubic phase at ~10 GPa.[257] However, despite the growing investigations on 2D materials, related research about how high pressure affects

layered bAs has been rare to date. This motivates us to carry out a detailed EXAFS study of the structural and electronic properties of bAs under hydrostatic pressure. EXAFS data at As K-edge were collected from ambient to 20.1 GPa to explore the structure evolution of bAs under pressure.

4.2.2 Experiments

The bAs crystals we used in the experiment were purchased from 2D semiconductor Inc. with 6N purity. The Raman spectrum of bAs crystals shown in Figure 4.9, which is consistent with previously reported results,[258] confirmed no contamination.

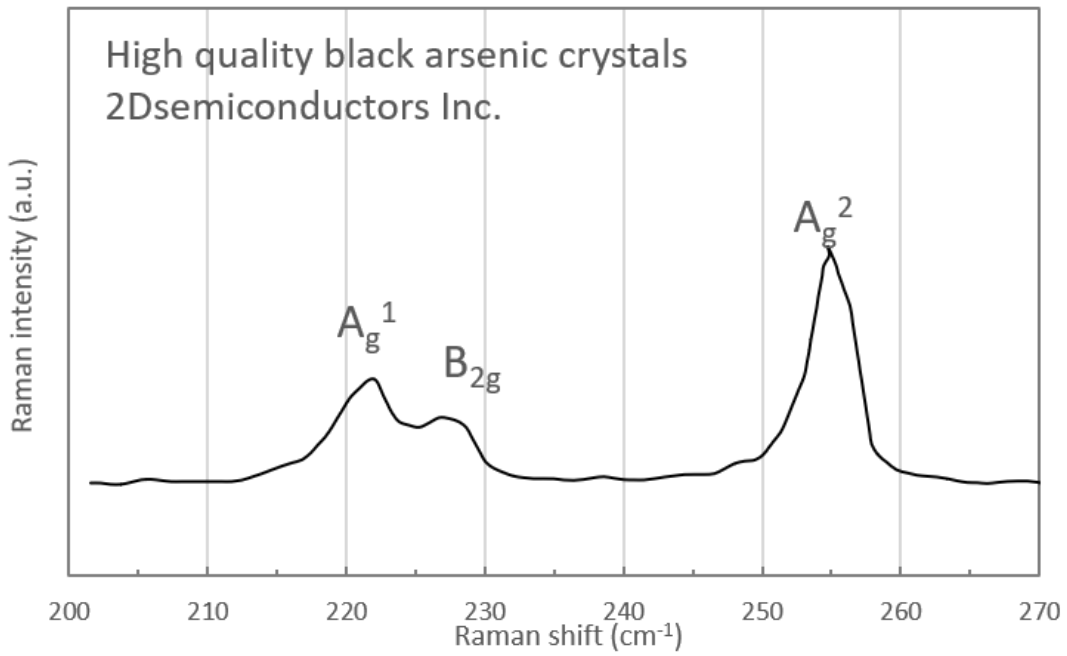

Figure 4.9 Raman spectrum of bAs crystals.

The high-pressure As K-edge EXAFS measurements at room temperature were performed using the dispersive XAS setup (Figure 2.12) at the ODE beamline of Synchrotron SOLEIL.[132] A steel gasket was pre-indented to a thickness of 50 μm, and a hole of 150 μm in diameter was drilled in the center. The bAs were loaded into the hole with silicone oil as the pressure medium and subjected to high pressure up to 20.1 GPa in a membrane DAC with a diamond

size of 400 μm. The pressure was measured in a standard way using the ruby fluorescence line shift. The normalization of the spectra and the EXAFS signal treatments were carried out by using the Demeter package.[121]

4.2.3 Experimental results and discussion

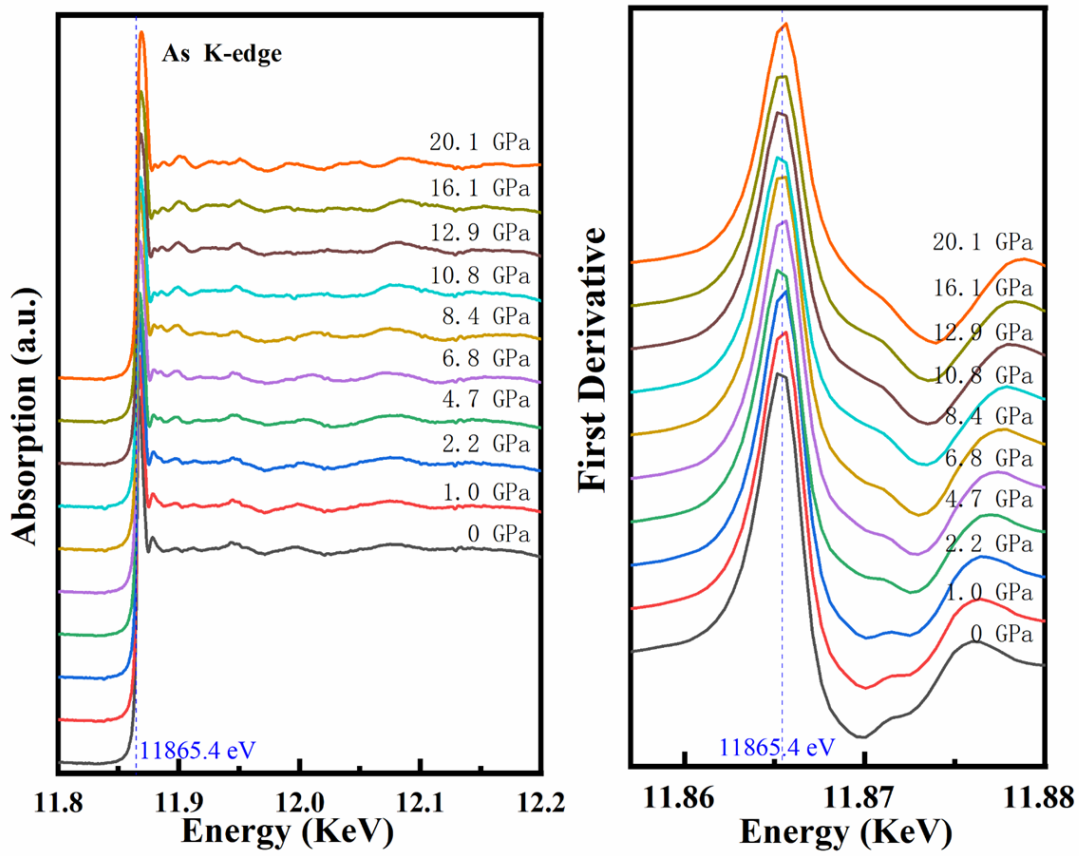

Figure 4.10 The vertically shifted XAS spectra (left) at As K-edge and the first derivative of the spectra (right) under various pressure.

Figure 4.10 shows the pressure dependence of X-ray absorption spectroscopy (XAS) at the As K-edge and the first derivative of the spectra under selected pressures. XAS profiles are characterized by the prominent feature near the edges called white-line, which is due to an electronic transition from the arsenic 1s→4p ty orbitals,[259-260] it will have sharp change when phase transition happens. The absorption-edge energy E_0 was obtained at the first maximum of the first derivative of the absorption spectra. To observe the change of the absorption edge more intuitively, we made a dashed line perpendicular to the

horizontal axis as a reference. We noticed that no significant change of absorption edge was observed across the entire pressure range obtaining an absorption edge of around 11865.4 eV for all of the spectrum.

We used a similar analysis method to ReS_2 as illustrated above. The white line intensities, which are obtained by integrating, shown in Figure 4.11 illustrate the changes of the unoccupied electron density state of the 4p orbital in As. The changes of the integrated white line area with pressure are shown in Figure 4.11. We noticed that the integral of the white line changed discontinuously at 4.7 and 10.8 GPa, which is caused by phase transition, but the data still needs to be analyzed to confirm it.

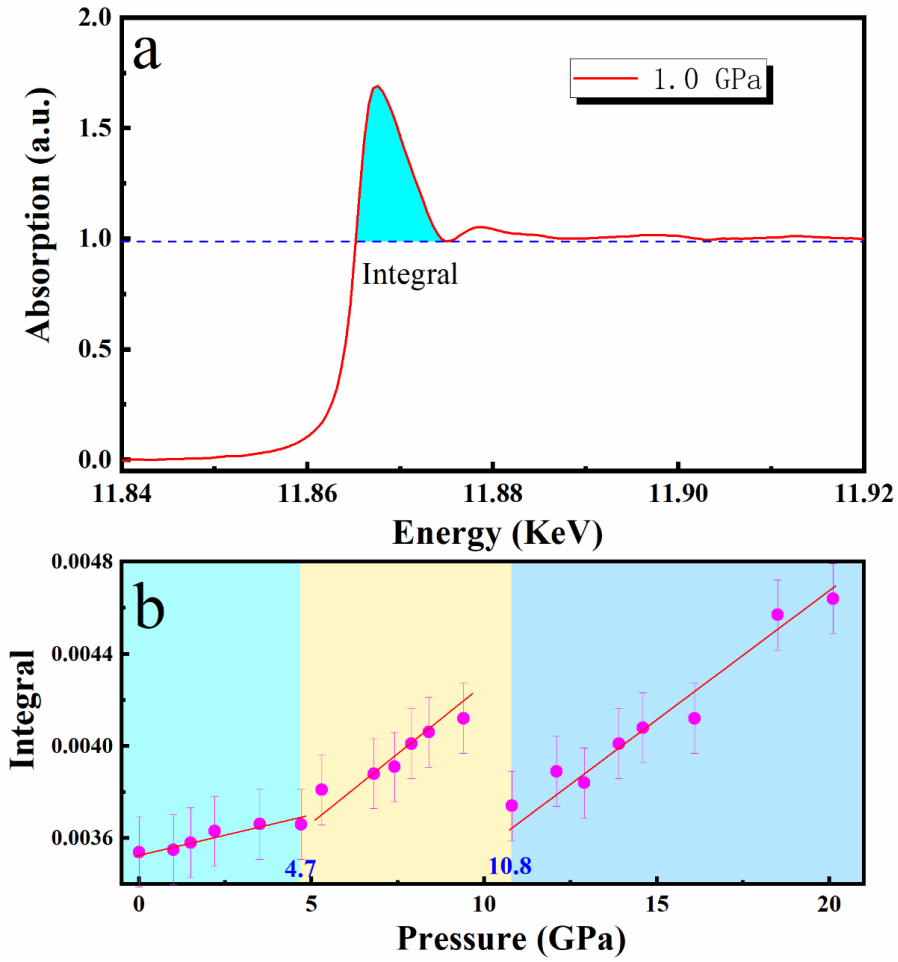

Figure 4.11 The area of the white line peak for integration (top) and its change with pressure (bottom).

As shown in Figure 4.11 b, the integral of the white line increases gradually from 0 to 4.7 GPa. Similar to the change of the white line of ReS_2 in the low pressure range, the increase of the pressure will compress the lattice, and the coupling effect between the layers will be enhanced, which caused some of the interlayer electrons to become delocalized, then leads to the integral of the white line increased. Gao et al. studied the high-pressure Raman of bAs and they observed the bAs (A17 phase) began to transform to gAs with the A7 phase at pressures larger than 3.48 GPa and completely converted to gAs at 5.37 GPa.[258] Figures 4.12 (a) and (c) shows the crystal structures of bAs and gAs, respectively, and the DAC setup for the experiments is shown in Figure 4.12 (b). Therefore, combined with the results of the Fourier transform below, we can confirm that the phase transition from bAs to gAs occurs at 4.7 GPa.

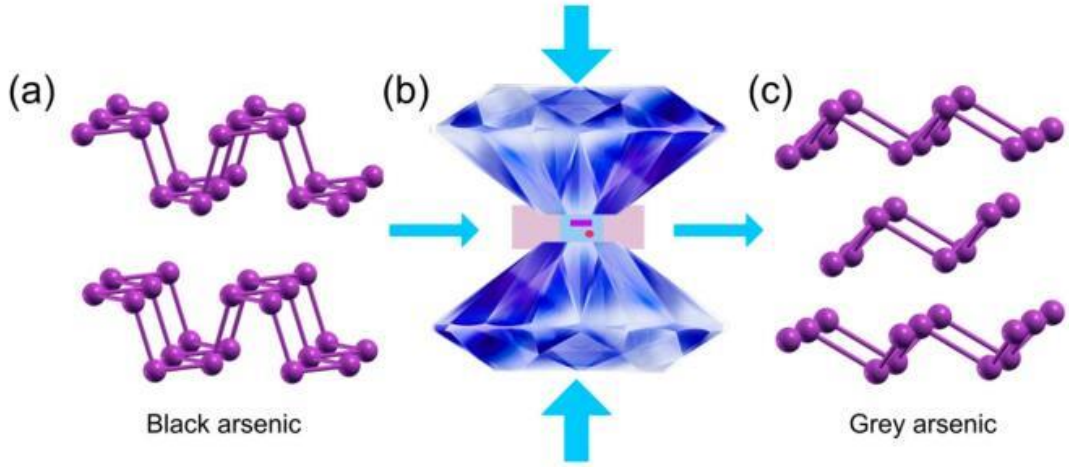

Figure 4.12 Crystal structure of bAs (a) and gAs (c). Schematic diagram of the DAC (b).[258]

However, this phase transition is not simply a lattice deformation via layer shifts and cell compression. Similar to the phase transition process of bP, the phase transition from bAs to gAs under high pressure is attributed to the breaking of intralayer bonds and the formation of new interlayer bonds meanwhile.[261] Figure 4.13 shows the mechanism from bAs (A17) to gAs (A7) transition. During the formation of interlayer bonds, some As atoms will change

from the original three-coordinated to four-coordinated, and the interlayer coupling will continue to increase. Therefore, from 4.7 to 10.8 GPa, the integral of the white line will increase continuously.

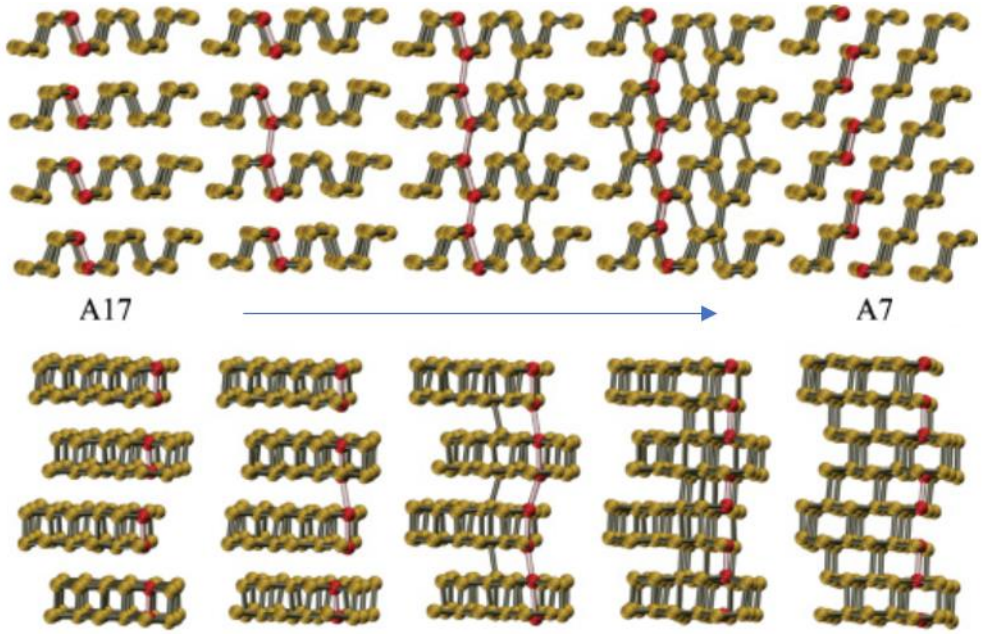

Figure 4.13 Mechanism for the A17→A7 transformation. Compression and layer shuffling of A17 results in interlayer contacts and interlayer bonds, until reconstruction into A7. A vertical bond chain is highlighted and marked throughout. Upper row: orientation as shown in the figure. Lower row: rotated by 90°. Zeroth time frame is set arbitrarily.[261]

Although Gao et al. found the transition from bAs to gAs, they didn't observe the other phase transitions at higher pressures. We observed a significant change in the intensity of the white line peak at 10.8 GPa. The EXAFS spectra at various pressures were collected over 400 eV between 11800 and 12200 eV. Figure 4.14 shows the $\chi(k)k^2$ EXAFS signals as a function of pressure.

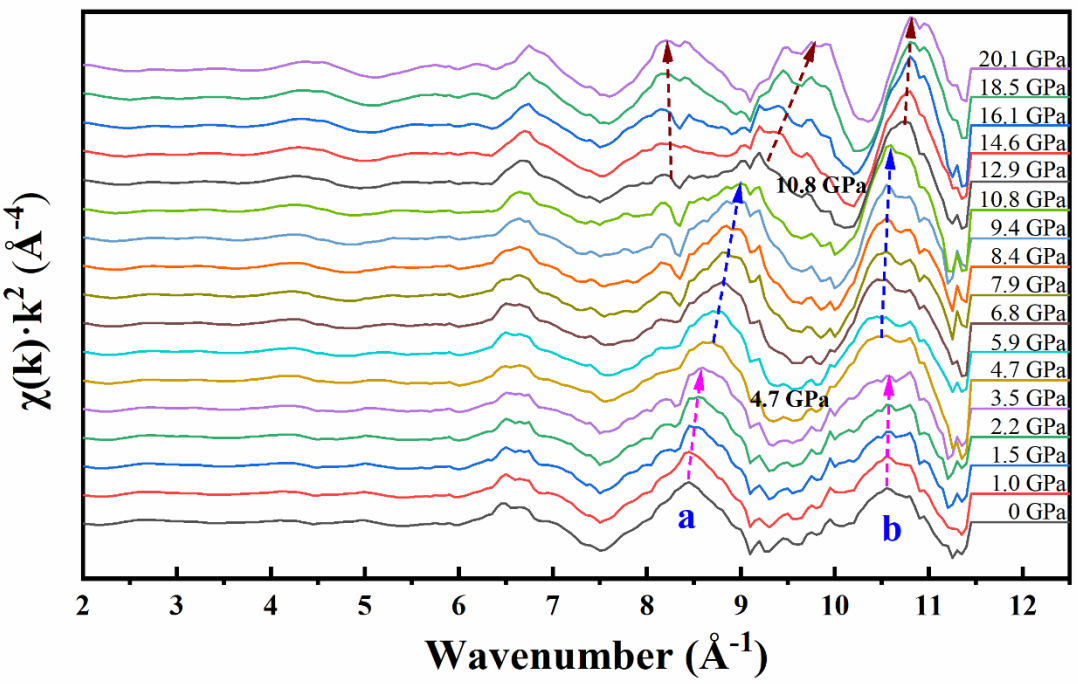

Figure 4.14 As K-edge EXAFS $\chi(k)k^2$ spectra at selected pressures.

With increasing pressure, a shift of the EXAFS oscillations to higher k values is usually expected due to the contraction of bond lengths. But the evolution of peaks a and b is not like this, and two discontinuous changes at 4.7 and 10.8 GPa are clear. When the pressure exceeds 10.8 GPa, peak "a" is split into two peaks shown in Figure 4.14. This is strong evidence of a structural transformation in the sample. Previous theoretical calculations and experimental results indicate that gAs (A7) transform to a simple cubic (SC) phase under a higher pressure of ~25 GPa,[262-263] this also confirmed our experimental conclusions.

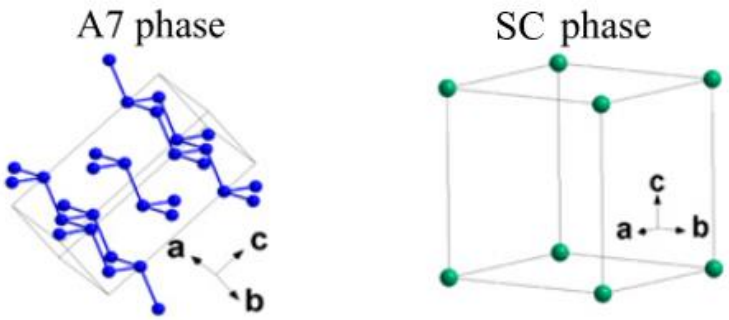

Figure 4.15 shows the structure of the A7 and SC phases.

The phase transition from A7 to SC results in a sudden change in the integral of the white line at 10.8 GPa shown in Fig. 4.11b. But in this process, As atoms gradually transform from the three-coordinated the fully phase-transitioned A7 phase to the six-coordinated SC shown in Figure 4.15,[263] which also results in the integral of the white line increasing continuously.

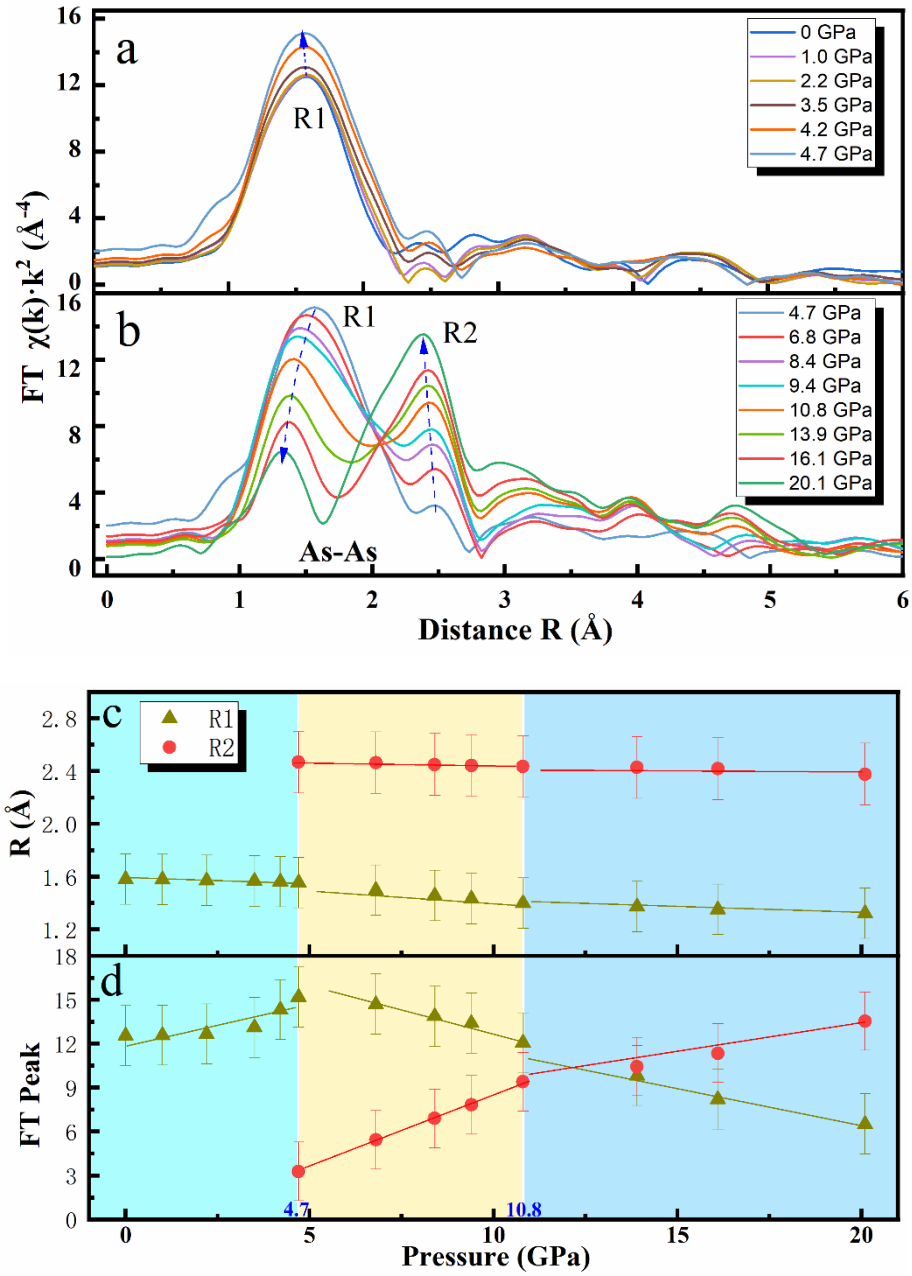

Figure 4.16 (a,b) The Fourier transformed EXAFS of bAs, Pressure dependence of the As-As distance (c), and the intensity of the As-As peak (d).

The Fourier transforms (FTs) at selected pressure points are shown in Figure 4.16. With the limited energy range of the EXAFS data, we can only get the first-neighbor distance. The FTs were calculated in the k-space range of 3–11 $Å^{-1}$. In the entire pressure range, the As-As bond lengths decrease gradually as the pressure increases, as shown in Figure 4.16 (c), which is consistent with the previous study.[262-264] Below 4.7 GPa, we could only see one peak R1. Above 4.7 GPa, the intensity of the R1 peak decreases with increased pressure, at the same time a new peak R2 appears, and its intensity increases with the increased pressure. As we have discussed above, bAs undergo a transition from Orthorhombic A17 to rhombohedral A7 at 4.7 GPa. The interlayer coupling became stronger with the increase of pressure. The phase transition from A17 to A7 is attributed to the intralayer bond breakage and interlayer bond formation. Therefore, we believe that the new R2 peak comes from the interlayer As-As bonds.

The intensity of the FT peak represents the number of atoms around the As atom, as shown at 4.16 d. When the pressure is lower than 4.7 GPa, the intensity of the FT peak increases because the interlayer coupling interaction of bAs enhances, which increases the coordination number of As atoms. Finally, the transition from A17 three-coordinated to A7 four-coordinated occurs at 4.7 GPa. From the above analysis, we already know that R1 and R2 represent the intralayer As-As bond and the interlayer As-As bond, respectively. After the transition from A17 to A7, with the formation of the interlayer As-As bond and the intralayer As-As bond broken, the As atom gradually changes from a four-coordinated to a three-coordinated A7. Therefore, the coordination number of As atoms in the layer corresponding to R1 (brown line) decreases, and the intensity of the FT peak decreases. Meanwhile, the coordination number (red line) of the As atom in the A7 phase corresponding to R2 gradually increased. As the increase of pressure, the transition from the A7 (three-coordinated)

phase to the SC phase (six-coordinated) will happen, and the FT peak intensity consequent increases.

Through the EXAFS study of bAs under high pressure, we found that bAs undergo a phase transition at 4.7 GPa and 10.8 GPa. However, the detailed structural information of bAs under high pressure still needs to be further explored through high-pressure XRD. Then, we can combine this structural information to do accurate structural optimization under high pressure using Artemis analysis.

4.3 Conclusions

Firstly, we performed EXAFS measurements on the Re L3 edge of ReS_2 and finally determined that two phase transitions occurred at 6.0 and 20.4 GPa, respectively. When the pressure exceeds 6.0 GPa, the interaction between the interlayer S atoms was enhanced, which eventually leads to the formation of S-S covalentlike bonds, and the phase transition of ReS_2 occurs. When the pressure reaches 20.4 GPa, the enhanced interlayer coupling makes the different layers of ReS_2 gradually transform from disordered stacking to ordered stacking, and keeps the 1T' phase up to 70.3 GPa. We attribute the phase transitions at 6.0 and 20.4 GPa to intralayer and interlayer transitions, respectively.

Then, we used a similar analysis method to ReS_2 as illustrated above to investigate the phase transition of bAs under pressure. We found that the transition from bAs (A17) to gAs (A7) occurred at 4.7 GPa. In addition, combined with previous research results, we believe that the transition from gAs to the simple cubic phase occurred at 10.8 GPa. In the future, we will combine the high-pressure XRD data to explore the phase structure transition of bAs under high pressure, and make an in-depth fitting analysis of the EXAFS data.

Chapter 5

Participate in user's experiment:

Identification of intermediates of a molecular ruthenium catalyst for water oxidation using *in situ* electrochemical XAS

5.1 Background

Solar fuels are one of the most promising alternatives to traditional fossil fuels. The abundant natural resources can be converted to solar fuels through solar-energy-driven chemical reactions, such as water oxidation and hydrogen generation reactions.[265-266] Efficient catalysts are critical to promoting the rate of water oxidation reactions and the eventual application of solar fuels.[267] Ruthenium-based molecular water oxidation catalysts have drawn considerable attention because their structures can be easily modified and they can mediate multiple-electron transfer reactions.[268]

The molecular mononuclear $Ru(bda)(L)_2$ (bda: 2,2′-bipyridine-6,6′-dicarboxylic acid; L: 4-picoline (pic) or isoquinoline (isq)) catalysts show remarkable activity with a turnover number＞10 000 and were successfully employed in photoelectrochemical cells; this family of catalysts is among the best water oxidation catalysts known to date.[269-272] However, the mechanistic

action of $Ru(bda)(L)_2$ is still under debate.[273-274] Therefore, it is essential to understand the fundamentals of the mode of action of this catalyst at an atomic level.

XAS is a powerful technique for studying metal-centered compounds.[275] XANES provides information about the oxidation state of the metal center, while EXAFS provides information about the local structure. To the best of our knowledge, no *in situ* spectroscopic study has been performed for the detection of these intermediates (Six-coordinated Ru^{II}, seven-coordinated Ru^{III}, and seven-coordinated Ru^{IV} species) or any other similar ruthenium complex in solution. *In situ* detection of intermediates is challenging because of numerous factors.[276-279] One of the biggest challenges is to avoid X-ray-induced sample damage, especially in solution.[276-279] Therefore, we need to design a simple and feasible experimental scheme to carry out the measurement.

5.2 Experimental design and measurements

5.2.1 The home-built electrochemical cell

The *in situ* electrochemical cell was home-made using a plastic cuvette with a path length of 1 cm, which contains two holes with 4 mm diameter in the front and backside of the cell. The holes were covered by Kapton films, which allow X-rays to pass through. The working electrode (WE), reference electrode (RE), and counter electrode (CE) are glassy carbon foam (40 PPI, 1×2 cm), Ag/AgCl, and platinum foil respectively. The cell was filled with a pH = 1 nitric acid solution as the supporting electrolyte. An illustration of the *in situ* electrochemical cell was shown in Figure 1.

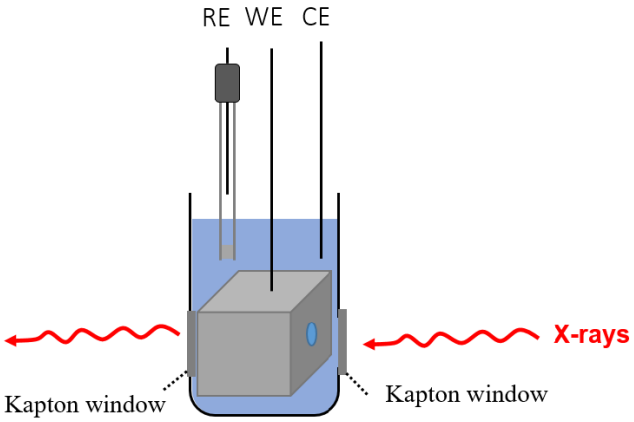

Figure 5.1. Illustration of *in situ* electrochemical cell. The cell contains two Kapton windows, which allow X-rays to pass through. The working electrode (WE), reference electrode (RE), and counter electrode (CE) are glassy carbon foam, Ag/AgCl, and Pt respectively.[280]

5.2.2 The catalyst selection

Because we need to conduct the in situ electrochemical XAS study of the Ru^{II} catalyst in solution for water oxidation reaction, the water-soluble Complex **1** was chosen as the catalyst as shown in Figure 2. Complex **1** has been synthesized and characterized following a previously described method.[281-282]

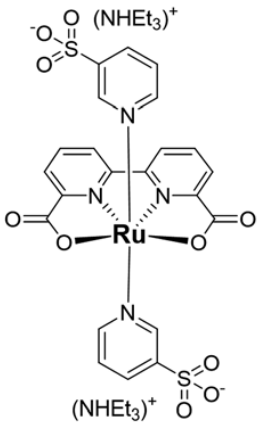

Figure 5.2. Chemical structure of Complex **1**.

5.2.3 *In situ* electrochemistry and XAS measurements

The home-built in situ electrochemical cell was filled with a pH = 1 nitric acid

solution as the supporting electrolyte. The electrolyte was protected with argon before and during the electrochemical measurements. Cyclic voltammetry (CV) was carried out in the solution with 1 mM of complex 1 in the electrolyte to determine the redox potentials, which can simulate the catalyst catalyzes solar water oxidation process. The catalyst was examined by XAS at the ruthenium K-edge to obtain its structural details during the reaction.

XAS was carried out at the ODE beamline at the Ru K-edge (22.117 keV). The experimental setup of XAS at the ODE beamline has been described in detail in Chapter 2. An EXAFS spectrum with a full energy range can be obtained from a single exposure to the CCD detector (SPEC-10, Princeton Instruments) with an energy resolution of ~0.5 eV. The exposure time for a single frame is 45 ms, which can significantly reduce radiation damage. Each spectrum was averaged over 500 frames to get a reasonable signal-to-noise ratio. The spectra of metallic ruthenium foil and ruthenium oxides were recorded at the beginning and after the sample measurements, which is used for energy calibration and comparison of the XANES signal to determine the oxidation states of the Ru atom in the sample material. X-ray absorption data were processed and analyzed using the Athena software package. The fit of experimental EXAFS data to available crystal structures is done using Artemis.

This work was published last year, and a detailed description of the experimental results and discussions can be found in the article.[280]

5.3 Conclusions

In summary, we have demonstrated a new approach for the *in situ* characterization of a homogeneous molecular electrocatalyst for water oxidation. Complex **1** was studied in situ under acidic conditions using a home-built electrochemical cell, in combination with an energy dispersive EXAFS setup.

The experimental setup allowed the acquisition of the XAS spectra without radiation-induced damage to the sample. The applied potential in the electrochemical cell was controlled to generate Ru^{II}, Ru^{III}, and Ru^{IV} species and appropriate conditions for the oxygen evolution reaction (OER). Six-coordinated Ru^{II}, seven-coordinated Ru^{III}, and seven-coordinated Ru^{IV} species were detected during the oxidation of the complex. For further oxidation of complex **1** to generate appropriate OER conditions, we speculate that the seven-coordinated Ru^{IV}, seven-coordinated Ru^{V}, and six-coordinated Ru^{III} species were present in the catalytic cycle. This in situ approach can be used to study other homogeneous water oxidation catalysts, thereby providing information on the static intermediates during electrocatalysis. Moreover, monitoring the catalyst in solution and the working electrode in the in situ electrochemical cell can allow us to distinguish between molecular catalysts and heterogeneous catalysts (metal oxides). In short, this work is a key step to capture static intermediates, which could be a reference for future study.

Chapter 6

Conclusions and perspectives

In this thesis, we selected $CsPbBr_3$, ReS_2, and bAs as the research objects. The electrical transport properties and optoelectronic properties of $CsPbBr_3$ were investigated using a high-pressure device based on the DAC, combined with high-pressure in-situ AC impedance spectroscopy and photocurrent measurement methods. In addition, their electronic structure evolution was investigated by high-pressure X-ray absorption spectroscopy (XANES+EXAFS), and the following results were obtained:

1. The conduction mechanism in $CsPbBr_3$ is mixed ionic/electron conduction. There are discontinuous changes in electrical parameters at the pressure point of phase transition. Moreover, the transition from ion/electron mixed conduction to pure electronic conduction occurs after the amorphization of $CsPbBr_3$. As the pressure increases, the contribution of grain boundaries to the resistance becomes more and more evident. But the grain boundary only affects the change of its resistance value and does not affect its intrinsic properties such as the trend of resistance change with pressure, and the pressure-induced transition from ionic/electronic conduction to pure electronic conduction.

2. The photoelectric response of $CsPbBr_3$ can be improved by pressure, the photocurrent reaching the maximum at 1.4 GPa, which is affected by ion migration. The ions migrated in $CsPbBr_3$ can be divided into two parts: 1) ions participating in migration under dark conditions without light; 2) ions excited

by light to participate in migration under light conditions. The ions involved in the migration are excited by light, migrate along the direction of the external electric field, and accumulate at the perovskite-electrode interface to form a new built-in electric field. The direction is opposite to that of the external electric field, so the external electric field is consumed, resulting in a gradual decrease in the photocurrent.

3. The variation of the X-ray absorption spectrum of $CsPbBr_3$ with pressure and the theoretical calculation results of the absorption spectrum directly confirm the isostructural phase transition at 1.2 GPa, and the main reason for the phase transition is the shortening of the Pb-Br bond length caused by the pressure.

4. For a layered material such as ReS_2, the pressure can easily affect the interlayer coupling by changing the interlayer distance, thereby changing its electronic structure. Many previous research results have found the phase transition of ReS_2 at low pressure. This phase transition is mainly caused by the formation of interlayer S-S covalentlike bonds, resulting in the rotation of the S atoms around the Re atoms intralayer. But we also found a high-pressure structural transition around 20 GPa, which is mainly caused by the high pressure driving ReS_2 from disordered to ordered stacking.

5. The structural transformation from bAs to gray arsenic isn't caused by the compression and extension of the intralayer structure along with one direction under pressure, instead is caused by the formation of interlayer bonds and the rupture of intralayer bonds. For the sudden transition in the intensity of the white line at 10.8 GPa, we speculate that the transition from gray arsenic (A7 phase) to simple cubic phase occurred.

In the past, we found no obvious ion migration phenomenon in $MAPbI_3$, while obvious ion migration phenomenon was found in bromine-based halide

perovskites ($FAPbBr_3$, $CsPbBr_3$, and $MAPbBr_3$), and the inductance was also found in $FAPbBr_3$, indicating that the change of organic/inorganic cations or halogen anions have a great influence on the properties of organic-inorganic hybrid perovskites. In the future, we plan to study high-pressure electrical transport and optoelectronic properties of chloride-based halide perovskites. Explore the relationship between ionic radius and properties of perovskites. Furthermore, for ReS_2, the structure of which was changed by pressure, as a promising photovoltaic material, it is necessary to perform high-pressure electrical measurements on it in the future to explore how high pressure tunes its optoelectronic properties. Although we confirmed the structural transformation of bAs to gAs, the phase transition point of 10.8 GPa is different from the theoretically predicted value for the transition from A7 to the simple cubic phase, which requires further high-pressure XRD measurement to determine its structure precisely at high pressure.

Bibliography

1. Nozik, A. J. Photoelectrochemistry: applications to solar energy conversion. Annual review of physical chemistry 1978, 29 (1), 189-222.
2. Lewis, N. S.; Nocera, D. G. Powering the planet: Chemical challenges in solar energy utilization. Proceedings of the National Academy of Sciences 2006, 103 (43), 15729-15735.
3. Nocera, D. G. Personalized energy: The home as a solar power station and solar gas station. ChemSusChem: Chemistry & Sustainability Energy & Materials 2009, 2 (5), 387-390.
4. Nuraje, N.; Asmatulu, R.; Kudaibergenov, S. Metal oxide-based functional materials for solar energy conversion: a review. Current Inorganic Chemistry (Discontinued) 2012, 2 (2), 124-146.
5. Nuraje, N.; Kudaibergenov, S.; Asmatulu, R. Solar energy storage with nanomaterials. Production of Fuels using Nanomaterials 2013, 95-117.
6. https://www.worldscientific.com/series/mae.
7. Tsao, J, Lewis, Nate and Crabtree, George. Solar FAQs[OL]. http://www.sandia.gov/~jytsao/Solar%20FAQs.pdf.
8. Lee, M. M.; Teuscher, J.; Miyasaka, T.; Murakami, T. N.; Snaith, H. J. Efficient hybrid solar cells based on meso-superstructured organometal halide perovskites. Science 2012, 338 (6107), 643-647.
9. Kojima, A.; Teshima, K.; Shirai, Y.; Miyasaka, T. Organometal halide perovskites as visible-light sensitizers for photovoltaic cells. Journal of the American Chemical Society 2009, 131 (17), 6050-6051.
10. Kim, H.-S.; Lee, C.-R.; Im, J.-H.; Lee, K.-B.; Moehl, T.; Marchioro, A.; Moon, S.-J.; Humphry-Baker, R.; Yum, J.-H.; Moser, J. E. Lead iodide perovskite

sensitized all-solid-state submicron thin film mesoscopic solar cell with efficiency exceeding 9%. Scientific reports 2012, 2 (1), 1-7.

11. Burschka, J.; Pellet, N.; Moon, S.-J.; Humphry-Baker, R.; Gao, P.; Nazeeruddin, M. K.; Grätzel, M. Sequential deposition as a route to high-performance perovskite-sensitized solar cells. Nature 2013, 499 (7458), 316-319.
12. Liu, M.; Johnston, M. B.; Snaith, H. J. Efficient planar heterojunction perovskite solar cells by vapour deposition. Nature 2013, 501 (7467), 395-398.
13. Rhodes, C. J. Perovskites and their potential use in solar energy applications. Science progress 2014, 97 (3), 279-287.
14. Yi, C.; Luo, J.; Meloni, S.; Boziki, A.; Ashari-Astani, N.; Grätzel, C.; Zakeeruddin, S. M.; Röthlisberger, U.; Grätzel, M. Entropic stabilization of mixed A-cation ABX 3 metal halide perovskites for high performance perovskite solar cells. Energy & Environmental Science 2016, 9 (2), 656-662.
15. Li, W.; Zhang, W.; Van Reenen, S.; Sutton, R. J.; Fan, J.; Haghighirad, A. A.; Johnston, M. B.; Wang, L.; Snaith, H. J. Enhanced UV-light stability of planar heterojunction perovskite solar cells with caesium bromide interface modification. Energy & Environmental Science 2016, 9 (2), 490-498.
16. Dang, Y.; Zhou, Y.; Liu, X.; Ju, D.; Xia, S.; Xia, H.; Tao, X. Formation of hybrid perovskite tin iodide single crystals by top-seeded solution growth. Angewandte Chemie International Edition 2016, 55 (10), 3447-3450.
17. Bi, D.; Tress, W.; Dar, M. I.; Gao, P.; Luo, J.; Renevier, C.; Schenk, K.; Abate, A.; Giordano, F.; Baena, J.-P. C. Efficient luminescent solar cells based on tailored mixed-cation perovskites. Science advances 2016, 2 (1), e1501170.
18. Yang, D.; Yang, Z.; Qin, W.; Zhang, Y.; Liu, S. F.; Li, C. Alternating precursor layer deposition for highly stable perovskite films towards efficient solar cells using vacuum deposition. Journal of Materials Chemistry A 2015, 3 (18), 9401-9405.

19. Liu, Y.; Yang, Z.; Cui, D.; Ren, X.; Sun, J.; Liu, X.; Zhang, J.; Wei, Q.; Fan, H.; Yu, F. Two-inch-sized perovskite CH3NH3PbX3 (X= Cl, Br, I) crystals: growth and characterization. Advanced materials 2015, 27 (35), 5176-5183.
20. Green, M. A.; Ho-Baillie, A.; Snaith, H. J. The emergence of perovskite solar cells. Nature photonics 2014, 8 (7), 506-514.
21. Stranks, S. D.; Eperon, G. E.; Grancini, G.; Menelaou, C.; Alcocer, M. J.; Leijtens, T.; Herz, L. M.; Petrozza, A.; Snaith, H. J. Electron-hole diffusion lengths exceeding 1 micrometer in an organometal trihalide perovskite absorber. Science 2013, 342 (6156), 341-344.
22. Deng, Y.; Peng, E.; Shao, Y.; Xiao, Z.; Dong, Q.; Huang, J. Scalable fabrication of efficient organolead trihalide perovskite solar cells with doctor-bladed active layers. Energy & Environmental Science 2015, 8 (5), 1544-1550.
23. Deschler, F.; Price, M.; Pathak, S.; Klintberg, L. E.; Jarausch, D.-D.; Higler, R.; Hüttner, S.; Leijtens, T.; Stranks, S. D.; Snaith, H. J. High photoluminescence efficiency and optically pumped lasing in solution-processed mixed halide perovskite semiconductors. The journal of physical chemistry letters 2014, 5 (8), 1421-1426.
24. Hao, F.; Stoumpos, C. C.; Cao, D. H.; Chang, R. P.; Kanatzidis, M. G. Lead-free solid-state organic–inorganic halide perovskite solar cells. Nature photonics 2014, 8 (6), 489-494.
25. Kazim, S.; Nazeeruddin, M. K.; Grätzel, M.; Ahmad, S. Perovskite as light harvester: a game changer in photovoltaics. Angewandte Chemie International Edition 2014, 53 (11), 2812-2824.
26. Kim, Y. H.; Cho, H.; Heo, J. H.; Kim, T. S.; Myoung, N.; Lee, C. L.; Im, S. H.; Lee, T. W. Multicolored organic/inorganic hybrid perovskite light-emitting diodes. Advanced materials 2015, 27 (7), 1248-1254.
27. Lee, B.; He, J.; Chang, R. P.; Kanatzidis, M. G. All-solid-state dye-sensitized solar cells with high efficiency. Nature 2012, 485 (7399), 486-489.

28. Tan, Z.-K.; Moghaddam, R. S.; Lai, M. L.; Docampo, P.; Higler, R.; Deschler, F.; Price, M.; Sadhanala, A.; Pazos, L. M.; Credgington, D. Bright light-emitting diodes based on organometal halide perovskite. Nature nanotechnology 2014, 9 (9), 687-692.
29. Xiao, Z.; Wang, D.; Dong, Q.; Wang, Q.; Wei, W.; Dai, J.; Zeng, X.; Huang, J. Unraveling the hidden function of a stabilizer in a precursor in improving hybrid perovskite film morphology for high efficiency solar cells. Energy & Environmental Science 2016, 9 (3), 867-872.
30. Xing, G.; Mathews, N.; Lim, S. S.; Yantara, N.; Liu, X.; Sabba, D.; Grätzel, M.; Mhaisalkar, S.; Sum, T. C. Low-temperature solution-processed wavelength-tunable perovskites for lasing. Nature materials 2014, 13 (5), 476-480.
31. Arora, N.; Dar, M. I.; Hinderhofer, A.; Pellet, N.; Schreiber, F.; Zakeeruddin, S. M.; Grätzel, M. Perovskite solar cells with CuSCN hole extraction layers yield stabilized efficiencies greater than 20%. Science 2017, 358 (6364), 768-771.
32. Ball, J. M.; Lee, M. M.; Hey, A.; Snaith, H. J. Low-temperature processed meso-superstructured to thin-film perovskite solar cells. Energy & Environmental Science 2013, 6 (6), 1739-1743.
33. Chen, H.; Ye, F.; Tang, W.; He, J.; Yin, M.; Wang, Y.; Xie, F.; Bi, E.; Yang, X.; Grätzel, M. A solvent-and vacuum-free route to large-area perovskite films for efficient solar modules. Nature 2017, 550 (7674), 92-95.
34. Chen, P.; Yin, X.; Que, M.; Liu, X.; Que, W. Low temperature solution processed indium oxide thin films with reliable photoelectrochemical stability for efficient and stable planar perovskite solar cells. Journal of Materials Chemistry A 2017, 5 (20), 9641-9648.
35. Docampo, P.; Ball, J. M.; Darwich, M.; Eperon, G. E.; Snaith, H. J. Efficient organometal trihalide perovskite planar-heterojunction solar cells on flexible polymer substrates. Nature communications 2013, 4 (1), 1-6.
36. Hou, Y.; Du, X.; Scheiner, S.; McMeekin, D. P.; Wang, Z.; Li, N.; Killian, M. S.;

Chen, H.; Richter, M.; Levchuk, I. A generic interface to reduce the efficiency-stability-cost gap of perovskite solar cells. Science 2017, 358 (6367), 1192-1197.

37. Snaith, H. J. Perovskites: the emergence of a new era for low-cost, high-efficiency solar cells. The journal of physical chemistry letters 2013, 4 (21), 3623-3630.
38. Tan, H.; Jain, A.; Voznyy, O.; Lan, X.; De Arquer, F. P. G.; Fan, J. Z.; Quintero-Bermudez, R.; Yuan, M.; Zhang, B.; Zhao, Y. Efficient and stable solution-processed planar perovskite solar cells via contact passivation. Science 2017, 355 (6326), 722-726.
39. Zhao, D.; Yu, Y.; Wang, C.; Liao, W.; Shrestha, N.; Grice, C. R.; Cimaroli, A. J.; Guan, L.; Ellingson, R. J.; Zhu, K. Low-bandgap mixed tin–lead iodide perovskite absorbers with long carrier lifetimes for all-perovskite tandem solar cells. Nature Energy 2017, 2 (4), 1-7.
40. NREL cell efficiency chart. (Accessed: June, 2021).
41. Novoselov, K. S.; Jiang, D.; Schedin, F.; Booth, T.; Khotkevich, V.; Morozov, S.; Geim, A. K. Two-dimensional atomic crystals. Proceedings of the National Academy of Sciences 2005, 102 (30), 10451-10453.
42. Radisavljevic, B.; Radenovic, A.; Brivio, J.; Giacometti, V.; Kis, A. Single-layer MoS 2 transistors. Nature nanotechnology 2011, 6 (3), 147-150.
43. Butler, S. Z.; Hollen, S. M.; Cao, L.; Cui, Y.; Gupta, J. A.; Gutiérrez, H. R.; Heinz, T. F.; Hong, S. S.; Huang, J.; Ismach, A. F. Progress, challenges, and opportunities in two-dimensional materials beyond graphene. ACS nano 2013, 7 (4), 2898-2926.
44. Xu, M.; Liang, T.; Shi, M.; Chen, H. Graphene-like two-dimensional materials. Chemical reviews 2013, 113 (5), 3766-3798.
45. Chen, Y.; Chen, C.; Kealhofer, R.; Liu, H.; Yuan, Z.; Jiang, L.; Suh, J.; Park, J.; Ko, C.; Choe, H. S. Black arsenic: a layered semiconductor with extreme in-plane

anisotropy. Advanced materials 2018, 30 (30), 1800754.

46. Li, L.; Yu, Y.; Ye, G. J.; Ge, Q.; Ou, X.; Wu, H.; Feng, D.; Chen, X. H.; Zhang, Y. Black phosphorus field-effect transistors. Nature nanotechnology 2014, 9 (5), 372.
47. Guo, J.; Liu, Y.; Ma, Y.; Zhu, E.; Lee, S.; Lu, Z.; Zhao, Z.; Xu, C.; Lee, S. J.; Wu, H. Few-layer GeAs field-effect transistors and infrared photodetectors. Advanced Materials 2018, 30 (21), 1705934.
48. Wang, X.; Li, Y.; Huang, L.; Jiang, X.-W.; Jiang, L.; Dong, H.; Wei, Z.; Li, J.; Hu, W. Short-wave near-infrared linear dichroism of two-dimensional germanium selenide. Journal of the American Chemical Society 2017, 139 (42), 14976-14982.
49. Tian, N.; Yang, Y.; Liu, D.; Liu, X.; Tan, P.-H.; Zhang, D.; Chang, K.; Li, H.; Zhao, M.; Li, J. R. High anisotropy in tubular layered exfoliated KP15. ACS nano 2018, 12 (2), 1712-1719.
50. Niu, Y.; Frisenda, R.; Flores, E.; Ares, J. R.; Jiao, W.; Perez de Lara, D.; Sánchez, C.; Wang, R.; Ferrer, I. J.; Castellanos-Gomez, A. Polarization-Sensitive and Broadband Photodetection Based on a Mixed-Dimensionality TiS3/Si p–n Junction. Advanced Optical Materials 2018, 6 (19), 1800351.
51. Wen, W.; Zhu, Y.; Liu, X.; Hsu, H. P.; Fei, Z.; Chen, Y.; Wang, X.; Zhang, M.; Lin, K. H.; Huang, F. S. Anisotropic spectroscopy and electrical properties of 2d res2 (1–x) se2x alloys with distorted 1t structure. Small 2017, 13 (12), 1603788.
52. Chhowalla, M.; Shin, H. S.; Eda, G.; Li, L.-J.; Loh, K. P.; Zhang, H. The chemistry of two-dimensional layered transition metal dichalcogenide nanosheets. Nature chemistry 2013, 5 (4), 263-275.
53. Li, H.; Wu, J.; Yin, Z.; Zhang, H. Preparation and applications of mechanically exfoliated single-layer and multilayer MoS2 and WSe2 nanosheets. Accounts of chemical research 2014, 47 (4), 1067-1075.

54. Coleman, J. N.; Lotya, M.; O'Neill, A.; Bergin, S. D.; King, P. J.; Khan, U.; Young, K.; Gaucher, A.; De, S.; Smith, R. J. Two-dimensional nanosheets produced by liquid exfoliation of layered materials. Science 2011, 331 (6017), 568-571.
55. Eda, G.; Yamaguchi, H.; Voiry, D.; Fujita, T.; Chen, M.; Chhowalla, M. Photoluminescence from chemically exfoliated MoS2. Nano letters 2011, 11 (12), 5111-5116.
56. Novoselov, K. S.; Geim, A. K.; Morozov, S. V.; Jiang, D.; Zhang, Y.; Dubonos, S. V.; Grigorieva, I. V.; Firsov, A. A. Electric field effect in atomically thin carbon films. science 2004, 306 (5696), 666-669.
57. Allen, M. J.; Tung, V. C.; Kaner, R. B. Honeycomb carbon: a review of graphene. Chemical reviews 2010, 110 (1), 132-145.
58. Lee, E. J.; Balasubramanian, K.; Weitz, R. T.; Burghard, M.; Kern, K. Contact and edge effects in graphene devices. Nature nanotechnology 2008, 3 (8), 486-490.
59. Novoselov, K. S.; Fal, V.; Colombo, L.; Gellert, P.; Schwab, M.; Kim, K. A roadmap for graphene. nature 2012, 490 (7419), 192-200.
60. Castellanos-Gomez, A. Why all the fuss about 2D semiconductors? Nature Photonics 2016, 10 (4), 202-204.
61. Ahmed, S.; Yi, J. Two-dimensional transition metal dichalcogenides and their charge carrier mobilities in field-effect transistors. Nano-micro letters 2017, 9 (4), 1-23.
62. Buscema, M.; Barkelid, M.; Zwiller, V.; van der Zant, H. S.; Steele, G. A.; Castellanos-Gomez, A. Large and tunable photothermoelectric effect in single-layer MoS2. Nano letters 2013, 13 (2), 358-363.
63. Han, S.; Kwon, H.; Kim, S. K.; Ryu, S.; Yun, W. S.; Kim, D.; Hwang, J.; Kang, J.-S.; Baik, J.; Shin, H. Band-gap transition induced by interlayer van der Waals interaction in MoS 2. Physical Review B 2011, 84 (4), 045409.
64. Lien, D.-H.; Kang, J. S.; Amani, M.; Chen, K.; Tosun, M.; Wang, H.-P.; Roy, T.;

Eggleston, M. S.; Wu, M. C.; Dubey, M. Engineering light outcoupling in 2D materials. Nano letters 2015, 15 (2), 1356-1361.

65. Lin, Z.; McCreary, A.; Briggs, N.; Subramanian, S.; Zhang, K.; Sun, Y.; Li, X.; Borys, N. J.; Yuan, H.; Fullerton-Shirey, S. K. 2D materials advances: from large scale synthesis and controlled heterostructures to improved characterization techniques, defects and applications. 2D Materials 2016, 3 (4), 042001.
66. Perea-López, N.; Lin, Z.; Pradhan, N. R.; Iñiguez-Rábago, A.; Elías, A. L.; McCreary, A.; Lou, J.; Ajayan, P. M.; Terrones, H.; Balicas, L. CVD-grown monolayered MoS2 as an effective photosensor operating at low-voltage. 2D Materials 2014, 1 (1), 011004.
67. Shim, J.; Park, H. Y.; Kang, D. H.; Kim, J. O.; Jo, S. H.; Park, Y.; Park, J. H. Electronic and optoelectronic devices based on two-dimensional materials: from fabrication to application. Advanced Electronic Materials 2017, 3 (4), 1600364.
68. Splendiani, A.; Sun, L.; Zhang, Y.; Li, T.; Kim, J.; Chim, C.-Y.; Galli, G.; Wang, F. Emerging photoluminescence in monolayer MoS2. Nano letters 2010, 10 (4), 1271-1275.
69. Tongay, S.; Zhou, J.; Ataca, C.; Liu, J.; Kang, J. S.; Matthews, T. S.; You, L.; Li, J.; Grossman, J. C.; Wu, J. Broad-range modulation of light emission in two-dimensional semiconductors by molecular physisorption gating. Nano letters 2013, 13 (6), 2831-2836.
70. Tsai, D.-S.; Liu, K.-K.; Lien, D.-H.; Tsai, M.-L.; Kang, C.-F.; Lin, C.-A.; Li, L.-J.; He, J.-H. Few-layer MoS2 with high broadband photogain and fast optical switching for use in harsh environments. Acs Nano 2013, 7 (5), 3905-3911.
71. Wang, H.; Yu, L.; Lee, Y.-H.; Shi, Y.; Hsu, A.; Chin, M. L.; Li, L.-J.; Dubey, M.; Kong, J.; Palacios, T. Integrated circuits based on bilayer MoS2 transistors. Nano letters 2012, 12 (9), 4674-4680.

72. Fang, H.; Chuang, S.; Chang, T. C.; Takei, K.; Takahashi, T.; Javey, A. High-performance single layered WSe2 p-FETs with chemically doped contacts. Nano letters 2012, 12 (7), 3788-3792.
73. Huang, Y.; Sutter, E.; Sadowski, J. T.; Cotlet, M.; Monti, O. L.; Racke, D. A.; Neupane, M. R.; Wickramaratne, D.; Lake, R. K.; Parkinson, B. A. Tin Disulfide An Emerging Layered Metal Dichalcogenide Semiconductor: Materials Properties and Device Characteristics. ACS nano 2014, 8 (10), 10743-10755.
74. Xia, F.; Wang, H.; Jia, Y. Rediscovering black phosphorus as an anisotropic layered material for optoelectronics and electronics. Nature communications 2014, 5 (1), 1-6.
75. Deng, Y.; Luo, Z.; Conrad, N. J.; Liu, H.; Gong, Y.; Najmaei, S.; Ajayan, P. M.; Lou, J.; Xu, X.; Ye, P. D. Black phosphorus–monolayer MoS2 van der Waals heterojunction p–n diode. ACS nano 2014, 8 (8), 8292-8299.
76. Castellanos-Gomez, A. Black phosphorus: narrow gap, wide applications. The journal of physical chemistry letters 2015, 6 (21), 4280-4291.
77. Liu, K.; Wu, J. Mechanical properties of two-dimensional materials and heterostructures. Journal of Materials Research 2016, 31 (7), 832-844.
78. Akinwande, D.; Brennan, C. J.; Bunch, J. S.; Egberts, P.; Felts, J. R.; Gao, H.; Huang, R.; Kim, J.-S.; Li, T.; Li, Y. A review on mechanics and mechanical properties of 2D materials—Graphene and beyond. Extreme Mechanics Letters 2017, 13, 42-77.
79. Jastrzebski, Z. Ceramics and Related Materials. Nature and Properties of Engineering Materials, John Wiley & Sons, Inc 1959, 281.
80. Late, D. J.; Rout, C. S.; Chakravarty, D.; Ratha, S. Emerging energy applications of two-dimensional layered materials. Can. Chem. Trans 2015, 3 (118-157), 118-157.
81. Yu, X.; Sivula, K. Toward large-area solar energy conversion with semiconducting 2D transition metal dichalcogenides. ACS energy letters

2016, 1 (1), 315-322.

82. Lee, J. Y.; Shin, J.-H.; Lee, G.-H.; Lee, C.-H. Two-dimensional semiconductor optoelectronics based on van der Waals heterostructures. Nanomaterials 2016, 6 (11), 193.
83. Tang, W.; Rassay, S.; Ravindra, N. Electronic & optical properties of transition-metal dichalcogenides. Madridge J Nano Tech 2017, 2 (1), 59-65.
84. Sundqvist, B. Fullerenes under high pressures. Advances in physics 1999, 48 (1), 1-134.
85. Zha, C.-S.; Mao, H.-k.; Hemley, R. J. Elasticity of MgO and a primary pressure scale to 55 GPa. Proceedings of the National Academy of Sciences 2000, 97 (25), 13494-13499.
86. McMillan, P. F. Chemistry at high pressure. Chemical Society Reviews 2006, 35 (10), 855-857.
87. Choukroun, M.; Grasset, O. Thermodynamic data and modeling of the water and ammonia-water phase diagrams up to 2.2 GPa for planetary geophysics. The Journal of chemical physics 2010, 133 (14), 144502.
88. Kurpiewska, K.; Lewiński, K. High pressure macromolecular crystallography for structural biology: a review. Open Life Sciences 2010, 5 (5), 531-542.
89. Hemley, R. J.; Ashcroft, N. W. The revealing role of pressure in the condensed matter sciences. Physics Today 1998, 51 (8), 26-32.
90. Shim, S.-H.; Bengtson, A.; Morgan, D.; Sturhahn, W.; Catalli, K.; Zhao, J.; Lerche, M.; Prakapenka, V. Electronic and magnetic structures of the postperovskite-type Fe2O3 and implications for planetary magnetic records and deep interiors. Proceedings of the National Academy of Sciences 2009, 106 (14), 5508-5512.
91. Solozhenko, V. L.; Kurakevych, O. O.; Andrault, D.; Le Godec, Y.; Mezouar, M. Ultimate metastable solubility of boron in diamond: Synthesis of superhard diamondlike BC 5. Physical Review Letters 2009, 102 (1), 015506.

92. Zarechnaya, E. Y.; Dubrovinsky, L.; Dubrovinskaia, N.; Filinchuk, Y.; Chernyshov, D.; Dmitriev, V.; Miyajima, N.; El Goresy, A.; Braun, H. F.; Van Smaalen, S. Superhard semiconducting optically transparent high pressure phase of boron. Physical review letters 2009, 102 (18), 185501.
93. Somayazulu, M.; Dera, P.; Goncharov, A. F.; Gramsch, S. A.; Liermann, P.; Yang, W.; Liu, Z.; Mao, H.-k.; Hemley, R. J. Pressure-induced bonding and compound formation in xenon–hydrogen solids. Nature chemistry 2010, 2 (1), 50-53.
94. Horikawa, D. D.; Iwata, K.-I.; Kawai, K.; Koseki, S.; Okuda, T.; Yamamoto, K. High hydrostatic pressure tolerance of four different anhydrobiotic animal species. Zoological science 2009, 26 (3), 238-242.
95. Zou, B.; Wang, B.; Li, S.; Zou, G. Synchrotron radiation applications on high-pressure research. Synchrotron Radiation Applications. Singapore: World Scientific 2018.
96. Grochala, W.; Hoffmann, R.; Feng, J.; Ashcroft, N. W. The chemical imagination at work in very tight places. Angewandte Chemie International Edition 2007, 46 (20), 3620-3642.
97. Bassett, W. A. Diamond anvil cell, 50th birthday. High Pressure Research 2009, 29 (2), 163-186.
98. Jayaraman, A. Diamond anvil cell and high-pressure physical investigations. Reviews of Modern Physics 1983, 55 (1), 65.
99. Bussod, G. Y.; Katsura, T.; Rubie, D. C. The large volume multi-anvil press as a high PT deformation apparatus. In Experimental Techniques in Mineral and Rock Physics, Springer: 1993; pp 579-599.
100. Paszkowicz, W. High-pressure powder X-ray diffraction at the turn of the century. Nuclear Instruments and Methods in Physics Research Section B: Beam Interactions with Materials and Atoms 2002, 198 (3-4), 142-182.
101. Miletich, R.; Allan, D. R.; Kuhs, W. F. High-pressure single-crystal techniques.

Reviews in Mineralogy and Geochemistry 2000, 41 (1), 445-519.

102. Akahama, Y.; Kawamura, H.; Hirao, N.; Ohishi, Y.; Takemura, K. In Raman scattering and x-ray diffraction experiments for phase III of solid hydrogen, Journal of Physics: Conference Series, IOP Publishing: 2010; p 012056.

103. Bassett, W. A. The diamond cell and the nature of the Earth's mantle. Annual Review of Earth and Planetary Sciences 1979, 7 (1), 357-384.

104. Piermarini, G. J.; Block, S.; Barnett, J.; Forman, R. Calibration of the pressure dependence of the R 1 ruby fluorescence line to 195 kbar. Journal of Applied Physics 1975, 46 (6), 2774-2780.

105. Grasset, O. Calibration of the R ruby fluorescence lines in the pressure range [0-1 GPa] and the temperature range [250-300 K]. High Pressure Research 2001, 21 (3-4), 139-157.

106. Rekhi, S.; Dubrovinsky, L. S.; Saxena, S. K. Study of temperature–induced ruby fluorescence shifts up to a pressure 15 GPa in an externally heated diamond anvil cell. High Pressure–High Temperature 1999.

107. Ragan, D. D.; Gustavsen, R.; Schiferl, D. Calibration of the ruby R 1 and R 2 fluorescence shifts as a function of temperature from 0 to 600 K. Journal of applied physics 1992, 72 (12), 5539-5544.

108. Mao, H.; Bell, P.; Shaner, J. t.; Steinberg, D. Specific volume measurements of Cu, Mo, Pd, and Ag and calibration of the ruby R 1 fluorescence pressure gauge from 0.06 to 1 Mbar. Journal of applied physics 1978, 49 (6), 3276-3283.

109. Barnett, J.; Block, S.; Piermarini, G. An optical fluorescence system for quantitative pressure measurement in the diamond-anvil cell. Review of scientific instruments 1973, 44 (1), 1-9.

110. Buras, B.; Olsen, J. S.; Gerward, L.; Will, G.; Hinze, E. X-ray energy-dispersive diffractometry using synchrotron radiation. Journal of Applied Crystallography 1977, 10 (6), 431-438.

111. Lee, S. K.; Lin, J.-F.; Cai, Y. Q.; Hiraoka, N.; Eng, P. J.; Okuchi, T.; Mao, H.-k.; Meng, Y.; Hu, M. Y.; Chow, P. X-ray Raman scattering study of MgSiO3 glass at high pressure: Implication for triclustered MgSiO3 melt in Earth's mantle. Proceedings of the National Academy of Sciences 2008, 105 (23), 7925-7929.

112. Rueff, J.-P.; Shukla, A. Inelastic x-ray scattering by electronic excitations under high pressure. Reviews of Modern Physics 2010, 82 (1), 847.

113. Penner-Hahn, J. E. X-ray absorption spectroscopy. Comprehensive Coordination Chemistry II 2003, 2, 159-186.

114. Westre, T. E.; Kennepohl, P.; DeWitt, J. G.; Hedman, B.; Hodgson, K. O.; Solomon, E. I. A multiplet analysis of Fe K-edge 1s→ 3d pre-edge features of iron complexes. Journal of the American Chemical Society 1997, 119 (27), 6297-6314.

115. Gawelda, W. Time-resolved x-ray absorption spectroscopy of transition metal complexes; EPFL: 2006.

116. Lee, P.; Pendry, J. Theory of the extended x-ray absorption fine structure. Physical Review B 1975, 11 (8), 2795.

117. Stern, E.; Sayers, D.; Lytle, F. Extended x-ray-absorption fine-structure technique. III. Determination of physical parameters. Physical Review B 1975, 11 (12), 4836.

118. Filipponi, A.; Di Cicco, A.; Natoli, C. R. X-ray-absorption spectroscopy and n-body distribution functions in condensed matter. I. Theory. Physical Review B 1995, 52 (21), 15122.

119. Filipponi, A.; Di Cicco, A. X-ray-absorption spectroscopy and n-body distribution functions in condensed matter. II. Data analysis and applications. Physical Review B 1995, 52 (21), 15135.

120. Newville, M. IFEFFIT: interactive XAFS analysis and FEFF fitting. Journal of synchrotron radiation 2001, 8 (2), 322-324.

121.Ravel, B.; Newville, M. ATHENA, ARTEMIS, HEPHAESTUS: data analysis for X-ray absorption spectroscopy using IFEFFIT. Journal of synchrotron radiation 2005, 12 (4), 537-541.

122.Aquilanti, G.; Trapananti, A.; Karandikar, A.; Kantor, I.; Marini, C.; Mathon, O.; Pascarelli, S.; Boehler, R. Melting of iron determined by X-ray absorption spectroscopy to 100 GPa. Proceedings of the National Academy of Sciences 2015, 112 (39), 12042-12045.

123.Ingalls, R.; Garcia, G.; Stern, E. X-ray absorption at high pressure. Physical Review Letters 1978, 40 (5), 334.

124.Itié, J.; Polian, A.; Martinez, D.; Briois, V.; Di Cicco, A.; Filipponi, A.; San Miguel, A. X-ray absorption spectroscopy under extreme conditions. Le Journal de Physique IV 1997, 7 (C2), C2-31-C2-38.

125.Kuramochi, K.; Ishimatsu, N.; Sakai, T.; Kawamura, N.; Irifune, T. An application of NPD to double-stage diamond anvil cells: XAS spectra of rhenium metal under high pressures above 300 GPa. High Pressure Research 2020, 40 (1), 119-129.

126.Mao, H.-K.; Chen, X.-J.; Ding, Y.; Li, B.; Wang, L. Solids, liquids, and gases under high pressure. Reviews of Modern Physics 2018, 90 (1), 015007.

127.Irifune, T.; Kurio, A.; Sakamoto, S.; Inoue, T.; Sumiya, H. Ultrahard polycrystalline diamond from graphite. Nature 2003, 421 (6923), 599-600.

128.Ishimatsu, N.; Kawamura, N.; Mizumaki, M.; Maruyama, H.; Sumiya, H.; Irifune, T. Applications of nano-polycrystalline diamond anvils to X-ray absorption spectroscopy under high pressure. High Pressure Research 2016, 36 (3), 381-390.

129.Rosa, A.; Mathon, O.; Torchio, R.; Jacobs, J.; Pasternak, S.; Irifune, T.; Pascarelli, S. Nano-polycrystalline diamond anvils: key devices for XAS at extreme conditions: their use, scientific impact, present status and future needs. High Pressure Research 2020, 40 (1), 65-81.

130.Mathon, O.; Beteva, A.; Borrel, J.; Bugnazet, D.; Gatla, S.; Hino, R.; Kantor, I.; Mairs, T.; Munoz, M.; Pasternak, S. The time-resolved and extreme conditions XAS (TEXAS) facility at the European Synchrotron Radiation Facility: the general-purpose EXAFS bending-magnet beamline BM23. Journal of synchrotron radiation 2015, 22 (6), 1548-1554.

131.Wilhelm, F.; Garbarino, G.; Jacobs, J.; Vitoux, H.; Steinmann, R.; Guillou, F.; Snigirev, A.; Snigireva, I.; Voisin, P.; Braithwaite, D. High pressure XANES and XMCD in the tender X-ray energy range. High Pressure Research 2016, 36 (3), 445-457.

132.Baudelet, F.; Kong, Q.; Nataf, L.; Cafun, J.; Congeduti, A.; Monza, A.; Chagnot, S.; Itié, J. ODE: a new beam line for high-pressure XAS and XMCD studies at SOLEIL. High Pressure Research 2011, 31 (1), 136-139.

133.Matsushita, T.; Phizackerley, R. P. A fast X-ray absorption spectrometer for use with synchrotron radiation. Japanese Journal of Applied Physics 1981, 20 (11), 2223.

134.Itie, J.; Polian, A.; Calas, G.; Petiau, J.; Fontaine, A.; Tolentino, H. Pressure-induced coordination changes in crystalline and vitreous GeO 2. Physical Review Letters 1989, 63 (4), 398.

135.Itié, J.; Briois, V.; Martinez-Garcia, D.; Polian, A.; San-Miguel, A. X-Ray Absorption Spectroscopy Applied to Pressure-Induced Transformations of Semiconductors. physica status solidi (b) 1999, 211 (1), 323-333.

136.Dartyge, E.; Flank, A.; Fontaine, A.; Jucha, A. Synchrotron radiation plus photodiode array: EXAFS in dispersive mode for fast microanalysis. Le Journal de Physique Colloques 1984, 45 (C2), C2-275-C2-277.

137.Tolentino, H.; Dartyge, E.; Fontaine, A.; Tourillon, G. X-ray absorption spectroscopy in the dispersive mode with synchrotron radiation: optical considerations. Journal of applied crystallography 1988, 21 (1), 15-22.

138.Ruffoni, M.; Pettifer, R. Calibration of spectra from dispersive XAS beamlines.

Journal of synchrotron radiation 2006, 13 (6), 489-493.

139. Iijima, S. Helical microtubules of graphitic carbon. nature 1991, 354 (6348), 56-58.

140. Bi, D.; Tress, W.; Dar, M. I.; Gao, P.; Luo, J.; Renevier, C.; Schenk, K.; Abate, A.; Giordano, F.; Baena, J.-P. C. Efficient luminescent solar cells based on tailored mixed-cation perovskites. Science advances 2016.

141. Bag, M.; Renna, L. A.; Adhikari, R. Y.; Karak, S.; Liu, F.; Lahti, P. M.; Russell, T. P.; Tuominen, M. T.; Venkataraman, D. Kinetics of Ion Transport in Perovskite Active Layers and Its Implications for Active Layer Stability. J Am Chem Soc 2015, 137 (40), 13130-13137.

142. Eames, C.; Frost, J. M.; Barnes, P. R. F.; O'Regan, B. C.; Walsh, A.; Islam, M. S. Ionic transport in hybrid lead iodide perovskite solar cells. Nat Commun 2015, 6, 7497.

143. Swarnkar, A.; Chulliyil, R.; Ravi, V. K.; Irfanullah, M.; Chowdhury, A.; Nag, A. Colloidal CsPbBr3 Perovskite Nanocrystals: Luminescence beyond Traditional Quantum Dots. Angewandte Chemie International Edition 2015, 54 (51), 15424-15428.

144. Protesescu, L.; Yakunin, S.; Bodnarchuk, M. I.; Krieg, F.; Caputo, R.; Hendon, C. H.; Yang, R. X.; Walsh, A.; Kovalenko, M. V. Nanocrystals of Cesium Lead Halide Perovskites (CsPbX3, X = Cl, Br, and I): Novel Optoelectronic Materials Showing Bright Emission with Wide Color Gamut. Nano Letters 2015, 15 (6), 3692-3696.

145. Alias, M. S.; Dursun, I.; Saidaminov, M. I.; Diallo, E. M.; Mishra, P.; Ng, T. K.; Bakr, O. M.; Ooi, B. S. Optical constants of CH3NH3PbBr3perovskite thin films measured by spectroscopic ellipsometry. Optics express 2016, 24 (15), 16586-94.

146. Xu, Y.-F.; Yang, M.-Z.; Chen, B.-X.; Wang, X.-D.; Chen, H.-Y.; Kuang, D.-B.; Su, C.-Y. A CsPbBr3 Perovskite Quantum Dot/Graphene Oxide Composite for

Photocatalytic CO2 Reduction. Journal of the American Chemical Society 2017, 139 (16), 5660-5663.

147. Han, J. S.; Le, Q. V.; Choi, J.; Hong, K.; Moon, C. W.; Kim, T. L.; Kim, H.; Kim, S. Y.; Jang, H. W. Air-Stable Cesium Lead Iodide Perovskite for Ultra-Low Operating Voltage Resistive Switching. Advanced Functional Materials 2018, 28 (5), 1705783.

148. Mizusaki, J.; Arai, K.; Fueki, K. Ionic conduction of the perovskite-type halides. Solid State Ionics 1983, 11 (3), 203-211.

149. Meloni, S.; Moehl, T.; Tress, W.; Franckevičius, M.; Saliba, M.; Lee, Y. H.; Gao, P.; Nazeeruddin, M. K.; Zakeeruddin, S. M.; Rothlisberger, U.; Graetzel, M. Ionic polarization-induced current–voltage hysteresis in CH3NH3PbX3 perovskite solar cells. Nature communications 2016, 7, 10334.

150. Pan, D.; Fu, Y.; Chen, J.; Czech, K. J.; Wright, J. C.; Jin, S. Visualization and Studies of Ion-Diffusion Kinetics in Cesium Lead Bromide Perovskite Nanowires. Nano Letters 2018, 18 (3), 1807-1813.

151. Eames, C.; Frost, J. M.; Barnes, P. R. F.; O'Regan, B. C.; Walsh, A.; Islam, M. S. Ionic transport in hybrid lead iodide perovskite solar cells. Nature Communications 2015, 6, 7497.

152. Narayan, R. L.; Sarma, M. V. S.; Suryanarayana, S. V. Ionic conductivity of CsPbCl3 and CsPbBr3. Journal of Materials Science Letters 1987, 6 (1), 93-94.

153. Narayan, R. L.; Suryanarayana, S. V. Transport properties of the perovskite-type halides. Materials Letters 1991, 11 (8), 305-308.

154. Zhang, L.; Zeng, Q.; Wang, K. Pressure-Induced Structural and Optical Properties of Inorganic Halide Perovskite CsPbBr3. The journal of physical chemistry letters 2017, 8 (16), 3752-3758.

155. Nagaoka, Y.; Hills-Kimball, K.; Tan, R.; Li, R.; Wang, Z.; Chen, O. Nanocube Superlattices of Cesium Lead Bromide Perovskites and Pressure-Induced

Phase Transformations at Atomic and Mesoscale Levels. Advanced materials 2017, 29 (18).

156.Xiao, G.; Cao, Y.; Qi, G.; Wang, L.; Liu, C.; Ma, Z.; Yang, X.; Sui, Y.; Zheng, W.; Zou, B. Pressure effects on structure and optical properties in cesium lead bromide perovskite nanocrystals. Journal of the American Chemical Society 2017, 139 (29), 10087-10094.

157.Ou, T.; Yan, J.; Xiao, C.; Shen, W.; Liu, C.; Liu, X.; Han, Y.; Ma, Y.; Gao, C. Visible light response, electrical transport, and amorphization in compressed organolead iodine perovskites. Nanoscale 2016, 8 (22), 11426-11431.

158.Yan, H.; Ou, T.; Jiao, H.; Wang, T.; Wang, Q.; Liu, C.; Liu, X.; Han, Y.; Ma, Y.; Gao, C. Pressure dependence of mixed conduction and photo responsiveness in organolead tribromide perovskites. The journal of physical chemistry letters 2017, 8 (13), 2944-2950.

159.Liang, J.; Wang, C.; Wang, Y.; Xu, Z.; Lu, Z.; Ma, Y.; Zhu, H.; Hu, Y.; Xiao, C.; Yi, X.; Zhu, G.; Lv, H.; Ma, L.; Chen, T.; Tie, Z.; Jin, Z.; Liu, J. All-Inorganic Perovskite Solar Cells. Journal of the American Chemical Society 2016, 138 (49), 15829-15832.

160.Tan, Z.-K.; Moghaddam, R. S.; Lai, M. L.; Docampo, P.; Higler, R.; Deschler, F.; Price, M.; Sadhanala, A.; Pazos, L. M.; Credgington, D.; Hanusch, F.; Bein, T.; Snaith, H. J.; Friend, R. H. Bright light-emitting diodes based on organometal halide perovskite. Nature Nanotechnology 2014, 9, 687.

161.Xing, G.; Mathews, N.; Lim, S. S.; Yantara, N.; Liu, X.; Sabba, D.; Grätzel, M.; Mhaisalkar, S.; Sum, T. C. Low-temperature solution-processed wavelength-tunable perovskites for lasing. Nature Materials 2014, 13, 476.

162.Yin, W.-J.; Wu, Y.; Wei, S.-H.; Noufi, R.; Al-Jassim, M. M.; Yan, Y. Engineering Grain Boundaries in Cu2ZnSnSe4 for Better Cell Performance: A First-Principle Study. Advanced Energy Materials 2014, 4 (1), 1300712.

163.Abou-Ras, D.; Schmidt, S. S.; Caballero, R.; Unold, T.; Schock, H.-W.; Koch, C.

T.; Schaffer, B.; Schaffer, M.; Choi, P.-P.; Cojocaru-Mirédin, O. Confined and Chemically Flexible Grain Boundaries in Polycrystalline Compound Semiconductors. Advanced Energy Materials 2012, 2 (8), 992-998.

164. Zhang, L.; Da Silva, J. L. F.; Li, J.; Yan, Y.; Gessert, T. A.; Wei, S.-H. Effect of Copassivation of Cl and Cu on CdTe Grain Boundaries. Physical review letters 2008, 101 (15), 155501.

165. Yin, W.-J.; Shi, T.; Yan, Y. Unique Properties of Halide Perovskites as Possible Origins of the Superior Solar Cell Performance. Advanced materials 2014, 26 (27), 4653-4658.

166. de Quilettes, D. W.; Vorpahl, S. M.; Stranks, S. D.; Nagaoka, H.; Eperon, G. E.; Ziffer, M. E.; Snaith, H. J.; Ginger, D. S. Impact of microstructure on local carrier lifetime in perovskite solar cells. Science 2015, 348 (6235), 683-686.

167. Xu, J.; Buin, A.; Ip, A. H.; Li, W.; Voznyy, O.; Comin, R.; Yuan, M.; Jeon, S.; Ning, Z.; McDowell, J. J.; Kanjanaboos, P.; Sun, J.-P.; Lan, X.; Quan, L. N.; Kim, D. H.; Hill, I. G.; Maksymovych, P.; Sargent, E. H. Perovskite–fullerene hybrid materials suppress hysteresis in planar diodes. Nature Communications 2015, 6, 7081.

168. De Marco, N.; Zhou, H.; Chen, Q.; Sun, P.; Liu, Z.; Meng, L.; Yao, E.-P.; Liu, Y.; Schiffer, A.; Yang, Y. Guanidinium: A Route to Enhanced Carrier Lifetime and Open-Circuit Voltage in Hybrid Perovskite Solar Cells. Nano Letters 2016, 16 (2), 1009-1016.

169. Thind, A. S.; Luo, G.; Hachtel, J. A.; Morrell, M. V.; Cho, S. B.; Borisevich, A. Y.; Idrobo, J.-C.; Xing, Y.; Mishra, R. Atomic Structure and Electrical Activity of Grain Boundaries and Ruddlesden–Popper Faults in Cesium Lead Bromide Perovskite. Advanced Materials 2019, 31 (4), 1805047.

170. Zhang, L.; Zeng, Q.; Wang, K. Pressure-induced structural and optical properties of inorganic halide perovskite CsPbBr3. The journal of physical chemistry letters 2017, 8 (16), 3752-3758.

171.Yu, C.; Yu, Q.; Gao, C.; Yang, H.; Liu, B.; Peng, G.; Han, Y.; Zhang, D.; Cui, X.; Liu, C. Phase transformation and resistivity of dumbbell-like ZnO microcrystals under high pressure. Journal of Applied Physics 2008, 103 (11), 114901.

172.Li, M.; Gao, C.; Ma, Y.; Li, Y.; Li, X.; Li, H.; Liu, J.; Hao, A.; He, C.; Huang, X. New diamond anvil cell system for in situ resistance measurement under extreme conditions. Review of scientific instruments 2006, 77 (12), 123902.

173.Mao, H.; Xu, J.-A.; Bell, P. Calibration of the ruby pressure gauge to 800 kbar under quasi-hydrostatic conditions. Journal of Geophysical Research: Solid Earth 1986, 91 (B5), 4673-4676.

174.Natoli, C.; Benfatto, M. A unifying scheme of interpretation of X-ray absorption spectra based on the multiple scattering theory. Le Journal de Physique Colloques 1986, 47 (C8), C8-11-C8-23.

175.Benfatto, M.; Congiu-Castellano, A.; Daniele, A.; Della Longa, S. MXAN: a new software procedure to perform geometrical fitting of experimental XANES spectra. Journal of Synchrotron Radiation 2001, 8 (2), 267-269.

176.Hayakawa, K.; Hatada, K.; Della Longa, S.; D'Angelo, P.; Benfatto, M. In Progresses in the MXAN fitting procedure, AIP Conference Proceedings, American Institute of Physics: 2007; pp 111-113.

177.Egger, D. A.; Kronik, L.; Rappe, A. M. Theory of Hydrogen Migration in Organic-Inorganic Halide Perovskites. Angewandte Chemie International Edition 2015, 54 (42), 12437-12441.

178.Azpiroz, J. M.; Mosconi, E.; Bisquert, J.; De Angelis, F. Defect migration in methylammonium lead iodide and its role in perovskite solar cell operation. Energy & Environmental Science 2015, 8 (7), 2118-2127.

179.Haruyama, J.; Sodeyama, K.; Han, L.; Tateyama, Y. First-Principles Study of Ion Diffusion in Perovskite Solar Cell Sensitizers. Journal of the American Chemical Society 2015, 137 (32), 10048-10051.

180.Yin, W.-J.; Shi, T.; Yan, Y. Unusual defect physics in CH3NH3PbI3 perovskite solar cell absorber. Applied Physics Letters 2014, 104 (6), 063903.

181.Chen, C.; Fu, Q.; Guo, P.; Chen, H.; Wang, M.; Luo, W.; Zheng, Z. Ionic transport characteristics of large-size CsPbBr3 single crystals. Materials Research Express 2019, 6 (11), 115808.

182.Zhang, B.-B.; Wang, F.; Zhang, H.; Xiao, B.; Sun, Q.; Guo, J.; Hafsia, A. B.; Shao, A.; Xu, Y.; Zhou, J. Defect proliferation in CsPbBr3 crystal induced by ion migration. Applied Physics Letters 2020, 116 (6), 063505.

183.Andrade, C. Calculation of chloride diffusion coefficients in concrete from ionic migration measurements. Cement and Concrete Research 1993, 23 (3), 724-742.

184.Wang, Q.; Liu, C.; Han, Y.; Gao, C.; Ma, Y. The determination of ionic transport properties at high pressures in a diamond anvil cell. Review of Scientific Instruments 2016, 87 (12), 123904.

185.Kim, G. Y.; Senocrate, A.; Yang, T.-Y.; Gregori, G.; Grätzel, M.; Maier, J. Large tunable photoeffect on ion conduction in halide perovskites and implications for photodecomposition. Nature Materials 2018, 17 (5), 445-449.

186.Juarez-Perez, E. J.; Sanchez, R. S.; Badia, L.; Garcia-Belmonte, G.; Kang, Y. S.; Mora-Sero, I.; Bisquert, J. Photoinduced Giant Dielectric Constant in Lead Halide Perovskite Solar Cells. The journal of physical chemistry letters 2014, 5 (13), 2390-2394.

187.Selig, O.; Sadhanala, A.; Müller, C.; Lovrincic, R.; Chen, Z.; Rezus, Y. L. A.; Frost, J. M.; Jansen, T. L. C.; Bakulin, A. A. Organic Cation Rotation and Immobilization in Pure and Mixed Methylammonium Lead-Halide Perovskites. Journal of the American Chemical Society 2017, 139 (11), 4068-4074.

188.Ascone, I.; Cognigni, A.; Le Godec, Y.; Paul Itié, J. X-ray absorption study of

Cu, Zn SOD under high pressure. International Journal of High Pressure Research 2000, 19 (1-6), 277-283.

189. Delacourt, C.; Poizot, P.; Bonnin, D.; Masquelier, C. Lithium-insertion mechanism in crystalline and amorphous FePO4 · nH2O. Journal of the Electrochemical Society 2009, 156 (7), A595.

190. Liu, W.; Borg, S. J.; Testemale, D.; Etschmann, B.; Hazemann, J.-L.; Brugger, J. Speciation and thermodynamic properties for cobalt chloride complexes in hydrothermal fluids at 35–440 C and 600 bar: an in-situ XAS study. Geochimica et Cosmochimica Acta 2011, 75 (5), 1227-1248.

191. Rodová, M.; Brožek, J.; Knížek, K.; Nitsch, K. Phase transitions in ternary caesium lead bromide. Journal of thermal analysis and calorimetry 2003, 71 (2), 667-673.

192. Bunker, G. Introduction to XAFS: a practical guide to X-ray absorption fine structure spectroscopy. Cambridge University Press: 2010.

193. Trcera, N.; Layek, S.; Shulman, M.; Polian, A.; Irifune, T.; Itié, J.; Rozenberg, G. K. XAS studies of pressure-induced structural and electronic transformations in α-FeOOH. Journal of Physics: Condensed Matter 2019, 31 (32), 325401.

194. Yin, W.-J.; Yang, J.-H.; Kang, J.; Yan, Y.; Wei, S.-H. Halide perovskite materials for solar cells: a theoretical review. Journal of Materials Chemistry A 2015, 3 (17), 8926-8942.

195. Chi, Z.-H.; Zhao, X.-M.; Zhang, H.; Goncharov, A. F.; Lobanov, S. S.; Kagayama, T.; Sakata, M.; Chen, X.-J. Pressure-induced metallization of molybdenum disulfide. Physical review letters 2014, 113 (3), 036802.

196. Kang, D.; Zhou, Y.; Yi, W.; Yang, C.; Guo, J.; Shi, Y.; Zhang, S.; Wang, Z.; Zhang, C.; Jiang, S. Superconductivity emerging from a suppressed large magnetoresistant state in tungsten ditelluride. Nature communications 2015, 6 (1), 1-6.

197.Pan, X.-C.; Chen, X.; Liu, H.; Feng, Y.; Wei, Z.; Zhou, Y.; Chi, Z.; Pi, L.; Yen, F.; Song, F. Pressure-driven dome-shaped superconductivity and electronic structural evolution in tungsten ditelluride. Nature communications 2015, 6 (1), 1-6.

198.Zhao, Z.; Zhang, H.; Yuan, H.; Wang, S.; Lin, Y.; Zeng, Q.; Xu, G.; Liu, Z.; Solanki, G.; Patel, K. Pressure induced metallization with absence of structural transition in layered molybdenum diselenide. Nature communications 2015, 6 (1), 1-8.

199.Barnett, R. L.; Polkovnikov, A.; Demler, E.; Yin, W.-G.; Ku, W. Coexistence of Gapless Excitations and Commensurate Charge-Density Wave in the 2 H Transition Metal Dichalcogenides. Physical review letters 2006, 96 (2), 026406.

200.Thoutam, L.; Wang, Y.; Xiao, Z.; Das, S.; Luican-Mayer, A.; Divan, R.; Crabtree, G.; Kwok, W. Temperature-dependent three-dimensional anisotropy of the magnetoresistance in WTe 2. Physical review letters 2015, 115 (4), 046602.

201.Yuan, N. F.; Mak, K. F.; Law, K. Possible topological superconducting phases of MoS 2. Physical review letters 2014, 113 (9), 097001.

202.Monney, G.; Monney, C.; Hildebrand, B.; Aebi, P.; Beck, H. Impact of Electron-Hole Correlations on the 1 T− TiSe 2 Electronic Structure. Physical review letters 2015, 114 (8), 086402.

203.Miwa, J. A.; Ulstrup, S.; Sørensen, S. G.; Dendzik, M.; Čabo, A. G.; Bianchi, M.; Lauritsen, J. V.; Hofmann, P. Electronic structure of epitaxial single-layer MoS 2. Physical review letters 2015, 114 (4), 046802.

204.Zhou, D.; Zhou, Y.; Pu, C.; Chen, X.; Lu, P.; Wang, X.; An, C.; Zhou, Y.; Miao, F.; Ho, C.-H. Pressure-induced metallization and superconducting phase in ReS 2. npj Quantum Materials 2017, 2 (1), 1-7.

205.Katzke, H.; Tolédano, P.; Depmeier, W. Phase transitions between polytypes and intralayer superstructures in transition metal dichalcogenides. Physical

Review B 2004, 69 (13), 134111.

206.Hromadova, L.; Martoňák, R.; Tosatti, E. Structure change, layer sliding, and metallization in high-pressure MoS 2. Physical Review B 2013, 87 (14), 144105.

207.Wypych, F.; Schöllhorn, R. 1T-MoS 2, a new metallic modification of molybdenum disulfide. Journal of the Chemical Society, Chemical Communications 1992, (19), 1386-1388.

208.Enyashin, A. N.; Yadgarov, L.; Houben, L.; Popov, I.; Weidenbach, M.; Tenne, R.; Bar-Sadan, M.; Seifert, G. New route for stabilization of 1T-WS2 and MoS2 phases. The Journal of Physical Chemistry C 2011, 115 (50), 24586-24591.

209.Merrill, L. Behavior of the AB2-Type Compounds at High Pressures and High Temperatures. Journal of Physical and Chemical Reference Data 1982, 11 (4), 1005-1064.

210.Silverman, M. S. Ultrahigh pressure-high temperature synthesis of rhombohedral dichalcogenides of molybdenum and tungsten. Inorganic Chemistry 1967, 6 (5), 1063-1064.

211. Beal, A. Intercalated Layered Materials, edited by F. Levy. Reidel, Dordrecht, The Netherlands: 1979.

212.Qian, X.; Liu, J.; Fu, L.; Li, J. Quantum spin Hall effect in two-dimensional transition metal dichalcogenides. Science 2014, 346 (6215), 1344-1347.

213.Calandra, M.; Mauri, F. Charge-density wave and superconducting dome in TiSe 2 from electron-phonon interaction. Physical review letters 2011, 106 (19), 196406.

214.Chatterjee, U.; Zhao, J.; Iavarone, M.; Di Capua, R.; Castellan, J.; Karapetrov, G.; Malliakas, C.; Kanatzidis, M. G.; Claus, H.; Ruff, J. Emergence of coherence in the charge-density wave state of 2 H-NbSe 2. Nature communications 2015, 6 (1), 1-7.

215.Shen, D.; Xie, B.; Zhao, J.; Yang, L.; Fang, L.; Shi, J.; He, R.; Lu, D.; Wen, H.; Feng, D. Novel mechanism of a charge density wave in a transition metal dichalcogenide. Physical review letters 2007, 99 (21), 216404.

216.Suderow, H.; Tissen, V.; Brison, J.; Martínez, J.; Vieira, S. Pressure Induced Effects on the Fermi Surface of Superconducting 2 H− NbSe 2. Physical review letters 2005, 95 (11), 117006.

217.Guillamón, I.; Suderow, H.; Vieira, S.; Cario, L.; Diener, P.; Rodiere, P. Superconducting density of states and vortex cores of 2H-NbS 2. Physical review letters 2008, 101 (16), 166407.

218.Chi, Z.; Chen, X.; Yen, F.; Peng, F.; Zhou, Y.; Zhu, J.; Zhang, Y.; Liu, X.; Lin, C.; Chu, S. Superconductivity in pristine 2 H a− MoS 2 at ultrahigh pressure. Physical review letters 2018, 120 (3), 037002.

219.Tongay, S.; Sahin, H.; Ko, C.; Luce, A.; Fan, W.; Liu, K.; Zhou, J.; Huang, Y.-S.; Ho, C.-H.; Yan, J. Monolayer behaviour in bulk ReS 2 due to electronic and vibrational decoupling. Nature communications 2014, 5 (1), 1-6.

220.Liu, E.; Fu, Y.; Wang, Y.; Feng, Y.; Liu, H.; Wan, X.; Zhou, W.; Wang, B.; Shao, L.; Ho, C.-H. Integrated digital inverters based on two-dimensional anisotropic ReS 2 field-effect transistors. Nature communications 2015, 6 (1), 1-7.

221.Ovchinnikov, D.; Gargiulo, F.; Allain, A.; Pasquier, D. J.; Dumcenco, D.; Ho, C.-H.; Yazyev, O. V.; Kis, A. Disorder engineering and conductivity dome in ReS 2 with electrolyte gating. Nature communications 2016, 7 (1), 1-7.

222.Nayak, A. P.; Bhattacharyya, S.; Zhu, J.; Liu, J.; Wu, X.; Pandey, T.; Jin, C.; Singh, A. K.; Akinwande, D.; Lin, J.-F. Pressure-induced semiconducting to metallic transition in multilayered molybdenum disulphide. Nature communications 2014, 5 (1), 1-9.

223.Nayak, A. P.; Yuan, Z.; Cao, B.; Liu, J.; Wu, J.; Moran, S. T.; Li, T.; Akinwande, D.; Jin, C.; Lin, J.-F. Pressure-modulated conductivity, carrier density, and

mobility of multilayered tungsten disulfide. ACS nano 2015, 9 (9), 9117-9123.

224.Hou, D.; Ma, Y.; Du, J.; Yan, J.; Ji, C.; Zhu, H. High pressure X-ray diffraction study of ReS2. Journal of Physics and Chemistry of Solids 2010, 71 (11), 1571-1575.

225.Wang, P.; Wang, Y.; Qu, J.; Zhu, Q.; Yang, W.; Zhu, J.; Wang, L.; Zhang, W.; He, D.; Zhao, Y. Pressure-induced structural and electronic transitions, metallization, and enhanced visible-light responsiveness in layered rhenium disulphide. Physical Review B 2018, 97 (23), 235202.

226.Yan, Y.; Jin, C.; Wang, J.; Qin, T.; Li, F.; Wang, K.; Han, Y.; Gao, C. Associated lattice and electronic structural evolutions in compressed multilayer ReS2. The journal of physical chemistry letters 2017, 8 (15), 3648-3655.

227.Sheremetyeva, N.; Tristant, D.; Yoshimura, A.; Gray, J.; Liang, L.; Meunier, V. First-principles study of the thermodynamic and vibrational properties of ReS 2 under pressure. Physical Review B 2019, 100 (21), 214101.

228.Jadczak, J.; Kutrowska-Girzycka, J.; Smoleński, T.; Kossacki, P.; Huang, Y.; Bryja, L. Exciton binding energy and hydrogenic Rydberg series in layered ReS 2. Scientific reports 2019, 9 (1), 1-9.

229.Ho, C.-H.; Liu, Z.-Z. Complete-series excitonic dipole emissions in few layer ReS2 and ReSe2 observed by polarized photoluminescence spectroscopy. Nano Energy 2019, 56, 641-650.

230.Zhao, K.; Huang, F.; Dai, C.-M.; Li, W.; Chen, S.-Y.; Jiang, K.; Huang, Y.-P.; Hu, Z.; Chu, J. Temperature dependence of phonon modes, optical constants, and optical band gap in two-dimensional ReS2 films. The Journal of Physical Chemistry C 2018, 122 (51), 29464-29469.

231.Qiao, X.-F.; Wu, J.-B.; Zhou, L.; Qiao, J.; Shi, W.; Chen, T.; Zhang, X.; Zhang, J.; Ji, W.; Tan, P.-H. Polytypism and unexpected strong interlayer coupling in two-dimensional layered ReS 2. Nanoscale 2016, 8 (15), 8324-8332.

232.He, R.; Yan, J.-A.; Yin, Z.; Ye, Z.; Ye, G.; Cheng, J.; Li, J.; Lui, C. Coupling and

stacking order of ReS2 atomic layers revealed by ultralow-frequency Raman spectroscopy. Nano letters 2016, 16 (2), 1404-1409.

233.Saha, P.; Ghosh, B.; Mazumder, A.; Glazyrin, K.; Dev Mukherjee, G. Pressure induced lattice expansion and phonon softening in layered ReS2. Journal of Applied Physics 2020, 128 (8), 085904.

234.Kuzmin, A.; Chaboy, J. EXAFS and XANES analysis of oxides at the nanoscale. IUCrJ 2014, 1 (6), 571-589.

235.Baldini, M.; Aquilanti, G.; Mao, H.; Yang, W.; Shen, G.; Pascarelli, S.; Mao, W. L. High-pressure EXAFS study of vitreous GeO 2 up to 44 GPa. Physical Review B 2010, 81 (2), 024201.

236.Murray, H.; Kelty, S.; Chianelli, R.; Day, C. Structure of rhenium disulfide. Inorganic Chemistry 1994, 33 (19), 4418-4420.

237.Novoselov, K. S.; Geim, A. K.; Morozov, S. V.; Jiang, D.-e.; Zhang, Y.; Dubonos, S. V.; Grigorieva, I. V.; Firsov, A. A. Electric field effect in atomically thin carbon films. science 2004, 306 (5696), 666-669.

238.Manzeli, S.; Ovchinnikov, D.; Pasquier, D.; Yazyev, O. V.; Kis, A. 2D transition metal dichalcogenides. Nature Reviews Materials 2017, 2 (8), 1-15.

239.Choi, W.; Choudhary, N.; Han, G. H.; Park, J.; Akinwande, D.; Lee, Y. H. Recent development of two-dimensional transition metal dichalcogenides and their applications. Materials Today 2017, 20 (3), 116-130.

240.Mak, K. F.; Lee, C.; Hone, J.; Shan, J.; Heinz, T. F. Atomically thin MoS 2: a new direct-gap semiconductor. Physical review letters 2010, 105 (13), 136805.

241.Kim, T.-Y.; Amani, M.; Ahn, G. H.; Song, Y.; Javey, A.; Chung, S.; Lee, T. Electrical properties of synthesized large-area MoS2 field-effect transistors fabricated with inkjet-printed contacts. ACS nano 2016, 10 (2), 2819-2826.

242.Haque, F.; Daeneke, T.; Kalantar-Zadeh, K.; Ou, J. Z. Two-dimensional transition metal oxide and chalcogenide-based photocatalysts. Nano-micro letters 2018, 10 (2), 1-27.

243.Zhao, Y.; Chen, Y.; Zhang, Y.-H.; Liu, S.-F. Recent advance in black phosphorus: Properties and applications. Materials Chemistry and Physics 2017, 189, 215-229.

244.Bridgman, P. TWO NEW MODIFICATIONS OF PHOSPHORUS. Journal of the American Chemical Society 1914, 36 (7), 1344-1363.

245.Zhang, K.; Feng, Y.; Wang, F.; Yang, Z.; Wang, J. Two dimensional hexagonal boron nitride (2D-hBN): synthesis, properties and applications. Journal of Materials Chemistry C 2017, 5 (46), 11992-12022.

246.Liu, H.; Neal, A. T.; Zhu, Z.; Luo, Z.; Xu, X.; Tománek, D.; Ye, P. D. Phosphorene: an unexplored 2D semiconductor with a high hole mobility. ACS nano 2014, 8 (4), 4033-4041.

247.Li, L.; Yu, Y.; Ye, G. J.; Ge, Q.; Ou, X.; Wu, H.; Feng, D.; Chen, X. H.; Zhang, Y. Black phosphorus field-effect transistors. Nature nanotechnology 2014, 9 (5), 372-377.

248.Luo, K.; Chen, S.; Duan, C. Indirect-direct band gap transition of two-dimensional arsenic layered semiconductors—cousins of black phosphorus. SCIENCE CHINA Physics, Mechanics & Astronomy 2015, 58 (8), 1-7.

249.Scalise, E.; Houssa, M.; Pourtois, G.; Afanas'ev, V.; Stesmans, A. Strain-induced semiconductor to metal transition in the two-dimensional honeycomb structure of MoS 2. Nano Research 2012, 5 (1), 43-48.

250.Sun, Z.; Xiang, Z.; Wang, Z.; Zhang, J.; Ma, L.; Wang, N.; Shang, C.; Meng, F.; Zou, L.; Zhang, Y. Magnetic field-induced electronic phase transition in the Dirac semimetal state of black phosphorus under pressure. Science Bulletin 2018, 63 (23), 1539-1544.

251.Liu, X.; Li, Z. Electric field and strain effect on graphene-MoS2 hybrid structure: ab initio calculations. The Journal of Physical Chemistry Letters 2015, 6 (16), 3269-3275.

252.Buscema, M.; Steele, G. A.; van der Zant, H. S.; Castellanos-Gomez, A. The

effect of the substrate on the Raman and photoluminescence emission of single-layer MoS 2. Nano research 2014, 7 (4), 561-571.

253.Norman, N. C. Chemistry of arsenic, antimony and bismuth. Springer Science & Business Media: 1997.

254.Osters, O.; Nilges, T.; Bachhuber, F.; Pielnhofer, F.; Weihrich, R.; Schöneich, M.; Schmidt, P. Synthesis and identification of metastable compounds: black arsenic—science or fiction? Angewandte Chemie International Edition 2012, 51 (12), 2994-2997.

255.Cheng, X.; Li, Y.; Shang, J.; Hu, C.; Ren, Y.; Liu, M.; Qi, Z. Thickness-dependent phase transition and optical behavior of MoS 2 films under high pressure. Nano Research 2018, 11 (2), 855-863.

256.Gong, P.-L.; Liu, D.-Y.; Yang, K.-S.; Xiang, Z.-J.; Chen, X.-H.; Zeng, Z.; Shen, S.-Q.; Zou, L.-J. Hydrostatic pressure induced three-dimensional Dirac semimetal in black phosphorus. Physical Review B 2016, 93 (19), 195434.

257.Li, X.; Sun, J.; Shahi, P.; Gao, M.; MacDonald, A. H.; Uwatoko, Y.; Xiang, T.; Goodenough, J. B.; Cheng, J.; Zhou, J. Pressure-induced phase transitions and superconductivity in a black phosphorus single crystal. Proceedings of the National Academy of Sciences 2018, 115 (40), 9935-9940.

258.Gao, C.; Li, R.; Zhong, M.; Wang, R.; Wang, M.; Lin, C.; Huang, L.; Cheng, Y.; Huang, W. Stability and phase transition of metastable black arsenic under high pressure. The journal of physical chemistry letters 2019, 11 (1), 93-98.

259.Cutler, J.; Chen, N.; Jiang, D.; Demopoulos, G.; Jia, Y.; Rowson, J. In The nature of arsenic in uranium mill tailings by X-ray absorption spectroscopy, Journal de Physique IV (Proceedings), EDP sciences: 2003; pp 337-340.

260.Kappen, P.; Webb, J. An EXAFS study of arsenic bonding on amorphous aluminium hydroxide. Applied geochemistry 2013, 31, 79-83.

261.Boulfelfel, S. E.; Seifert, G.; Grin, Y.; Leoni, S. Squeezing lone pairs: The A 17 to A 7 pressure-induced phase transition in black phosphorus. Physical

Review B 2012, 85 (1), 014110.

262.Beister, H.; Strössner, K.; Syassen, K. Rhombohedral to simple-cubic phase transition in arsenic under pressure. Physical Review B 1990, 41 (9), 5535.

263.Durandurdu, M. Ab initio simulation of the rhombohedral–to–simple-cubic transition in arsenic. Physical Review B 2005, 72 (7), 073208.

264.Feng, W.; Cui, S.; Hu, H.; Liu, H. First-principles study of A7 to simple cubic phase transformation in As. Physica B: Condensed Matter 2007, 400 (1-2), 22-25.

265.Li, L.; Duan, L.; Xu, Y.; Gorlov, M.; Hagfeldt, A.; Sun, L. A photoelectrochemical device for visible light driven water splitting by a molecular ruthenium catalyst assembled on dye-sensitized nanostructured TiO 2. Chemical communications 2010, 46 (39), 7307-7309.

266.Li, L.; Duan, L.; Wen, F.; Li, C.; Wang, M.; Hagfeldt, A.; Sun, L. Visible light driven hydrogen production from a photo-active cathode based on a molecular catalyst and organic dye-sensitized p-type nanostructured NiO. Chemical Communications 2012, 48 (7), 988-990.

267.Montoya, J. H.; Seitz, L. C.; Chakthranont, P.; Vojvodic, A.; Jaramillo, T. F.; Nørskov, J. K. Materials for solar fuels and chemicals. Nature materials 2017, 16 (1), 70-81.

268.Tong, L.; Thummel, R. P. Mononuclear ruthenium polypyridine complexes that catalyze water oxidation. Chemical science 2016, 7 (11), 6591-6603.

269.Duan, L.; Fischer, A.; Xu, Y.; Sun, L. Isolated seven-coordinate Ru (IV) dimer complex with [HOHOH]− bridging ligand as an intermediate for catalytic water oxidation. Journal of the American Chemical Society 2009, 131 (30), 10397-10399.

270.Gersten, S. W.; Samuels, G. J.; Meyer, T. J. Catalytic oxidation of water by an oxo-bridged ruthenium dimer. Journal of the American Chemical Society 1982, 104 (14), 4029-4030.

271.Liu, F.; Concepcion, J. J.; Jurss, J. W.; Cardolaccia, T.; Templeton, J. L.; Meyer, T. J. Mechanisms of water oxidation from the blue dimer to photosystem II. Inorganic Chemistry 2008, 47 (6), 1727-1752.

272.Lee, B. L.; Kärkäs, M. D.; Johnston, E. V.; Inge, A. K.; Tran, L. H.; Xu, Y.; Hansson, Ö.; Zou, X.; Åkermark, B. Synthesis and characterization of oligonuclear Ru, Co and Cu oxidation catalysts. Wiley Online Library: 2010.

273.Concepcion, J. J.; Zhong, D. K.; Szalda, D. J.; Muckerman, J. T.; Fujita, E. Mechanism of water oxidation by [Ru (bda)(L) 2]: the return of the "blue dimer". Chemical Communications 2015, 51 (19), 4105-4108.

274.Zhuo, Q.; Zhan, S.; Duan, L.; Liu, C.; Wu, X.; Ahlquist, M. S.; Li, F.; Sun, L. Tuning the O–O bond formation pathways of molecular water oxidation catalysts on electrode surfaces via second coordination sphere engineering. Chinese Journal of Catalysis 2021, 42 (3), 460-469.

275.Sayers, D. E.; Stern, E. A.; Lytle, F. W. New technique for investigating noncrystalline structures: Fourier analysis of the extended x-ray—absorption fine structure. Physical review letters 1971, 27 (18), 1204.

276.Watanabe, N.; Morais, J.; Alves, M. Design of an electrochemical cell for in situ XAS studies. Journal of electron spectroscopy and related phenomena 2007, 156, 164-167.

277.Dong, C. L.; Vayssieres, L. In Situ/Operando X-ray Spectroscopies for Advanced Investigation of Energy Materials. Chemistry-A European Journal 2018, 24 (69), 18356-18373.

278.Katsoudas, J. P.; Timofeeva, E. V.; Segre, C. U. Design of electrochemical cells for in-situ XAS experiments. NSTI-Nanotech 2013 2013, 1, 13-15.

279.Hennig, C.; Tutschku, J.; Rossberg, A.; Bernhard, G.; Scheinost, A. Comparative EXAFS investigation of uranium (VI) and-(IV) aquo chloro complexes in solution using a newly developed spectroelectrochemical cell. Inorganic chemistry 2005, 44 (19), 6655-6661.

280. Li, L.; Yan, H.; Li, F.; Kong, Q.; Yuan, C.; Weng, T.-C. Identification of intermediates of a molecular ruthenium catalyst for water oxidation using in situ electrochemical X-ray absorption spectroscopy. Physical Chemistry Chemical Physics 2021, 23 (41), 23961-23966.
281. Daniel, Q.; Huang, P.; Fan, T.; Wang, Y.; Duan, L.; Wang, L.; Li, F.; Rinkevicius, Z.; Mamedov, F.; Ahlquist, M. S. Rearranging from 6-to 7-coordination initiates the catalytic activity: An EPR study on a Ru-bda water oxidation catalyst. Coordination chemistry reviews 2017, 346, 206-215.
282. Duan, L.; Wang, L.; Inge, A. K.; Fischer, A.; Zou, X.; Sun, L. Insights into Ru-based molecular water oxidation catalysts: Electronic and noncovalent-interaction effects on their catalytic activities. Inorganic chemistry 2013, 52 (14), 7844-7852.